

DEPARTMENT OF MECHANICAL ENGINEERING
COLLEGE OF ENGINEERING & TECHNOLOGY
OLD DOMINION UNIVERSITY
NORFOLK, VIRGINIA 23529

**STUDIES ON NONEQUILIBRIUM PHENOMENA IN
SUPERSONIC CHEMICALLY REACTING FLOWS**

By

Rajnish Chandrasekhar, Graduate Research Assistant

and

S.N. Tiwari, Principal Investigator

Progress Report

For the period ended August 31, 1993

Prepared for

National Aeronautics and Space Administration

Langley Research Center

Hampton, VA 23681-0001

Under

Research Grant NAG-1-423

Drs. A. Kumar and J.P. Drummond, Technical Monitors

FLDMD-Theoretical Flow Physics Branch

Submitted by the

Old Dominion University Research Foundation

P.O. Box 6369

Norfolk, VA 23508-0369

November 1993

11-3434

193068

139 p

N94-17215

Unclass

G3/34 0193068

(NASA-CR-194662) STUDIES ON
NONEQUILIBRIUM PHENOMENA IN
SUPERSONIC CHEMICALLY REACTING
FLOWS Progress Report for period
ending 31 Aug. 1993 (Old Dominion
Univ.) 139 p

**DEPARTMENT OF MECHANICAL ENGINEERING
COLLEGE OF ENGINEERING & TECHNOLOGY
OLD DOMINION UNIVERSITY
NORFOLK, VIRGINIA 23529**

**STUDIES ON NONEQUILIBRIUM PHENOMENA IN
SUPERSONIC CHEMICALLY REACTING FLOWS**

By

Rajnish Chandrasekhar, Graduate Research Assistant

and

S.N. Tiwari, Principal Investigator

Progress Report

For the period ended August 31, 1993

Prepared for

National Aeronautics and Space Administration

Langley Research Center

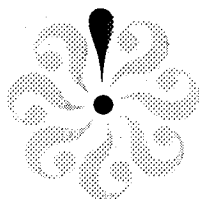
Hampton, VA 23681-0001

Under

Research Grant NAG-1-423

Drs. A. Kumar and J.P. Drummond, Technical Monitors

FLDMD-Theoretical Flow Physics Branch



November 1993

ABSTRACT

STUDIES ON NONEQUILIBRIUM PHENOMENA IN SUPERSONIC CHEMICALLY REACTING FLOWS

This study deals with a systematic investigation of nonequilibrium processes in supersonic combustion. The two-dimensional, elliptic Navier-Stokes equations are used to investigate supersonic flows with nonequilibrium chemistry and thermodynamics, coupled with radiation, for hydrogen-air systems. The explicit, unsplit MacCormack finite-difference scheme is used to advance the governing equations in time, until convergence is achieved.

For a basic understanding of the flow physics, premixed flows undergoing finite rate chemical reactions are investigated. Results obtained for specific conditions indicate that the radiative interactions vary substantially, depending on reactions involving HO_2 and NO species, and that this can have a noticeable influence on the flowfield.

The second part of this study deals with premixed reacting flows under thermal nonequilibrium conditions. Here, the critical problem is coupling of the vibrational relaxation process with the radiative heat transfer. The specific problem considered is a premixed expanding flow in a supersonic nozzle. Results indicate the presence of nonequilibrium conditions in the expansion region of the nozzle. This results in reduction of the radiative interactions in the flowfield.

Next, the present study focuses on investigation of non-premixed flows under chemical nonequilibrium conditions. In this case, the main problem is the coupled turbulence-chemistry interaction. The resulting formulation is validated by comparison with experimental data on reacting supersonic coflowing jets. Results indicate that the effect of heat release is to lower the turbulent shear stress and the mean density. The last part of this study proposes a new theoretical formulation for the coupled turbulence-radiation interactions. Results obtained for the coflowing jets experiment indicate that the effect of turbulence is to enhance the radiative interactions.

ACKNOWLEDGEMENTS

This is a progress report on the research project, "Analysis and Computation of Internal Flow Field in a Scramjet Engine," for the period ended August 31, 1993. Special attention during this period was directed to "Studies on Nonequilibrium Phenomena in Supersonic Chemically Reacting Flows."

The authors are indebted to Drs. R. L. Ash, A. O. Demuren, J. P. Drummond, A. Kumar, and J. Tweed for many useful and constructive suggestions during the course of this study and in the preparation of the final manuscript.

This work, in part, was supported by the NASA Langley Research Center (Theoretical Flow Physics Branch of the Fluid Mechanics Division) through the grant NAG-1-423. Th grant was monitored by Drs. A. Kumar and J. P. Drummond. The work, in part, was also supported by the Old Dominion University's ICAM Project through NASA grant NAG-1-363; this grant was monitored by Mr. Robert L. Yang, Assistant University Affairs Officer, NASA Langley Research Center, Hampton, Virginia 23681-0001.

TABLE OF CONTENTS

	<u>Page</u>
ACKNOWLEDGEMENTS	iii
LIST OF TABLES	vi
LIST OF FIGURES	vii
LIST OF SYMBOLS	x
 Chapter	
1. OVERVIEW AND RATIONALE	1
2. PREMIXED CHEMICAL NONEQUILIBRIUM FLOWS	5
2.1 Introduction	5
2.1.1 Literature Survey	5
2.1.2 Discussion of Physical Model	7
2.2 Basic Governing Equations	7
2.3 Chemistry and Thermodynamic Models	10
2.4 Radiative Interactions	13
2.5 Method of Solution	15

3.	PREMIXED THERMOCHEMICAL NONEQUILIBRIUM FLOWS	18
3.1	Introduction	18
3.2	Governing Equations	22
3.3	Thermal Nonequilibrium	24
3.4	Radiative Interactions	25
3.4.1	Local Thermodynamic Equilibrium	26
3.4.2	Non-local Thermodynamic Equilibrium	26
3.5	Method of Solution	27
4.	NONPREMIXED NONEQUILIBRIUM FLOWS	29
4.1	Introduction	29
4.2	Basic Governing Equations	32
4.3	Reynolds Stress Turbulence Model	37
4.4	Radiative Interactions	39
4.5	Method of Solution	40
5.	RESULTS AND DISCUSSION	41
5.1	Chemical Nonequilibrium and Radiative Interactions	41
5.2	Thermochemical Nonequilibrium and Radiative Interactions	66
5.3	Turbulence-Chemistry Interactions	84
5.4	Turbulence-Radiation Interactions	113
6.	CONCLUSIONS	117
	REFERENCES	119

LIST OF TABLES

<u>Table</u>		<u>Page</u>
2.1	Hydrogen-Air Mechanism	12
4.1	Conditions for the Beach experiment	34
4.2	Conditions for the Jarrett-Pitz experiment	34

LIST OF FIGURES

<u>Figure</u>		<u>Page</u>
2.1	Physical model for premixed chemical nonequilibrium	8
2.2	Plane radiating layer between parallel boundaries	14
3.1	Schematic diagram of nozzle for air chemistry	21
3.2	Schematic diagram of nozzle for H ₂ —air chemistry	23
4.1	Schematic of the coaxial jet flowfield	33
5.1	Temperature profiles	43
5.2	Pressure profiles (y=0.13 cm.)	44
5.3	H ₂ O mass fraction profiles	45
5.4	OH mass fraction profiles	46
5.5	Grid sensitivity results	47
5.6	Effect of reaction rates	49
5.7	Effect of NO and HO ₂ reactions	50
5.8	Profiles of streamwise radiative flux	52
5.9	Profiles of normal radiative flux	53
5.10	Radiation effects on temperature profiles (2-step model)	54
5.10	Radiation effects on temperature profiles (18-step model)	55
5.10	Radiation effects on temperature profiles (35-step model)	56
5.11	Radiation effects on pressure profiles at y = 0.13 cm. (2-step model) . .	57
5.11	Radiation effects on pressure profiles at y = 0.13 cm. (18-step model) .	58
5.11	Radiation effects on pressure profiles at y = 0.13 cm. (35-step model) .	59

5.12	Radiation effects on H ₂ O profiles (2-step model)	60
5.12	Radiation effects on H ₂ O profiles (18-step model)	61
5.12	Radiation effects on H ₂ O profiles (35-step model)	62
5.13	Radiation effects on OH profiles (2-step model)	63
5.13	Radiation effects on OH profiles (18-step model)	64
5.13	Radiation effects on OH profiles (35-model)	65
5.14	Air chemistry temperature profiles (1-D)	68
5.15	Temperature profiles (1-D)	69
5.15	Pressure profiles (1-D)	70
5.16	Grid resolution study on streamwise radiative flux — at wall (j = jmax-1)	72
5.16	Streamwise radiative flux profiles — midway (j = jmid)	73
5.16	Streamwise radiative flux profiles — wall (j = jmax-1)	74
5.17	Normal radiative flux profiles (j = jmid)	75
5.17	Normal radiative flux profiles (j = jmax-1)	76
5.18	Translational temperatures (j = 1)	78
5.18	Translational temperature (j = jmid)	79
5.18	Translational temperatures (j = jmax-1)	80
5.19	Pressure profiles (j = 1)	81
5.19	Pressure profiles (j = jmid)	82
5.19	Pressure profiles (j = jmax-1)	83
5.20	Vibrational temperature (j = 1)	85
5.20	Vibrational temperatures (j = jmid)	86
5.20	Vibrational temperatures (j = jmax-1)	87
5.21	Water mass fraction profiles (j = 1)	88

5.21	Water mass fraction profiles ($j = j_{\text{mid}}$)	89
5.21	Water mass fraction profiles ($j = j_{\text{max}}-1$)	90
5.22	Radial profile of initial temperature	92
5.23	Grid resolution study on mean density	93
5.23	Profiles of major species concentrations	94
5.24	Profiles of mixture fraction	96
5.25	Profiles of minor species fraction	97
5.26	Radial profile of density	98
5.27	Radial profile of normalized turbulent shear stress	99
5.27	Effect of different B.C.'s on turbulent shear stress	100
5.27	Mixture fraction profile — effect of different shear stress B.C.'s	101
5.28	Radial profile of mixture fraction	103
5.29	Radial profile of temperature	105
5.30	Profile of water mass fraction	106
5.31	Radial profile of normalized turbulent shear stress	107
5.32	Profile of R.H.S. of $\widetilde{u'v'}$ equation	108
5.33	Effect of “pressure-strain” model on turbulent shear stress	109
5.34	Effect of “pressure-strain” model on temperature	110
5.35	Effect of multivariate species PDF on water mass fraction	112
5.36	Profiles of streamwise radiative flux — Jarret-Pitz experiment	114
5.37	Effect of “turbulent/radiation” coupling on temperature	116

LIST OF SYMBOLS

A	=	band absorptance, m^{-1}
A_o	=	band width parameter, m^{-1}
C_j	=	concentration of the j^{th} species, $kg\text{-mole}/m^3$
C_o	=	correlation parameter, $(N/m^2)^{-1}m^{-1}$
C_p	=	constant pressure specific heat, $J/kg\text{-K}$
c	=	speed of light
D	=	binary mass diffusivity
E	=	total vibration energy
e_ω	=	Planck's function
f_j	=	mass fraction of the j^{th} species
H	=	total enthalpy, J/kg
h	=	static enthalpy, J/kg
h	=	Planck's constant = 6.6262×10^{-27} erg.sec
k	=	turbulent kinetic energy = $\widetilde{u_i' u_i'}/2$
k_b	=	backward rate constant
k_f	=	forward rate constant
k	=	Boltzmann's constant = 1.3806×10^{-16} erg K^{-1}
M_t	=	turbulent Mach number
P	=	pressure, N/m^2

P_j	=	partial pressure of the j^{th} species
q_R	=	total radiative flux
R	=	gas constant
S	=	integrated band intensity, $(\text{N/m}^2)^{-1}\text{m}^{-2}$
T	=	translational-rotational temperature, K
T_v	=	vibrational temperature, K
u, v	=	velocity in x- and y- directions, m/s
w_j	=	production rate of the j^{th} species, $\text{kg/m}^3\text{-s}$
x, y	=	physical coordinates

Greek Symbols

γ	=	ratio of specific heats
ϵ	=	turbulent dissipation rate
θ_v	=	characteristic vibrational temperature
κ_p	=	Planck mean absorption coefficient
λ	=	second coefficient of viscosity, wavelength
μ	=	dynamic viscosity, kg/m-s
ξ, η	=	computational coordinates
ρ	=	density
σ	=	Stefan-Boltzmann constant = $5.668 \times 10^{-8} \text{ erg K}^{-4}$
τ	=	shear stress
ϕ	=	equivalence ratio
χ	=	turbulent Prandtl or Schmidt number
ψ	=	thermal conductivity
ω	=	wave number, m^{-1}

Superscripts

- ~ = Favre — averaging (density — weighted)
- ' = fluctuating density — weighted variable
- = Reynolds — averaging (time — weighted)
- “ = fluctuating time — weighted variable

Chapter 1

OVERVIEW AND RATIONALE

In recent years there has been a renewed interest in the development of a hypersonic transatmospheric aerospace vehicle capable of flying at sub-orbital speeds. A hydrogen-fueled supersonic combustion ramjet (scramjet) engine is a strong candidate for propelling such a vehicle. The airflow is compressed inside the engine inlet and the supersonic combustion takes place inside the scramjet combustor. After this, the burned gases are expanded through the nozzles, followed by the undersurface of the vehicle. For a better understanding of the complex flowfield in different regions of the engine, both experimental and computational techniques have been employed. The complexity of these flows makes traditional wind tunnel tests quite difficult. However advances in computer architecture and efficient algorithms, make it possible to numerically investigate the flow in various sections of the scramjet module. Therefore, Computational Fluid Dynamics (CFD) is an extremely valuable tool for numerical simulation of supersonic combustion.

The flowfield in the combustor and nozzle sections of the scramjet is characterized by very short residence times. This could lead to chemical nonequilibrium, since the chemical reaction time will be of the same order of magnitude as the flow residence time. Furthermore, the scramjet flowfield is characterized by diffusive or non-premixed burning. However, premixed flows can be considered for preliminary studies, as well as for flow analysis in detonation wave engines. This lays the foundation for the present work, which is carried out in a systematic manner.

In the case of premixed flows, the air and fuel are thoroughly mixed in the required stoichiometric proportion, prior to combustion. Uncertainty in the choice of appropriate chemistry models can affect predictions of ignition delay. This underlines the need to study effects of chemical kinetics. Furthermore, this high enthalpy gaseous mixture encounters very short residence times and wide temperature and pressure variations. This could cause thermochemical nonequilibrium conditions. In addition, the combustion of hydrogen and air in the scramjet combustor results in absorbing-emitting gases such as water vapor and hydroxyl radicals. Existence of such gases makes it necessary to include the effect of radiation heat transfer.

The objective of the first part of this study is to investigate premixed flows undergoing finite rate chemical reactions. Here, the key problem is to determine the impact of chemical kinetics on the radiative interactions. The specific problem considered is the premixed flow in a channel with a ten-degree compression ramp. Three different chemistry models are used, accounting for increasing numbers of reactions and participating species. Two models assume nitrogen as inert, while the third chemistry model accounts for nitrogen reactions and NO_x formation. The tangent slab approximation is used in the radiative flux formulation. A pseudo-gray model is used to represent the absorption-emission characteristics of the participating species. Results obtained for specific conditions indicate that the radiative interactions vary substantially, depending on reactions involving HO_2 and NO species, and that this can have a noticeable influence on the flowfield. This provides the analytical tools required for further investigation of nonequilibrium processes in supersonic combustion.

The objective of the second part of this study is to investigate premixed reacting flows under thermal nonequilibrium conditions. Here, the critical problem is coupling of vibrational relaxation process with the radiative heat transfer. This has been implemented

in a unique manner. The specific problem considered is the premixed expanding flow in a supersonic nozzle. The reacting flow consists of seven species, one of which is the inert N_2 molecule. The thermal state of the gas is modeled with one translational-rotational temperature and five vibrational temperatures. The harmonic oscillator model is used in the formulation for vibrational relaxation. Results obtained for this case indicate the presence of nonequilibrium in the expansion region. This, in turn, reduces the radiative interactions and can have a significant influence on the flowfield.

In the case of non-premixed flows, the engine efficiency is strongly influenced by turbulent mixing of the fuel and oxidizer and its effect on chemical reactions. A variety of turbulence models can be applied to the analysis of the scramjet flowfield. Most of these models assume the turbulence to be isotropic. However, the occurrence of heat release due to chemical reactions, and the presence of shocks, could lead to anisotropic turbulence. This effect can be simulated by the Reynolds Stress models. Consequently, the objective of the third part of this study is to investigate non-premixed flows undergoing chemical nonequilibrium. A differential Reynolds Stress turbulence model has been applied to the Favre-averaged Navier-Stokes equations. An assumed Beta Probability Density Function is applied to account for the chemical source terms in the conservation equations. The resulting formulation is validated by comparison with experimental data on reacting supersonic coflowing jets. Results obtained for specific conditions demonstrate that the effect of chemical reaction on the turbulence is significant.

As stated earlier, the combustion of hydrogen and air in the scramjet combustor results in gases such as water vapor and hydroxyl radicals. Occurrence of such absorbing-emitting gases in the turbulent flame, implies the need to simulate the effect of radiative interactions. Thus, the objective of the last part of this work is to investigate turbulent

radiating flames. Here, the unsolved problem is the coupled turbulence-radiation interaction, for which a novel theoretical formulation has been proposed. Results obtained for the coflowing jets experiment indicate that the effect of turbulence is to enhance the radiative interactions.

The explicit, unsplit MacCormack finite-difference scheme is used to advance the governing equations in time, until convergence is achieved. The chemistry source term in the species equation is treated implicitly to alleviate the stiffness associated with fast reactions. Details of the theoretical formulations along with the methods of solution, are given in the ensuing chapters. Premixed flows are discussed in Chaps. 2 and 3. Chemical nonequilibrium is dealt with in Chap. 2, while thermochemical nonequilibrium receives attention in Chap. 3. An exposé of non-premixed flows is given in Chap. 4. The computational results obtained are presented and discussed in Chap. 5.

Chapter 2

PREMIXED CHEMICAL NONEQUILIBRIUM FLOWS

In this chapter, the chemical nonequilibrium phenomena pertaining to premixed, supersonic reacting flows are discussed. First, the problem is introduced. Then, the relevant literature is reviewed and the physical model is described. This is followed by a layout of the governing equations. After this, the method of solution is discussed.

2.1 Introduction

In the case of premixed flows, the air and the fuel are thoroughly mixed in the required stoichiometric proportion, prior to combustion. This gaseous mixture encounters very short residence times ($O[1.0 \text{ msec}]$), which will be of the same order of magnitude as the chemical reaction time. Uncertainty in the choice of appropriate chemistry models can affect predictions of ignition delay. This underlines the need to study effects of chemical kinetics. In addition, the combustion of hydrogen and air in the scramjet combustor results in absorbing-emitting gases such as water vapor and hydroxyl radicals. Existence of such gases makes it necessary to include the effect of radiation heat transfer.

2.1.1 Literature Survey

Several computer programs have been developed and applied to gain more insight into the problem involving a scramjet flowfield [1–3]*. Kumar [1] carried out numerical simulations of scramjet inlet flowfields. Drummond et al. [2, 3] developed a spectral method code for predicting the behavior of supersonic reacting mixing layers.

* Numbers in brackets indicate references.

Considerable work has been done in the past decade to model the chemical kinetic mechanism of the hydrogen-air system [4–7]. A simple two-step finite-rate chemistry model was used by Chitsomboon et al. [4] as well as by Rogers and Schexnayder [5]. A complete model would involve some 60 reaction paths, making numerical solution very difficult, if not impossible [5]. The two-step model [4, 5] has only four species and two reaction paths, and is used for preliminary studies. However, there are several limitations to this model, such as ignition-phase inaccuracy (i.e. a much shorter ignition delay), and overprediction of flame temperature as well as longer reaction times. Recent improvements in this area include an 8-species, 14-reaction model used by Shuen and Yoon [6]. While none of these aforementioned models account for nitrogen reactions (by assuming nitrogen was inert), recent developments in this area include a 15-species, 35-reaction model reported by Carpenter [7]. This latter model accounts for NO_x formation and other nitrogen reactions in the hydrogen-air system.

There are several models available in the literature to represent the absorption-emission characteristics of molecular gases [8–13]. Sparrow and Cess [8] wrote a definitive text on radiative heat transfer. Tien [9] as well as Cess and Tiwari [10] investigated thermal radiation properties of gases. Band models for infrared radiation were reviewed by Edwards [11] and Tiwari [12, 13].

One- and two-dimensional radiative heat transfer equations for various flow and combustion related problems are available [14–22]. Tsai and Chan [14] studied multi-dimensional radiative transfer. Chung and Kim [15] reported a solution for two-dimensional radiation using the finite element method. Coupled radiation and convection were investigated by Im and Ahluwalia [16] as well as Soufiani and Taine [17]. Tiwari [18, 19] studied transient radiative interactions in gases, Mani et al. [20–22] obtained numerical solutions of supersonic chemically reacting and radiating flows.

As the above literature survey clearly indicates, there is a need for additional studies in this key field. The objective of this chapter is to determine the impact of chemical kinetics on the radiative interactions. The specific problem considered is the premixed flow in a channel with a ten-degree compression ramp. Three different chemistry models are used, accounting for increasing number of reactions and participating species. Two models assume nitrogen as inert, while the third chemistry model accounts for nitrogen reactions and NO_x formation. The tangent slab approximation is used in the radiative flux formulation. A pseudo-gray model is used to represent the absorption-emission characteristics of the participating species.

2.1.2 Discussion of Physical Model

The specific problem considered is the supersonic flow of premixed hydrogen and air (stoichiometric equivalence ratio $\phi = 1.0$) in a channel with a compression corner on the lower boundary (Fig. 2.1). The physical dimensions considered for obtaining results are $L = 2\text{cm.}$, $X_1 = 1\text{ cm.}$, $X_2 = 2\text{ cm.}$, $L_x = X_1 + X_2 = 3\text{ cm.}$, and $\alpha = 10\text{ degrees}$. The flow is ignited by the shock from the compression corner. The inlet conditions which are representative of scramjet operating conditions, are $P_\infty = 1.0\text{ atm.}$, $T_\infty = 900\text{ K}$ and $M_\infty = 4.0$. This same flow has been computed by several researchers [4, 6, 20–22] as a benchmark case.

2.2 Basic Governing Equations

The physical model for analyzing the flowfield in a supersonic combustor is described by the Navier-Stokes and species continuity equations. For two-dimensional flows, these equations are expressed in physical coordinates as [2, 3]

$$\frac{\partial U}{\partial t} + \frac{\partial F}{\partial x} + \frac{\partial G}{\partial y} + H = 0 \quad (2.1)$$

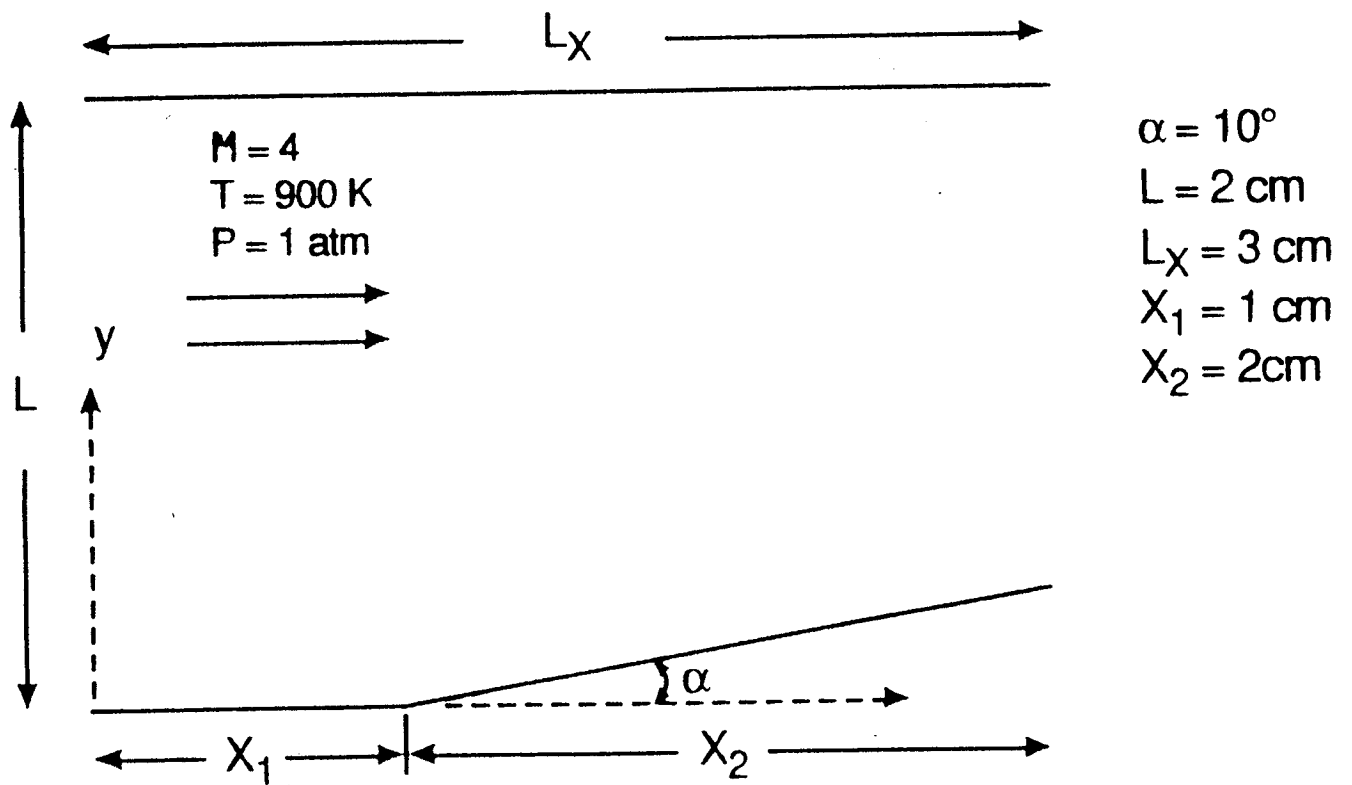


Fig. 2.1 Physical model for premixed chemical nonequilibrium

where vectors U , F , G and H are written as,

$$\begin{aligned}
 U &= \begin{bmatrix} \rho \\ \rho u \\ \rho v \\ \rho E \\ \rho f_j \end{bmatrix} \\
 F &= \begin{bmatrix} \rho u \\ \rho u^2 + p + \tau_{xx} \\ \rho uv + \tau_{xy} \\ (\rho E + p)u + \tau_{xx}u + \tau_{xy}v + q_{cx} + q_{Rx} \\ \rho u f_j - \rho D \frac{\partial f_j}{\partial x} \end{bmatrix} \\
 G &= \begin{bmatrix} \rho v \\ \rho uv + \tau_{yx} \\ \rho v^2 + p + \tau_{yy} \\ (\rho E + p)v + \tau_{xy}u + \tau_{yy}v + q_{cy} + q_{Ry} \\ \rho v f_j - \rho D \frac{\partial f_j}{\partial y} \end{bmatrix} \\
 H &= \begin{bmatrix} 0 \\ 0 \\ 0 \\ 0 \\ -w_j \end{bmatrix}
 \end{aligned} \tag{2.2}$$

The viscous stress tensors in the F and G terms are given as,

$$\tau_{xx} = -\lambda \left(\frac{\partial u}{\partial x} + \frac{\partial v}{\partial y} \right) - 2\mu \frac{\partial u}{\partial x} \tag{2.3a}$$

$$\tau_{xy} = -\mu \left(\frac{\partial u}{\partial y} + \frac{\partial v}{\partial x} \right) \tag{2.3b}$$

$$\tau_{yy} = -\lambda \left(\frac{\partial u}{\partial x} + \frac{\partial v}{\partial y} \right) - 2\mu \frac{\partial v}{\partial y} \tag{2.3c}$$

where $\lambda = -\frac{2}{3}\mu$ invokes the Stokes' hypothesis. This assumption of zero bulk viscosity is true for an incompressible gas, as well as for boundary layer type flows [23–25]. The quantities q_{cx} and q_{cy} in the F and G terms are the components of the conduction heat flux and are expressed as

$$q_{cx} = -\psi \frac{\partial T}{\partial x} \quad ; \quad q_{cy} = -\psi \frac{\partial T}{\partial y} \tag{2.4}$$

The molecular viscosity μ is evaluated from Sutherland's formula [22]. The total internal energy E in Eq. (2.2) is given by

$$E = -\frac{P}{\rho} + \frac{u^2 + v^2}{2} + \sum_{j=1}^m h_j f_j \quad (2.5)$$

Specific relations are needed for the chemistry and radiative flux terms. These are discussed in the following sections.

2.3 Chemistry and Thermodynamic Models

Chemical reaction rate expressions are usually determined by summing the contributions from each relevant reaction path to obtain the total rate of change of each species. Each path is governed by a law of mass action expression in which the rate constants can be determined from a temperature dependent Arrhenius expression. The reaction mechanism is expressed in a general form as

$$\sum_{j=1}^{ns} \gamma'_{ij} C_j \xrightleftharpoons[k_{bi}]{k_{fi}} \sum_{j=1}^{ns} \gamma''_{ij} C_j, \quad i = 1, nr \quad (2.6)$$

where ns = number of species and nr = number of reactions. The chemistry source terms \dot{w}_j in Eq. (2.2) are obtained, on a mass basis, by multiplying the molar changes and corresponding molecular weight as

$$\begin{aligned} \dot{w}_j = M_j C_j = M_j \sum_{i=1}^{nr} (\gamma''_{ij} - \gamma'_{ij}) & \left[k_{fi} \prod_{m=1}^{ns} C_m^{\gamma'_{im}} \right. \\ & \left. - k_{bi} \prod_{m=1}^{ns} C_m^{\gamma''_{im}} \right], \quad j = 1, ns \end{aligned} \quad (2.7)$$

The reaction rate constants k_{fi} and k_{bi} , appearing in Eqs. (2.6) and (2.7), are determined from an Arrhenius rate expression as

$$k_{fi} = A_i T^b \exp\left(-\frac{E_i}{RT}\right) \quad (2.8)$$

Table 2.1 Hydrogen-Air Mechanism

	REACTION	A(moles)	N(cm ³)	E(calories/gm-mole)
(1)	$O_2 + H_2 \rightleftharpoons OH + OH$	1.70×10^{13}	0	48150
(2)	$O_2 + H \rightleftharpoons OH + O$	1.42×10^{14}	0	16400
(3)	$H_2 + OH \rightleftharpoons H_2O + H$	3.16×10^{07}	1.8	3030
(4)	$H_2 + O \rightleftharpoons OH + O$	2.07×10^{14}	0	13750
(5)	$OH + OH \rightleftharpoons H_2O + O$	5.50×10^{13}	0	7000
(6)	$H + OH + M \rightleftharpoons H_2O + M$	2.21×10^{22}	-2.0	0
(7)	$H + H + M \rightleftharpoons H_2 + M$	6.53×10^{17}	-1.0	0
(8)	$H + O_2 + M \rightleftharpoons HO_2 + M$	3.20×10^{18}	-1.0	0
(9)	$OH + HO_2 \rightleftharpoons O_2 + H_2O$	5.00×10^{13}	0	1000
(10)	$H + HO_2 \rightleftharpoons H_2 + O_2$	2.53×10^{13}	0	700
(11)	$H + HO_2 \rightleftharpoons OH + OH$	1.99×10^{14}	0	1800
(12)	$O + HO_2 \rightleftharpoons O_2 + OH$	5.00×10^{13}	0	1000
(13)	$HO_2 + HO_2 \rightleftharpoons O_2 + H_2O_2$	1.99×10^{12}	0	0
(14)	$H_2 + HO_2 \rightleftharpoons H + H_2O_2$	3.01×10^{11}	0	18700
(15)	$OH + H_2O_2 \rightleftharpoons H_2O + HO_2$	1.02×10^{13}	0	1900
(16)	$H + H_2O_2 \rightleftharpoons H_2O + OH$	5.00×10^{14}	0	10000
(17)	$O + H_2O_2 \rightleftharpoons OH + HO_2$	1.99×10^{13}	0	5900
(18)	$H_2O_2 + M \rightleftharpoons OH + OH + M$	1.21×10^{17}	0	45500
(19)	$O_2 + M \rightleftharpoons O + O + M$	2.75×10^{19}	-1.0	118700
(20)	$N_2 + M \rightleftharpoons N + N + M$	3.70×10^{21}	-1.6	225000
(21)	$N + O_2 \rightleftharpoons O + NO$	6.40×10^{09}	1.0	6300
(22)	$N + NO \rightleftharpoons O + N_2$	1.60×10^{13}	0	0
(23)	$N + OH \rightleftharpoons H + NO$	6.30×10^{11}	0.5	0
(24)	$H + NO + M \rightleftharpoons HNO + M$	5.40×10^{15}	0	-600
(25)	$H + HNO \rightleftharpoons H_2 + NO$	4.80×10^{12}	0	0
(26)	$O + HNO \rightleftharpoons OH + NO$	5.00×10^{11}	0.5	0
(27)	$OH + HNO \rightleftharpoons H_2O + NO$	3.60×10^{13}	0	0
(28)	$HO_2 + HNO \rightleftharpoons H_2O_2 + NO$	2.00×10^{12}	0	0
(29)	$HO_2 + NO \rightleftharpoons OH + NO_2$	3.43×10^{12}	0	-260
(30)	$H + NO_2 \rightleftharpoons OH + NO$	3.50×10^{14}	0	1500
(31)	$O + NO_2 \rightleftharpoons O_2 + NO$	1.00×10^{13}	0	600
(32)	$NO_2 + M \rightleftharpoons O + NO + M$	1.16×10^{16}	0	66000
(33)	$M + OH + NO \rightleftharpoons HNO_2 + M$	5.60×10^{15}	0	-1700
(34)	$M + OH + NO_2 \rightleftharpoons HNO_3 + M$	3.00×10^{15}	0	-3800
(35)	$OH + HNO_2 \rightleftharpoons H_2O + NO_2$	1.60×10^{12}	0	0
*	global	2-step	model	*
(1'')	$H_2 + O_2 \rightleftharpoons 2OH$	11.4×10^{47}	-10.0	4865
(2'')	$2OH + H_2 \rightleftharpoons 2H_2O$	2.50×10^{64}	-13.0	42500

2.4 Radiative Interactions

Evaluation of the energy equation presented in Eq. (2.2) requires an appropriate expression for the radiative flux term, q_R . Therefore, a suitable radiative transport model is needed. Various models are available in the literature to represent the absorption-emission characteristics of the molecular species [22]. The equations of radiative transport are expressed generally in integro-differential forms. The integration involves both the frequency spectrum and physical coordinates. In many realistic three-dimensional physical problems, the complexity of the radiative transport equations can be reduced by introduction of the tangent-slab approximation. This approximation treats the gas layer as a one-dimensional slab in evaluation of the radiative flux (Fig. 2.2).

Detailed derivations of radiative flux equations for gray as well as nongray radiation have been carried out previously [22]. For a multiband gaseous system, the nongray radiative flux in the normal direction is expressed as

$$q_R(y) = e_1 - e_2 + \sum_{i=1}^n A_{oi} \left\{ \int_0^y \left[\frac{de_{\omega_i}(z)}{dz} \right] \bar{A}_i \left[\frac{3}{2} \frac{u_{oi}}{L} (y - z) \right] dz + \int_y^L \left[\frac{de_{\omega_i}(z)}{dz} \right] \bar{A}_i \left[\frac{3}{2} \frac{u_{oi}}{L} (z - y) \right] dz \right\} \quad (2.15)$$

Information on the band absorptance \bar{A}_i and other quantities are available in the cited references.

For a gray medium, the spectral absorption coefficient κ_ω is independent of the wave number, and an expression for the radiative flux is obtained as [8, 22]

$$q_R(y) = e_1 - e_2 + \frac{3}{2} \left\{ \int_0^y [c(z) - e_1] e^{-\frac{3\kappa(y-z)}{2}} \kappa dz - \int_y^L [c(z) - e_2] e^{-\frac{3\kappa(y-z)}{2}} \kappa dz \right\} \quad (2.16)$$

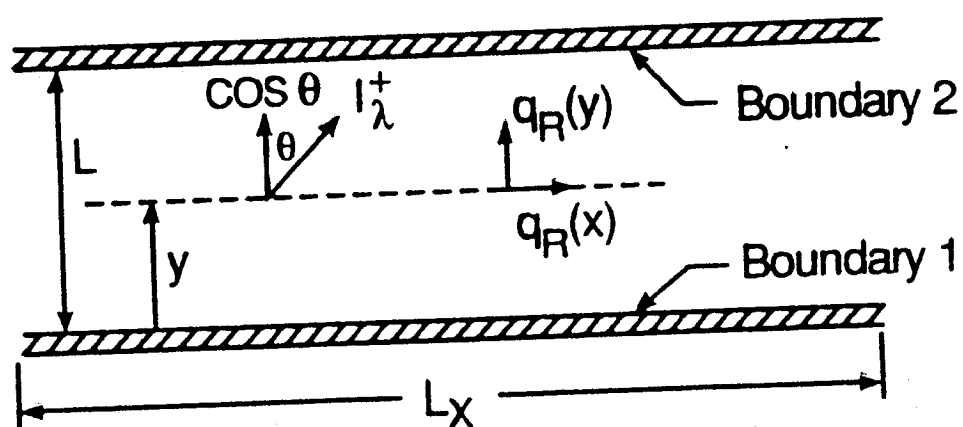


Fig. 2.2 Plane radiating layer between parallel boundaries

It is computationally more efficient to use Eq. (2.16) in the general energy equation than Eq. (2.15). This is because by differentiating Eq. (2.16) twice (using the Leibnitz formula) the integrals are eliminated and the following inhomogeneous ordinary differential equation is obtained:

$$\frac{1}{\kappa^2} \frac{d^2 q_R(y)}{dy^2} - \frac{9}{4} q_R(y) = \frac{3}{\kappa} \frac{dc(y)}{dy} \quad (2.17)$$

The solution of Eq. (2.17) requires two boundary conditions which are given for non-black diffuse surfaces as [8]

$$\left(\frac{1}{\epsilon_1} - \frac{1}{2} \right) [q_R(y)]_{y=0} - \frac{1}{3\kappa} \left[\frac{dq_R}{dy} \right]_{y=0} = 0 \quad (2.18a)$$

$$\left(\frac{1}{\epsilon_2} - \frac{1}{2} \right) [q_R(y)]_{y=L} + \frac{1}{3\kappa} \left[\frac{dq_R}{dy} \right]_{y=L} = 0 \quad (2.18b)$$

For black surfaces, the emissivity $\epsilon_1 = \epsilon_2 = 1$ and Eqs. (2.18) reduce to simpler forms.

An appropriate model for a gray gas absorption coefficient is required in Eqs. (2.16)-(2.18). This is represented by the Planck mean absorption coefficient, which is expressed for a multi-band system as [8, 22]

$$\kappa = \kappa_P = \frac{P_j}{\sigma T^4(y)} \sum_{i=1}^n \epsilon_{\omega_i}(T) S_i(T) \quad (2.19)$$

It should be noted that κ_P is a function of the temperature and the partial pressures P_j of the species.

2.5 Method of Solution

The flowfield in the combustor is represented by the Navier-Stokes equations and by the appropriate species continuity equations. The solution scheme is based on the SPARK code [2-4, 7, 20-22] available at NASA Langley Research Center. The finite-difference method using the explicit, unsplit MacCormack scheme [26] is used to solve

the governing equations. Incorporation of the finite-rate chemistry models into the fluid dynamic equations can create a set of stiff differential equations. Stiffness is due to a disparity in the time scales of the governing equations. In the time accurate solution, after the fast transients have decayed and the solutions are changing slowly, taking a larger time step is more efficient. But explicit methods still require small time steps to maintain stability. One way around this problem is to use a fully implicit method. However, this requires the inversion of a block multi-diagonal system of algebraic equations, which is also computationally expensive. The use of a semi-implicit technique [27, 28] provides an alternative to the above problems. This method treats the source term (which is the cause of the stiffness) implicitly, and solves the remaining terms explicitly.

The governing equations are transformed from the physical domain (x, y) to a computational domain (ξ, η) , using an algebraic grid generation technique similar to the one used by Smith and Weigel [29]. In the computational domain, Eq. (1) is expressed as [30]

$$\frac{\partial \hat{U}}{\partial t} + \frac{\partial \hat{F}}{\partial \xi} + \frac{\partial \hat{G}}{\partial \eta} + \hat{H} = 0 \quad (2.20)$$

where

$$\begin{aligned} \hat{U} &= UJ, \quad \hat{F} = Fy_{\eta} - Gx_{\eta} \\ \hat{G} &= Gx_{\xi} - Fy_{\xi}, \quad \hat{H} = HJ \\ J &= x_{\xi}y_{\eta} - y_{\xi}x_{\eta} \end{aligned} \quad (2.21)$$

Once the temporal discretization has been performed, the resulting system is spatially differenced using the explicit, unsplit MacCormack predictor-corrector scheme [26]. This results in a spatially and temporally discrete, simultaneous system of equations at each

grid point. Each simultaneous system is solved, subject to initial and boundary conditions, by using the Householder technique [31, 32]. At the supersonic inflow boundary, characteristic flow quantities are specified as freestream conditions. At the supersonic outflow boundary, non-reflective boundary conditions are used, i.e. flow quantities are extrapolated from interior grid points.

Chapter 3

PREMIXED THERMOCHEMICAL NONEQUILIBRIUM FLOWS

In this chapter, the thermochemical nonequilibrium phenomena pertaining to premixed, supersonic reacting flows are discussed. First, the relevant literature is reviewed, and then the physical models used in this study are described. This is followed by a description of the governing equations. After this, the method of solution is discussed.

3.1 Introduction

As stated in Chap. 2, in the case of premixed flows, the air and the fuel are thoroughly mixed in the required stoichiometric proportion, prior to combustion. This high enthalpy gaseous mixture characterized by very short residence times and wide temperature and pressure variations. This could lead to thermochemical nonequilibrium. In order for molecules to dissociate, they must be excited in all three energy states (rotational, translational and vibrational). After dissociation, the translational and rotational temperatures relax towards equilibrium faster than the vibrational temperature. This makes the study of vibrational nonequilibrium an important issue. Furthermore, the combustion of hydrogen and air in a scramjet combustor results in absorbing-emitting gases such as water vapor and hydroxyl radicals. Existence of such gases makes it necessary to consider the effect of radiative heat transfer.

In the presence of a radiation field, if the energy exchange is dominated by a collisional process, then the conditions of local thermodynamic equilibrium (LTE) exist. Otherwise, the system is considered to be in the state of non-local thermodynamic

equilibrium (non-LTE or NLTE). Further discussion on this is provided in the section on radiative interactions.

Several theoretical and computational studies on the nonequilibrium flow of air have been carried out [33–40]. Blythe [34, 35] carried out analytical studies of nonequilibrium flows in nozzles. Stollery and Park reported one of the first numerical solutions to the vibrational relaxation problem. Cheng and Lee [37] investigated freezing effects of chemical nonequilibrium flows in nozzles. A comprehensive review of the literature prior to 1968 was undertaken by Hall and Treanor [38]. Further numerical results for thermochemical nonequilibrium were discussed by Anderson [39, 40].

Vibrational relaxation effects are important in mixtures of combustng gases [41–43]. The relaxation rates of some gases were discussed by von Rosenberg et al. [41, 42] and by Kung and Center [43]. Vibrational relaxation effects are also important in lasers [44–47]. Kothari et al. [44] obtained numerical simulations for chemical lasers. Gas dynamic lasers were discussed by Anderson [45], by Reddy and Shanmugasundaram [46], and by Wada et al. [47].

In recent years, thermochemical nonequilibrium effects in atmospheric re-entry flows have received considerable attention [48–53]. Rakich et al. [48] studied flows over blunt bodies. Lee [49] discussed the basic governing equations. Gnoffo [50] developed the LAURA code for computing reentry flows. Candler and MacCormack [51] focused on ionization effects. Gnoffo et al. [52] comprehensively laid out the conservation equations for thermochemical nonequilibrium. Desideri et al. [53] discussed benchmark results of a workshop on hypersonic reentry flows.

The combustion of hydrogen and air in the scramjet combustor results in gases such as water vapor and hydroxyl radicals. It is known that the presence of water vapor gives

rise to rapid relaxation rates [41, 42, 54, 55]. Finzi et al. [54] and Center and Newton [55] investigated the vibrational relaxation effects of water vapor. The vibrational relaxation effects of hydrogen-air combustion have been very briefly touched upon recently by Grossmann and Cinella [56, 57].

Furthermore, water vapor is an absorbing-emitting gas. Existence of such gases makes it necessary to include the effect of radiation heat transfer. Coupled radiative transfer with chemical nonequilibrium has been studied earlier in Chap. 3 of this study. The effect of vibrational nonequilibrium upon radiative energy transfer in hot gases has also been investigated [58–61]. Tiwari and Cess [58] discussed a new formulation for the non-LTE radiation. Goody [59] studied radiation effects in the upper atmosphere. Coupled radiative and vibrational relaxation were discussed by Gilles and Vincenti [60]. Radiative cooling effects were investigated by Wang [61].

As this literature survey clearly indicates, there is a need for additional investigation in this critical area. The objective of this chapter is to study the coupled interaction of vibrational relaxation and radiative heat transfer, in the presence of finite rate chemical reactions. The thermal state of the gas is modeled using one translational-rotational temperature and five vibrational temperatures. The harmonic oscillator model is used in the formulation for vibrational relaxation. The radiative interactions are investigated in both streamwise and transverse directions. The tangent slab approximation is used in the radiative flux formulation. An optically thin assumption is made in the non-LTE model.

Two physical problems are considered for this study. The first one is reacting airflow in a hypersonic nozzle (Fig. 3.1), which is a benchmark case [53] used for code validation. Inlet reservoir conditions for this flow are $P_o = 1.53 \times 10^8 \text{ Pa}$, $T_o = 6500 \text{ K}$.

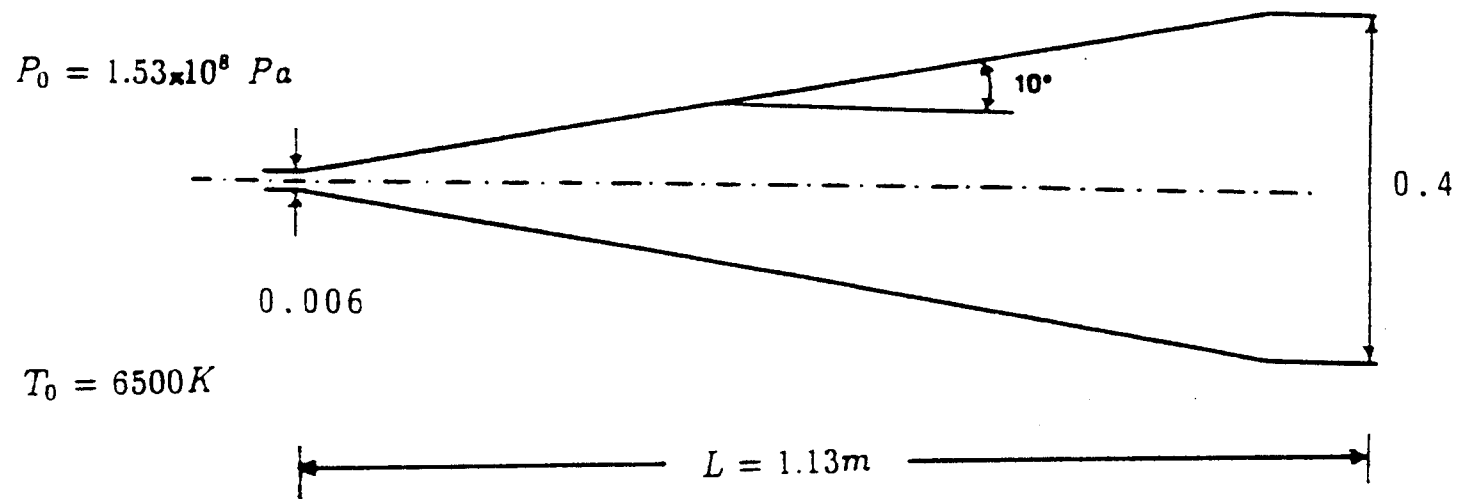


Fig. 3.1 Schematic diagram of nozzle for air chemistry

Based on validation of the code for the problem discussed above, the second physical problem considered is the supersonic flow of premixed hydrogen and air (stoichiometric equivalence ratio $\phi = 0.3$) in an expanding nozzle (Fig. 3.2). The physical dimension considered for obtaining results is $L_X = 2$ m. The flow is ignited by the high enthalpy of the flowfield. The inlet conditions which are representative of scramjet combustor exit conditions, are $P_\infty = 0.8046$ atm, $T_\infty = 1890$ K and $M_\infty = 1.4$. A one-dimensional flow has been computed by Grossmann and Cinella [56, 57].

3.2 Governing Equations

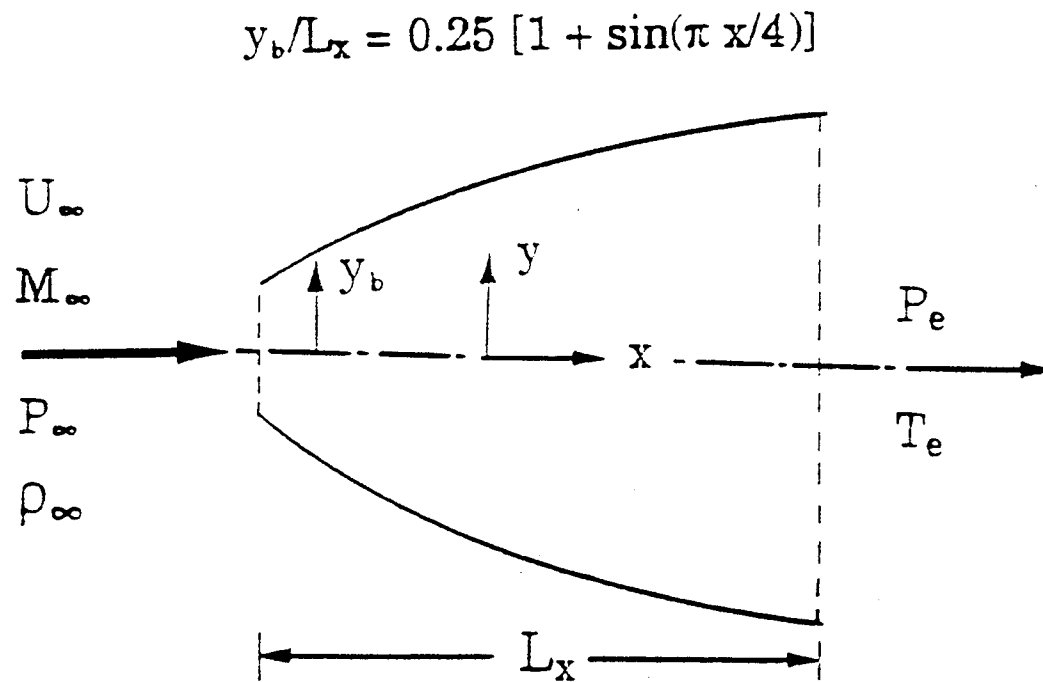
The Navier-Stokes and species continuity equations used in this study have already been discussed in Sec. 2.2 of previous Chap. 2. The additional governing equations, different from Eqs. (2.1) and (2.2), are described as

$$\begin{aligned}
 U &= \begin{bmatrix} \text{Eq. (2.2)} \\ \downarrow \\ \rho E_{Vj} \end{bmatrix} \\
 F &= \begin{bmatrix} \text{Eq. (2.2)} \\ \downarrow \\ \rho u E_{Vj} \end{bmatrix} \\
 G &= \begin{bmatrix} \text{Eq. (2.2)} \\ \downarrow \\ \rho v E_{Vj} \end{bmatrix} \\
 H &= \begin{bmatrix} \text{Eq. (2.2)} \\ \downarrow \\ -\dot{e}_j \end{bmatrix}
 \end{aligned} \tag{3.1}$$

The total internal energy E in Eq. (2.2) is modified as

$$E = -\frac{P}{\rho} + \frac{u^2 + v^2}{2} + \sum_{j=1}^m h_j f_j + \sum_{j=1}^m f_j E_{Vj} \tag{3.2}$$

where E_V is the total vibrational energy. Specific relations are needed for the chemistry and radiative flux terms. These are discussed in the following sections.



$$M_\infty = 1.4, P_\infty = 0.8046, T_\infty = 1890 \text{ K}, L_x = 2.0 \text{ m.}, \phi = 0.3$$

Fig. 3.2 Schematic diagram of nozzle for H_2 —air chemistry

The chemistry and thermodynamic model used in this study is the same as described in Sec. 2.3 of Chap. 2. A truncated 7-species, 7-step chemistry model, derived from Table 2.1, is used in this study. In order to account for the effect of vibrational relaxation on the chemical reaction rates, the equivalent temperature $T_{equiv.}$ in Eqs. (2.8)-(2.10) is expressed as [62]

$$T_{equiv.} = \sqrt{T \cdot T_V} \quad (3.3)$$

3.3 Thermal Nonequilibrium

A simplified thermodynamic model for the mixture of gases is necessary. Each species contains translational and rotational energy states in thermodynamic equilibrium and the vibrational energy is described by a harmonic oscillator, which is not in equilibrium [24, 62]. A Landau-Teller model is used to determine the effect of vibrational relaxation on the energy production. Furthermore, ionization effects are ignored. It should be noted that monoatomic species like O and H are not vibrationally excited.

For the range of temperatures considered in this study, a harmonic oscillator can be assumed. Accordingly, the vibrational source terms in Eq. (3.1) are expressed as

$$c_i = \frac{E_{Vi}^* - E_V}{\eta_{ci}} \quad (3.4)$$

where

$$E_{Vi}^* = \frac{R_i \theta_{vi}}{\exp(\theta_{vi}/T) - 1} \quad (3.5)$$

The asterisk * in Eq. (3.5) denotes the equilibrium value and

$$\theta_{vi} = \frac{\hbar c \omega_i}{k} \quad (3.6)$$

where $i = \text{H}_2, \text{O}_2, \text{H}_2\text{O}, \text{OH}$ and N_2 .

In Eq. (3.4), the equivalent relaxation time η_{ci} of a mixture of gases ($i = 1, j$) is given by the linear mixture rule [41, 42]

$$\frac{1}{\eta_{ci}} = \frac{f_1}{\eta_{ci1}} + \frac{f_2}{\eta_{ci2}} + \frac{f_3}{\eta_{ci3}} + \dots + \frac{f_j}{\eta_{cij}} \quad (3.7)$$

which accounts for the acceleration of vibrational relaxation observed in the presence of H₂O [41–43]. Analogy may also be drawn to electrical circuits, with resistors in parallel.

In Eq. (3.7), the local vibrational relaxation time η_{cij} of a molecular collision pair (i, j) is given by an empirical correlation [63], curve-fitted from experimental data as

$$\eta_{cij} = p^{-1} \exp[0.00116 \mu_{ij}^{1/4} \theta_{vi}^{4/3} (T^{-1/3} - 0.015 \mu_{ij}^{1/4}) - 18.42] \quad (3.8)$$

where

$$\mu_{ij} = \frac{\mu_{ii} \mu_{jj}}{\mu_{ii} + \mu_{jj}} \quad (3.9)$$

In Eq. (3.8), μ_{ij} is the effective molecular weight for a pair of colliding molecules (i, j). Values of θ_{vi} for N₂, O₂ and H₂O are obtained from [64] and for H₂ and OH from [65] and [66], respectively.

3.4 Radiative Interactions

Evaluation of the energy E in Eq. (2.2) requires an appropriate expression for the radiative flux term q_R . This radiation is emitted and absorbed by the “photon fluid” [60]. If the photon field is in equilibrium with the vibrational and translational fields, then the radiation is said to be of the Local Thermodynamic Equilibrium (LTE) type. This means that the LTE process is collision dominated. On the other hand, if the photon field also undergoes nonequilibrium, then the radiation is considered to be of the Non-local Thermodynamic Equilibrium (NLTE) type. This implies that the NLTE process is emission dominated.

3.4.1 Local Thermodynamic Equilibrium

The LTE radiative transfer model is the same as discussed in Sec. 2.4 of Chap. 2 and so it is not repeated here. This method of coupling the LTE radiation with the governing equations, is similar to a formulation discussed by Gokcen and Park [67].

3.4.2 Non-local Thermodynamic Equilibrium

The non-LTE radiation model is discussed here. Relevant information on relaxation processes, nonequilibrium transfer equations and radiative flux equations is provided in [58]. The basic equations developed can be used to investigate radiative interactions of gray as well as nongray gases under nonequilibrium conditions. In this study, however, the nonequilibrium radiative interactions are considered only in the optically thin conditions. A brief discussion of applicable equations is provided here.

The nonequilibrium radiative transfer equation for two level transitions between vibrational states may be written as [58–61]

$$\frac{dI_\omega}{ds} = \kappa_\omega(J_\omega - I_\omega) \quad (3.10)$$

where I_ω is the intensity of radiation. In Eq. (3.10), J_ω is the nonequilibrium source function and is defined as

$$J_\omega = B_\omega \left[\frac{\eta_r + \eta_c X}{\eta_r + \eta_c} \right] ;$$

$$X = \frac{\int d\Omega \int \kappa_\omega I_\omega d\omega}{(\int d\Omega \int \kappa_\omega B_\omega d\omega)} \quad (3.11)$$

where Ω is the solid angle, and B_ω is the black-body intensity of radiation. It should be noted that absorption is an equilibrium process, whereas the nonequilibrium influence comes only through the emission process (source function).

The time constant η_r in Eq. (3.11) is the radiative lifetime of vibrational states, and this is expressed as [58]

$$\frac{1}{\eta_r} = 8 c \omega^2 \left(\frac{P}{n} \right) S \quad (3.12)$$

where n denotes the number density of the radiating molecules and S represents the integrated band intensity of a vibration-rotation band.

The influence of nonequilibrium radiation is most apparent in the optically thin limit, wherein the divergence of the radiative flux can be expressed as [58]

$$\frac{dq_R}{d\xi} \left(1 + \frac{3}{4} \frac{\eta_c}{\eta_r} \right) = 3 A_o \mu_o [c_\omega(\xi) - c_{l\omega}(\xi)] \quad (3.13)$$

where A_o is the band width parameter and μ_o is the nondimensional path length, and these are defined in the cited references. It can be seen from Eq. (3.13) that the contribution of the non-LTE (non-local thermodynamic equilibrium) is obtained simply by adding a correction involving the nonequilibrium parameter $\frac{\eta_c}{\eta_r}$ to the divergence of the radiative flux.

3.5 Method of Solution

The method of solution used in this study is the same as discussed in Sec. 2.5 of Chap. 2. Additional details are presented in this section. Only the upper half of the flow domain is computed, as the flow is assumed to be symmetric about the centerline of a two-dimensional nozzle. The upper boundary is treated as a solid wall. This implies a no-slip boundary condition (i.e. zero velocities). The wall temperature and species mass fractions are extrapolated from interior grid points, by assuming an adiabatic, black and non-catalytic wall. The pressure is also extrapolated by using the boundary layer approximations for the pressure gradient. Symmetry boundary conditions are imposed at the lower boundary. Initial conditions are obtained by specifying freestream conditions

throughout the flowfield. The resulting set of equations is marched in time, until convergence is achieved. The details of the radiative flux formulation and method of solution are available elsewhere [22].

Chapter 4

NONPREMIXED NONEQUILIBRIUM FLOWS

In this chapter, the chemical nonequilibrium phenomena pertaining to non-premixed, supersonic, turbulent reacting flows are discussed. First, the relevant literature is reviewed, with a view towards presenting the problem statement and scope, as well as the physical models used. Then, the basic governing equations are described. This is followed by a discussion of the method of solution.

4.1 Introduction

In the case of non-premixed flows, engine efficiency is strongly influenced by turbulent mixing of the fuel and oxidizer and its effect on the chemical reactions. Also, the presence of absorbing-emitting species, like water vapor and hydroxyl radicals, implies the need to consider radiative heat transfer. The objective of this chapter is to study the coupled turbulence-chemistry-radiation interactions, in the presence of chemical nonequilibrium.

Several experimental and computational techniques have been developed towards a better understanding of the mixing and burning within a supersonic free shear layer or jet [3, 68]. The shear layer and the single jet simulate the parallel injection of hydrogen fuel in a scramjet engine without introducing complexities arising from the combustor geometry. Drummond [3] presented numerical solutions for a supersonic reacting mixing layer. Eklund et al. [68] discussed computational and experimental results for coaxial reacting jets.

A variety of turbulence models [69–74] can be applied to the analysis of the scramjet flowfield. These range from the simplest mixing length or zero-equation models, one-equation models and two-equation models, to the most general Reynolds stress turbulence closures. Eklund et al. [68] simulated subsonic diffusion flames using an algebraic turbulence model [2]. Due to the limitations of this turbulence model, the effects of fluctuations of the species concentrations and the temperature, were ignored. Jones and Whitelaw [69] showed that this underpredicted the extent of combustion. A Direct Numerical Simulation (DNS) of a reacting mixing layer has been carried out recently by Givi et al. [70]. The effects of temperature fluctuations was modelled using an assumed Probability Density Function (PDF) technique, proposed by Frankel et al. [71]. Narayan [72], Villasenor et al. [73] as well as Kolbe and Kollmann [74] have applied the two-equation models for simulating reacting mixing layers. While these are more sophisticated than algebraic models, they have been developed primarily for incompressible flows, using a gradient transport hypothesis.

Unfortunately, realistic engineering problems entail “non-gradient” transport [75–78]. This has been observed by Hinze [75], for incompressible flows, in measurements of the wake of an axisymmetric cylinder. In compressible flows, ‘counter-gradient’ diffusion has been observed experimentally by Moss [76]. Also, Libby and Bray [77] predicted that counter-gradient diffusion can occur due to the effect of the mean pressure gradient. The two-equation model (‘ $k-\epsilon$ ’ model) neglects terms involving pressure gradients. In addition to these shortcomings, the two-equation models cannot predict buoyancy effects and perform poorly for predicting swirling flows. These defects are eliminated with the differential Reynolds stress models, as suggested by Hogg and Leschziner [78].

The combustion of hydrogen and air in the scramjet combustor results in absorbing-emitting gases such as water vapor and hydroxyl radicals. Existence of such gases

makes the study of thermal radiation from turbulent reacting flows, an important issue. There are several models available in the literature to represent the absorption-emission characteristics of molecular gases as described by Mani and Tiwari [22]. Both pseudo-gray and non-gray gas models have been employed to evaluate the radiative heat transfer for supersonic combustion. Results of both models were compared and the pseudo-gray model was found to be computationally efficient. All these studies considered only laminar flows [22].

However, an important issue for turbulent flames is the effect of turbulence/radiation interactions [79–85]. The results obtained by Cox [79] shed some light on radiant heat transfer from turbulent flames. Tamanini [80] obtained numerical solutions for radiation on turbulent fire plumes. Kabashnikov and Kmit [81] investigated the influence of turbulent fluctuations on thermal radiation. Experimental data on turbulence/radiation interactions in diffusion flames were obtained by Gore et al. [82], and Jeng and Faeth [83]. Yuen et al. [84] discussed non-gray radiation in the presence of turbulence. Fairweather et al. [85] investigated radiative heat transfer from a turbulent reacting jet.

Second-order turbulence models have been applied recently to reacting as well as to compressible flows [86–88]. Chen [86] studied subsonic diffusion flames, using a Reynolds Stress model. Farschi [87] investigated heat release effects in reacting mixing layers, also using a second order model. Sarkar and Balakrishnan [89] applied a compressibility correction to the ϵ equation, and observed the correct decrease in growth rate of compressible mixing layers.

As seen from the above literature survey, there is clearly a need for additional investigation in this key field. The objective of the present study is to investigate turbulence-chemistry-radiation interactions in supersonic hydrogen-air diffusion flames.

The effects of turbulence on the chemistry and radiation heat transfer, are accounted for by using an assumed Beta-PDF method. The flowfield in the combustor is represented by the Navier-Stokes equations and by the appropriate species continuity equations. The finite difference method using the explicit, unsplit MacCormack scheme is used to solve the governing equations. A truncated 7-step finite rate chemistry model, derived from the complete mechanism (Table 2.1) is used here. The radiation model used in this study is the same as discussed in Sec. 2.4 of Chap. 2.

The physical models used in this study are the Beach and Jarrett-Pitz coaxial jets experiments [89, 90]. A schematic diagram of these coaxial jets experiments is given in Fig. 4.1, wherein an inner fuel jet diffuses into an outer air jet. This outer jet is vitiated with water vapor to enhance the combustion process. The temperature and other exit conditions for the Beach case are given in Table 4.1. The temperature and other exit conditions for the Jarrett-Pitz experiment are given in Table 4.2. Diagnostics for the Jarrett case could be more reliable, since the Beach experiment is older by a decade.

4.2 Basic Governing Equations

The physical model for analyzing the flowfield in a supersonic combustor is described by the Navier-Stokes and species continuity equations [1, 2]. Favre-averaging is used to derive the turbulent flow equations from the Navier-Stokes equations. This is carried out as

$$\phi = \tilde{\phi} + \phi' \quad (4.1)$$

where the mean is expressed as

$$\tilde{\phi} = \frac{\overline{\rho\phi}}{\bar{\rho}} \quad (4.2)$$

and ϕ denotes u , v , T and f_j .

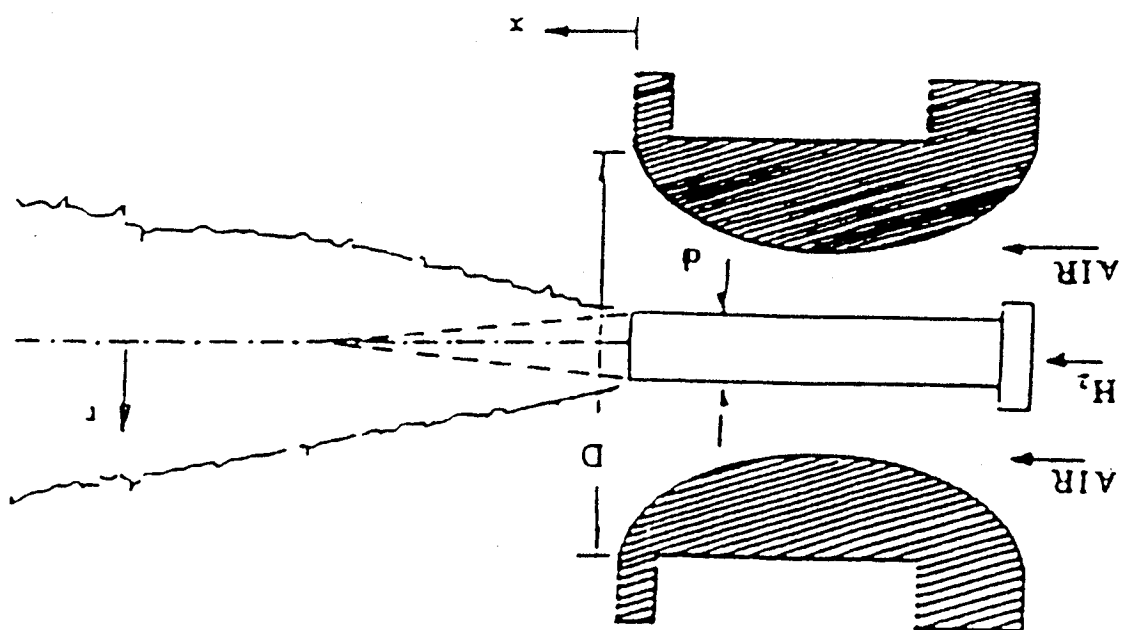


Fig. 4.1 Schematic of the coaxial jet flowfield

Table 4.1 Conditions for the Beach experiment

	H ₂	Air
Mach No.	2.0	1.9
Temperature	251 K	1495 K
Pressure	0.1 MPa	0.1 MPa
Velocity	2418 m/s	1510 m/s
f-H ₂	1.0	0.0
f-O ₂	0.0	0.241
f-N ₂	0.0	0.478
f-H ₂ O	0.0	0.281

Fuel injector inner diameter, $d = 0.009525$ m.

Injector lip thickness = 0.0015 m.

Nozzle diameter, $D = 0.0653$ m.

Table 4.2 Conditions for the Jarrett-Pitz experiment

	Hydrogen jet (inner)	Air jet (outer)	Ambient Air
Mach No.	1.0	2.02	0.0
Temperature	545 K	1250 K	273 K
Velocity	1772 m/s	1441 m/s	0
Pressure	0.112 MPa	0.096 MPa	0.101 MPa
f-H ₂	1.0	0.0	0.0
f-O ₂	0.0	0.254	0.233
f-N ₂	0.0	0.572	0.767
f-H ₂ O	0.0	0.174	0.0

Fuel injector inner diameter, $d = 0.00236$ m.

Injector lip thickness = 0.00145 m.

Nozzle diameter, $D = 0.01778$ m.

The density and pressure are time-averaged and are expressed as

$$\begin{aligned}\rho &= \bar{\rho} + \rho'' \\ p &= \bar{p} + p''\end{aligned}\quad (4.3)$$

where by definition

$$\overline{\rho\phi'} = 0 \quad (4.4)$$

and

$$\begin{aligned}\overline{\rho''} &= 0 \\ \overline{p''} &= 0\end{aligned}\quad (4.5)$$

A relationship between time-averaged and density-weighted variables can be obtained

as

$$\tilde{\phi} - \bar{\phi} = \frac{\overline{\rho''\phi'}}{\bar{\rho}} \quad (4.6)$$

This leads to the averaged continuity, momentum and energy equations being expressed in tensor notation as [88]

$$\frac{\partial \rho}{\partial t} + \frac{\partial(\bar{\rho}\tilde{u}_j)}{\partial x_j} = 0 \quad (4.7)$$

$$\begin{aligned}\frac{\partial(\bar{\rho}\tilde{u}_i)}{\partial t} + \frac{\partial(\bar{\rho}\tilde{u}_i\tilde{u}_j)}{\partial x_j} &= -\frac{\partial p}{\partial x_i} \\ &+ \frac{\partial(\bar{\tau}_{ij} - \overline{\rho u'_i u'_j})}{\partial x_j}\end{aligned}\quad (4.8)$$

and

$$\begin{aligned}
 \frac{\partial(\bar{\rho}\tilde{E})}{\partial t} + \frac{\partial(\bar{\rho}\tilde{E}\tilde{u}_j)}{\partial x_j} &= \frac{\partial(-\tilde{u}_j\tau_{ij} - \bar{p}\tilde{u}_j - \bar{p}\tilde{u}'_i - \bar{q}_j - \overline{qR_j})}{\partial x_j} \\
 &+ \frac{\partial(-\overline{u'_j\tau'_{ij}} - \overline{u'_jp''} - \bar{\rho}\tilde{E}'u'_j)}{\partial x_j}
 \end{aligned} \quad (4.9)$$

where the mean heat flux is expressed as

$$\bar{q}_i = -\psi \frac{\partial \tilde{T}}{\partial x_i} \quad (4.10)$$

and the turbulent energy flux $\tilde{E}'u'$ can be obtained as,

$$\begin{aligned}
 \tilde{E}'u'_j &= -C_V \tilde{T}'u'_j + \tilde{u}_i \tilde{u}'_j u'_i \\
 &+ \frac{\overline{u'_i u'_i u'_j}}{2} + \sum_{k=1}^m \tilde{h}_k \tilde{f}'_k u'_j
 \end{aligned} \quad (4.11)$$

The averaged species equations in tensor notation are obtained as

$$\begin{aligned}
 \frac{\partial(\bar{\rho}\tilde{f}_k)}{\partial t} + \frac{\partial(\bar{\rho}\tilde{f}_k\tilde{u}_j)}{\partial x_j} &= \frac{\partial\left[D\bar{\rho}\frac{\partial\tilde{f}_k}{\partial x_j} - \bar{\rho}\tilde{f}'_k u'_j\right]}{\partial x_j} \\
 &+ \frac{\partial\left(D\bar{\rho}\frac{\partial\tilde{f}'_k}{\partial x_j}\right)}{\partial x_j} + \tilde{w}_k
 \end{aligned} \quad (4.12)$$

In order to close Eqs. (4.7)-(4.12), it is necessary to provide models or modelled transport equations for the following quantities :

- the Reynolds stress tensor $\tilde{u}'_i \tilde{u}'_j$ in Eq. (4.8)
- the turbulent heat flux $\tilde{T}'u'$ in Eq. (4.11)
- the turbulent mass flux $\overline{\rho''u'_i}$, the turbulent temperature flux $\overline{\rho''T'}$, and the turbulent species flux $\overline{\rho''f'_k}$, all appearing in Eq. (4.6)
- the turbulent species mass flux $\tilde{u}'_j \tilde{f}'_k$ in Eq. (4.12)
- the mean chemical species production term \tilde{w}_k in Eq. (4.12).

Other terms such as $\overline{\tau''_{ij} u'_j}$ in Eq. (4.9), are neglected in high Reynolds number turbulence.

4.3 Reynolds Stress Turbulence Model

The exact transport equation for the Reynolds stress $\widetilde{u'_i u'_j}$ can be obtained as [75, 88]

$$\begin{aligned}
 & \frac{\partial(\overline{\rho u'_i u'_j})}{\partial t} + \frac{\partial(\overline{u_k \rho u'_i u'_j})}{\partial x_k} = \\
 & \underbrace{-\overline{\rho u'_i u'_k} \frac{\partial \widetilde{u_j}}{\partial x_k} - \overline{\rho u'_j u'_k} \frac{\partial \widetilde{u_i}}{\partial x_k}}_{\text{Term I}} \\
 & \underbrace{+ \overline{u'_j} \frac{\partial \tau_{ik}}{\partial x_k} + \overline{u'_i} \frac{\partial \tau_{jk}}{\partial x_k}}_{\text{Term II}} - \underbrace{\frac{\partial(\overline{\rho u'_i u'_j u'_k})}{\partial x_k}}_{\text{Term III}} \\
 & \underbrace{- \overline{u'_j} \frac{\partial p}{\partial x_i} - \overline{u'_i} \frac{\partial p}{\partial x_j}}_{\text{Term IV}}
 \end{aligned} \tag{4.13}$$

where *Term I* is the production term, i.e.,

$$P_{ij} = \text{Term I} \tag{4.14}$$

and *Term II* is the viscous dissipation term ϵ_{ij} which is modelled as [88]

$$\epsilon_{ij} = \frac{2}{3} \bar{\rho} \epsilon (1 + M_t^2) \delta_{ij} \tag{4.15}$$

In Eq. (4.15), the turbulent Mach number is defined as [88]

$$M_t = \sqrt{\frac{\widetilde{u'^2} + \widetilde{v'^2} + \widetilde{w'^2}}{\gamma R T}} \tag{4.16}$$

The term ϵ is computed from a transport equation as [88]

$$\begin{aligned}
 & \frac{\partial(\bar{\rho} \epsilon)}{\partial t} + \frac{\partial(\bar{\rho} \widetilde{u_k} \epsilon)}{\partial x_k} = C_{\epsilon 1} \frac{\epsilon}{k} \bar{\rho} \widetilde{u'_i u'_j} u'_k \\
 & - C_{\epsilon 2} \bar{\rho} \frac{\epsilon^2}{k} + \frac{\partial\left(C_{\epsilon} \bar{\rho} \frac{k}{\epsilon} \widetilde{u'_k u'_l} \frac{\partial \epsilon}{\partial x_l}\right)}{\partial x_k}
 \end{aligned} \tag{4.17}$$

where the model coefficients have the following values :

$$C_{c1} = 1.41, C_{c2} = 1.90, C_c = 0.15 \quad (4.18)$$

Term III in Eq. (4.13) is the diffusive transport term $T_{ijk,k}$ and is modelled as

$$\begin{aligned} T_{ijk,k} = & -C_s \bar{\rho} \frac{(q^2)^2}{\epsilon} \left[\left(\frac{\partial (\widetilde{u_i' u_j'})}{\partial x_k} \right) \right. \\ & \left. + \left(\frac{\partial (\widetilde{u_j' u_k'})}{\partial x_i} \right) + \left(\frac{\partial (\widetilde{u_i' u_k'})}{\partial x_j} \right) \right] \end{aligned} \quad (4.19)$$

where $C_s = 0.018$.

The last *Term IV* in Eq. (4.13) can be expressed as the sum of a pressure-strain term Π_{ij} and a mean pressure gradient term, details of which are given in [88]. The Launder-Reece-Rodi (LRR) model is applied to the pressure-strain term Π_{ij} , and is expressed as

$$\Pi_{ij} = C_1 \rho \epsilon \left[\frac{\widetilde{u_i' u_j'}}{2k} - \frac{1}{3} \delta_{ij} \right] - C_3 \left[P_{ij} - \frac{1}{3} P_{kk} \right] \quad (4.20)$$

where $C_1 = 3.0$, $C_3 = 0.6$ and P_{ij} is given by Eqs. (4.13–4.14).

The turbulent heat flux term in Eq. (4.11) is modelled as a gradient transport term,

$$\widetilde{T' u_i'} = -\frac{C_\mu k^2}{c_\chi T} \frac{\partial \widetilde{T}}{\partial x_i} \quad (4.21)$$

where $C_\mu = 0.09$.

The turbulent species flux $\widetilde{u_j' f_k'}$ in Eq. (4.12), and the turbulent mass flux $\overline{\rho'' u_i'}$, the turbulent temperature flux $\overline{\rho'' T'}$, as well as the turbulent species flux $\overline{\rho'' f_k'}$, all appearing in Eq. (4.6), are modelled using the gradient transport method from Eq. (4.21), e.g.

$$\widetilde{\rho'' f_k'} = -\frac{C_\mu k^2}{c_\chi} \frac{\partial \widetilde{f_k}}{\partial x_i} \quad (4.22)$$

The mean chemical species production term \widetilde{w}_k in Eq. (4.12), is modelled using an assumed Beta-PDF for the temperature fluctuations, i.e.,

$$\widetilde{w}_k = \int_{-\infty}^{+\infty} w_k \cdot P(T') dT' \quad (4.23)$$

The Beta-PDF is preferred over other distributions because it closely approximates the actual DNS simulation of scalar mixing, and is expressed as

$$P(T') = \frac{T_0^{\alpha-1} (1 - T_0)^{\beta-1} \Gamma(\alpha + \beta)}{\Gamma(\alpha) \Gamma(\beta)} \quad (4.24)$$

where

$$\alpha = \widetilde{T}_0 \left(\frac{\widetilde{T}_0 (1 - \widetilde{T}_0)}{\widetilde{T}_0'^2} - 1 \right) \quad (4.25a)$$

$$\beta = (1 - \widetilde{T}_0) \left[\frac{\widetilde{T}_0 (1 - \widetilde{T}_0)}{\widetilde{T}_0'^2} - 1 \right] \quad (4.25b)$$

The quantity $\widetilde{T}_0'^2$ is the variance of the Beta-PDF, detail of which are given in Sec. 5.3, and Γ is the standard gamma function. Since probability space recognizes only values from 0 to 1, it is necessary to normalize the mean temperature in Eq. (4.25) as

$$\widetilde{T}_0 = \frac{\widetilde{T} - \widetilde{T}_{\min}}{\widetilde{T}_{\max} - \widetilde{T}_{\min}} \quad (4.26)$$

A very similar analysis can be carried out for the Beta PDF for species fluctuations.

4.4 Radiative Interactions

The radiative heat transfer model used in this study is the same as discussed in Sec. 2.4 of Chap. 2. Therefore, the relevant details need not be repeated here.

In the present study, the mean q_R term in Eq. (4.9) is modeled as

$$\widetilde{q}_R = \int_{-\infty}^{+\infty} q_R \cdot P(T') dT' \quad (4.27)$$

where the PDF, $P(T')$ is given by Eqs. (4.24)-(4.26). Equation (4.27) is a new and simple formulation for the coupled turbulence/radiation interactions.

4.5 Method of Solution

The method of solution used in this study is the same as discussed in Sec. 2.5 of Chap. 2. Additional details are presented in this section. The upper boundary is treated as a free boundary, wherein the gradients of all variables vanish. The lower boundary is the centerline of the axisymmetric flow. Consequently, the normal velocity is zero, on the centerline. The gradients of all remaining variables on the centerline vanish by symmetry. Initial conditions are obtained by specifying freestream conditions throughout the flowfield. An isotropic turbulent shear stress was prescribed as the initial condition for the Reynolds Stress equations. The resulting set of equations is marched in time, until convergence is achieved. The details of the radiative flux formulation and method of solution are available in Mani and Tiwari [22].

Chapter 5

RESULTS AND DISCUSSION

The theoretical formulations described in Chaps. 2, 3 and 4 are applied to obtain results for nonequilibrium processes in supersonic combustion. The explicit MacCormack technique has been used to march the governing equations in time, until convergence is achieved. The two-dimensional Navier-Stokes equations are solved for supersonic flows with nonequilibrium chemistry and thermodynamics, coupled with radiation, for hydrogen-air systems. This computer program is an extension of the original SPARK code [2, 3]. Results for the impact of chemical kinetics on radiative interactions are discussed first, followed by the results for the interaction of thermochemical nonequilibrium and radiative heat transfer. Results for the turbulence-chemistry as well as the turbulence-radiation interactions are presented in the third and fourth parts of this chapter.

5.1 Chemical Nonequilibrium and Radiative Interactions

Studies were conducted to investigate the extent of radiative heat transfer in supersonic flows undergoing hydrogen-air chemical reactions, using three chemical kinetics models. These chemistry mechanisms account for an increasing number of reactions and participating species. For the temperature range considered in this study, the important radiating species are OH and H₂O. The gray gas formulations are based on the Planck mean absorption coefficient which accounts for detailed information on different molecular bands. The radiative fluxes have been computed using this "pseudo-gray" formulation. The justification for using this model is provide in Mani and Tiwari [22]. The

three chemistry models are obtained from Table 2.1. The 2-step model is given at the bottom of that table. The first 18 reactions in this table constitute the 18-step model. The remaining 17 reactions Nos. (19)–(35) complete the 35-step model. The two-dimensional problem considered in this study is shown in Fig. 2.1.

Figures 5.1–5.4 show the computed results using a 61×61 grid, for temperature and pressure as well as H_2O and OH species mass fractions. The oblique shock igniting the air-fuel mixture, arises from the compression corner at the lower wall (Fig. 2.1). The hottest regions in the flowfield are in the upper and lower wall boundary layers. Figures 5.1 and 5.2 show the effect of the three chemistry models on the temperature and pressure profiles, varying along x at the location $y = 0.02$ cm. from the lower wall (boundary layer region). The temperatures in the boundary layer show a gradual increase (Fig. 5.1). The pressure profiles are plotted at $y = 0.13$ cm. (inviscid region) and show a sharp increase due to the shock (Fig. 5.2).

The ignition phase discrepancy of the three chemistry models can be seen in Figs. 5.3 and 5.4. The shock is occurring after $x/L_x = 0.3$. However, the 2-step model predicts ignition before the shock (shorter ignition delay) due to the high temperature in the boundary layer. On the other hand, the 18-step model predicts a longer ignition delay, at $x/L_x = 0.43$ (Fig. 5.3). The 35-step model's prediction of ignition delay appears to be an average of the other two models. Although the three models do not differ much in prediction of temperature and pressure profiles, they do differ significantly in predictions of species mass fractions (Fig. 5.4).

In order to resolve this discrepancy, a grid sensitivity study was carried out to examine whether the grid size affects the flow predictions. The results of three grid distributions 31×31 , 61×61 and 81×81 are shown in Fig. 5.5, and it appears that the 61×61 grid is

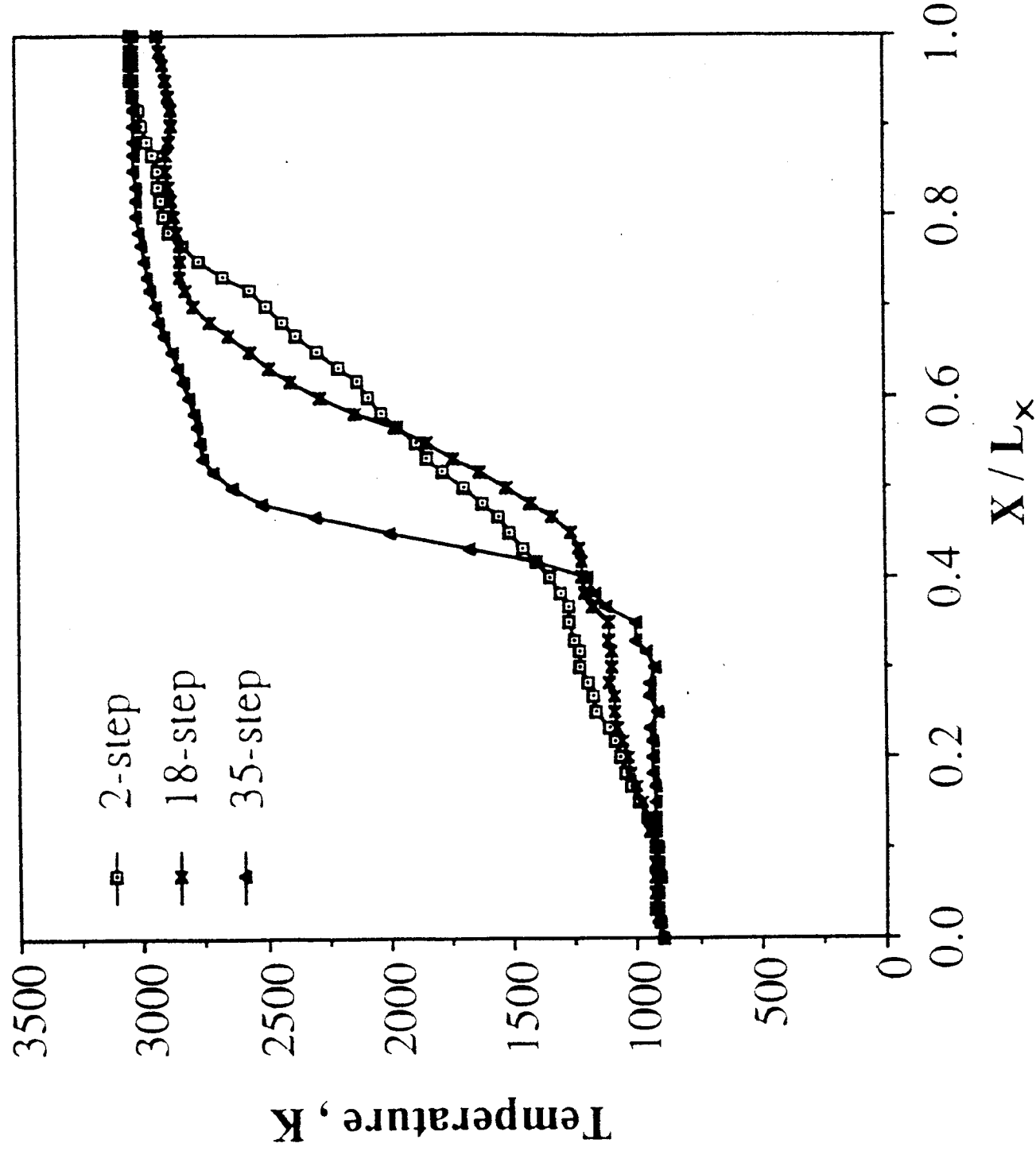


Fig. 5.1 Temperature profiles

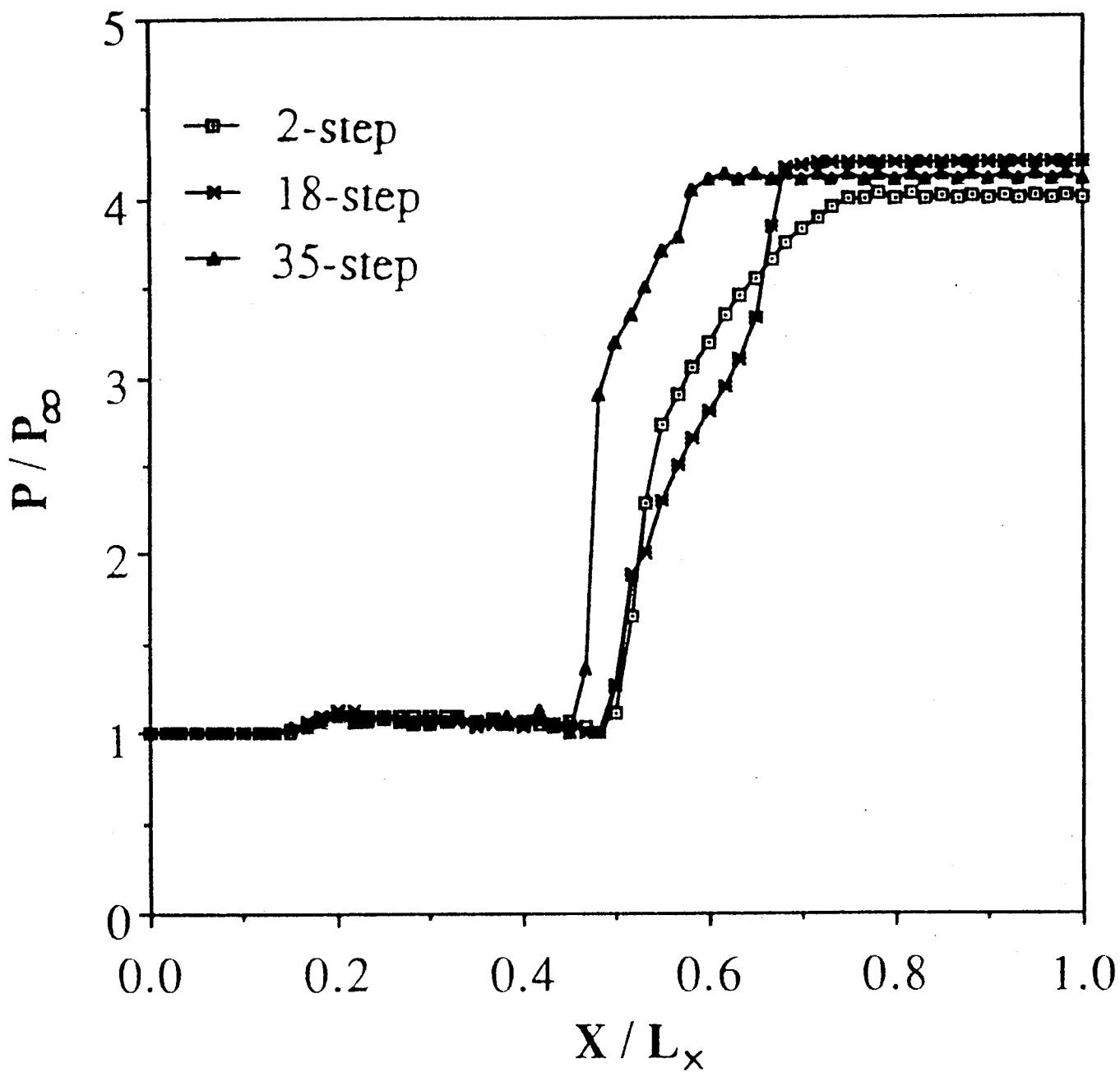
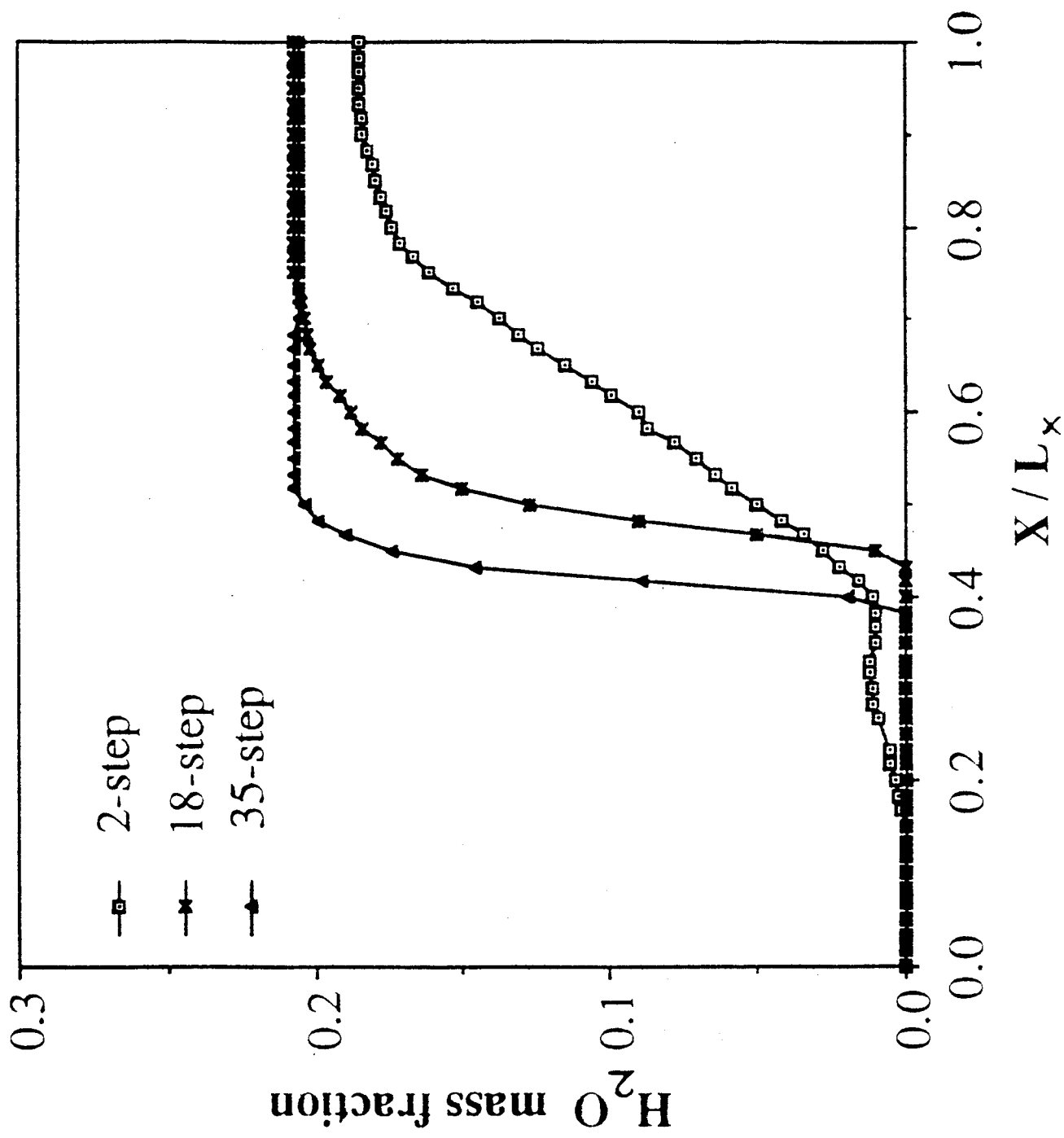


Fig. 5.2 Pressure profiles ($y=0.13$ cm.)

Fig. 5.3 H₂O mass fraction profiles

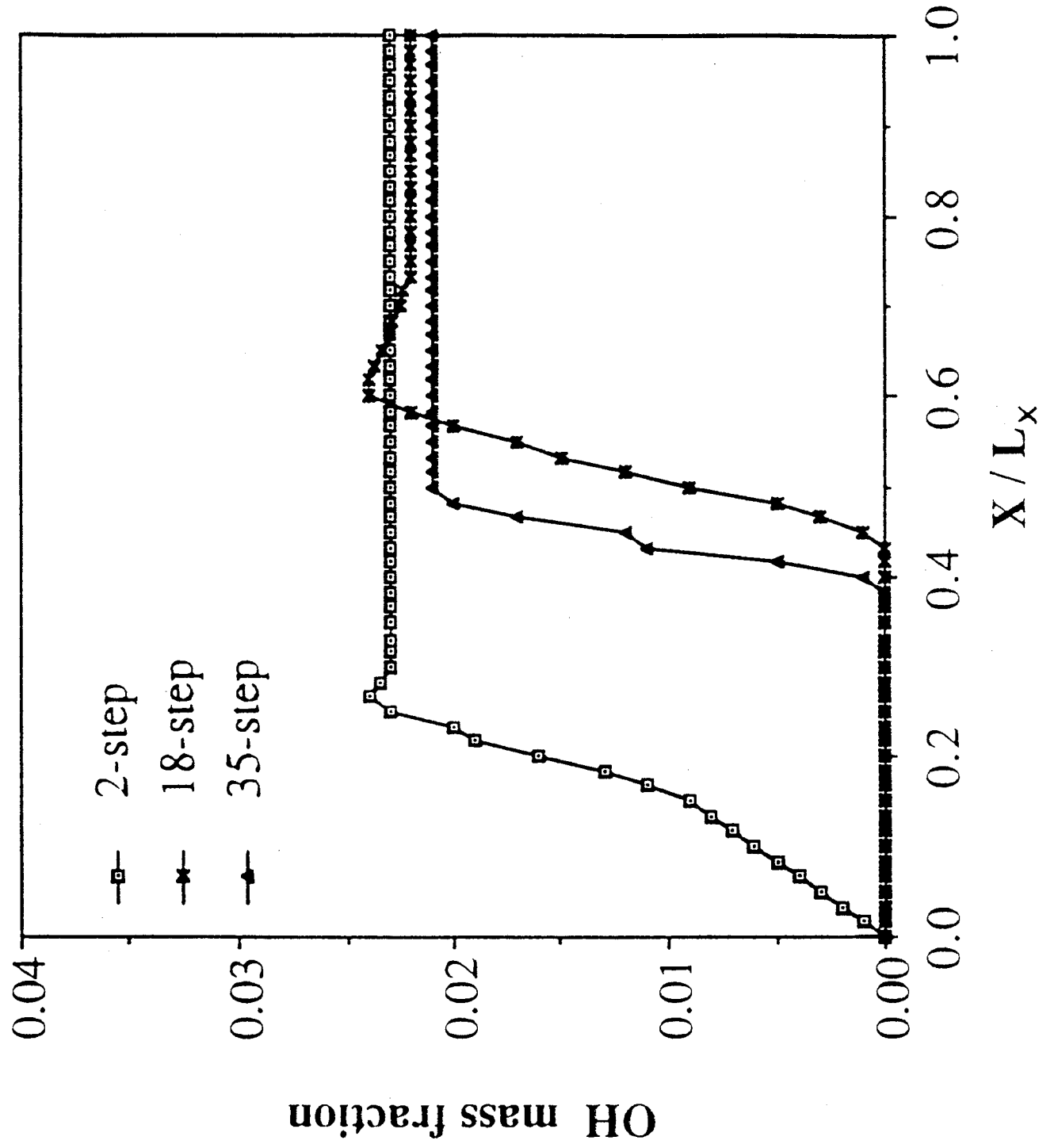


Fig. 5.4 OH mass fraction profiles

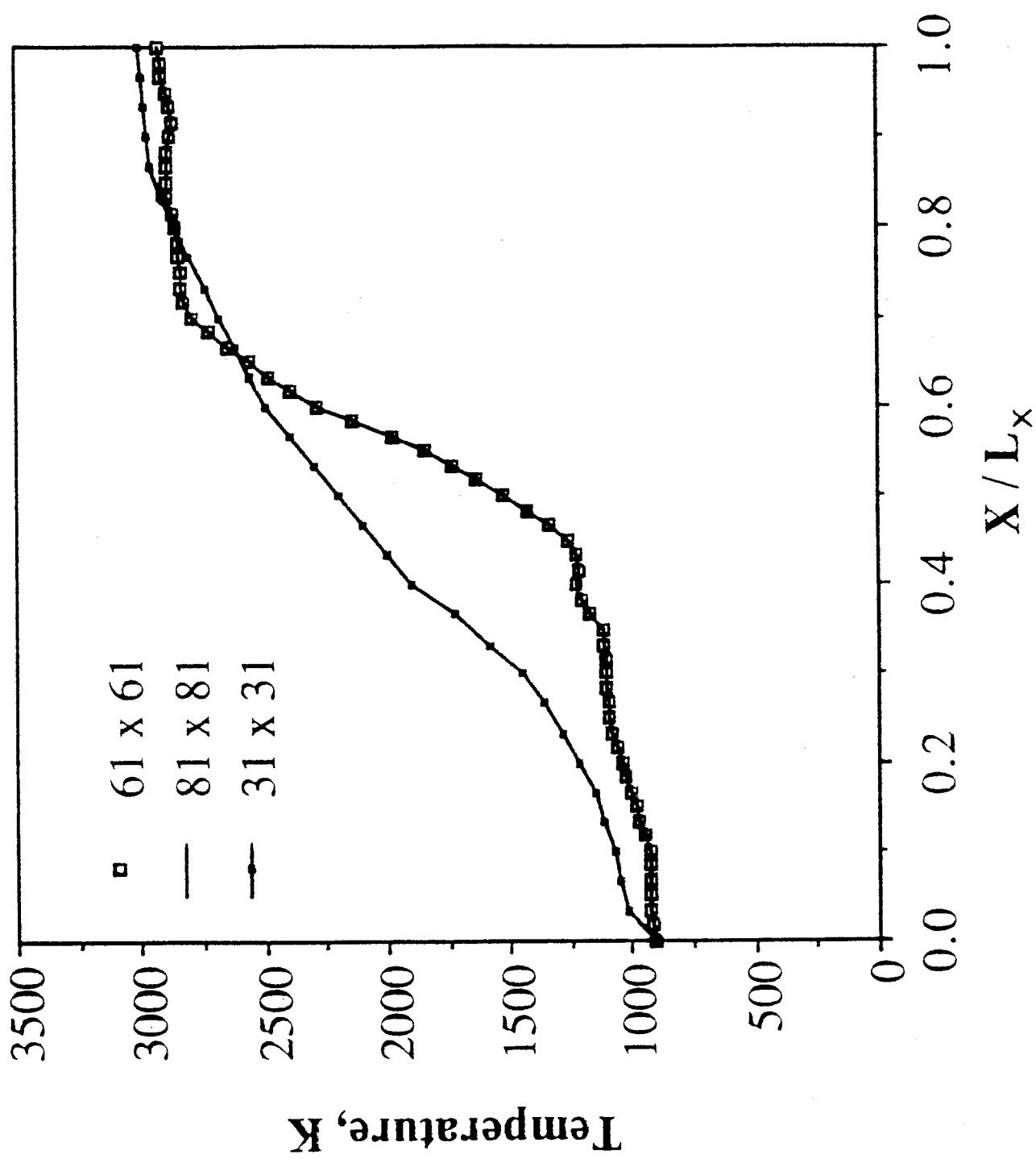


Fig. 5.5 Grid sensitivity results

sufficient for the present study. The grid points are concentrated in the boundary layer and shock regions.

The reasons for the varying predictions of species mass fraction by the three chemistry models was examined further and the results are shown in Figs. 5.6 and 5.7. Figure 5.6 shows that the reaction No. 8 in Table 2.1 is critical in determining the extent of chemical heat release and H_2O production. Reaction No. 8 deals with production of HO_2 radical. This reaction is absent from the 2-step model, while it is common to both the 18-step and 35-step models. Figure 5.6 shows that the 35-step model experiences nearly a 30% drop in temperature in the middle of the channel when the rate of reaction No. 8 is reduced by a factor of 1000 (effectively cutting of the production of the HO_2 radical). In contrast, the 18-step model shows a 15% drop in temperature, when subjected to the same reduction in the rate of reaction No. 8. This shows that the reaction No. 8 controls the overall H_2O production occurring in Table 2.1. Due to the high temperatures (~ 3000 K) in the flowfield, there is a pool of highly reactive free radicals like H, O, etc. The HO_2 radical is converted to the very reactive OH radical, by the free radicals (reaction Nos. 11 and 12). This establishes the HO_2 radical as a very important species in promoting flame propagation in hydrogen-air flames. A similar reaction sensitivity analysis has been carried out in [91]. Since the 2-step model does not have the HO_2 radical, it predicts lesser amounts of OH and H_2O .

It was necessary to determine the reason for the higher sensitivity of the 35-step model to the HO_2 radical, as compared to the 18-step model. Figure 5.7 shows that the reaction Nos. 21 and 23 in Table 2.1 are critical in determining the extent of chemical heat release and H_2O production. Reaction Nos. 21 and 23 deal with production of the NO radical. These reactions are absent from the 2-step and 18-step models, whereas they play an important role in the 35-step model. Figure 5.7 shows that the 35-step model

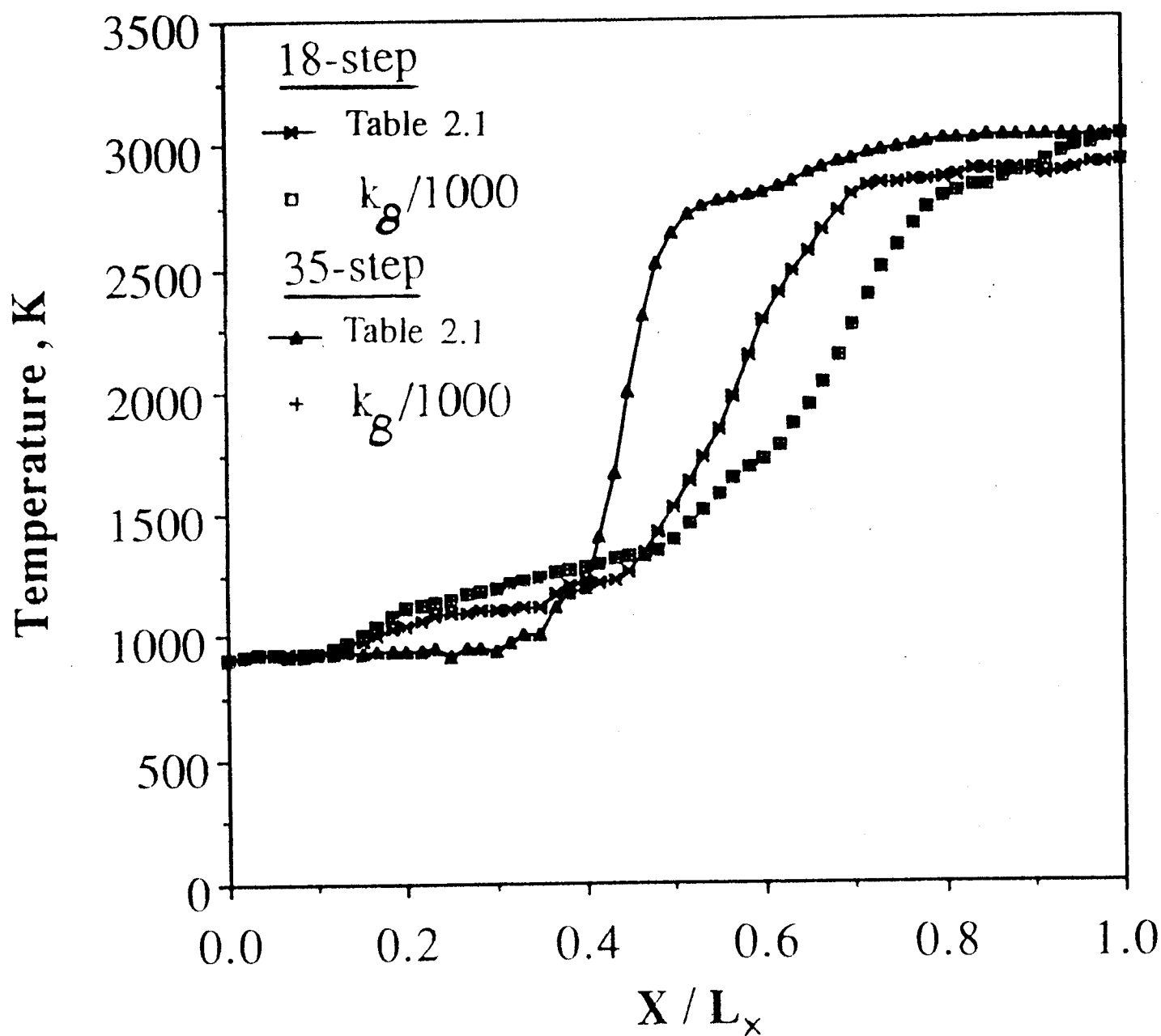


Fig. 5.6 Effect of reaction rates

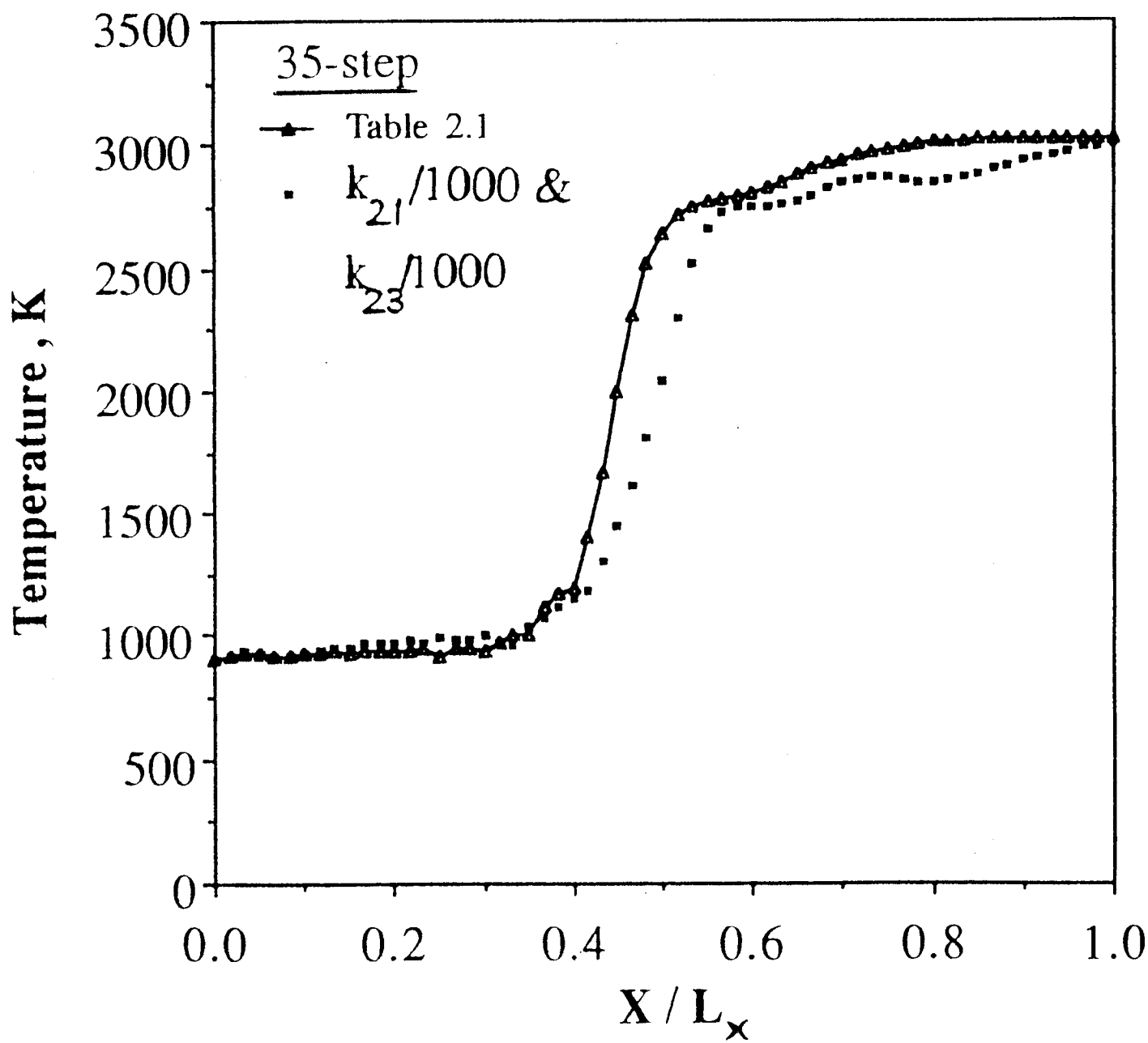


Fig. 5.7 Effect of NO and HO₂ reactions

undergoes a 10% reduction in temperature, when the rates of reaction Nos. 21 and 23 are reduced by a factor of 1000 (effectively cutting off the production of the NO radical). Due to the high temperatures in the flowfield, the usually inert nitrogen dissociates into the highly reactive N free radical. This free radical N is then oxidized in reaction Nos. 21 and 23, thereby producing the NO radical. This NO radical converts the HO₂ radical into the highly reactive OH radical, through reaction No. 29. This confirms that the NO radical is a very important species for flame propagation in a hydrogen-fueled supersonic combustor. Since the 35-step model has the NO radical, it predicts higher amounts of OH and H₂O than the 18-step model.

Based on the above understanding of the chemical kinetics of supersonic hydrogen-air flames, the radiative interactions were examined. Figure 5.8 shows the profiles of the normalized streamwise radiative flux q_{Rx} predicted by the three chemistry models, along the location $y = 0.02$ cm. from the lower wall. The q_{Rx} flux reduces towards the end of the channel due to cancellation of fluxes in positive and negative directions. It is seen from Fig. 5.8 that the 18-step and 35-step models predict significantly higher amounts of q_{Rx} (50% more and 100% more, respectively) than the 2-step model. This is because radiative heat transfer is a strong function of temperature, pressure and species concentrations. So, the larger values of radiative fluxes are caused by higher amounts of H₂O concentrations, which in turn, depend on reactions involving HO₂ and NO species. Figure 5.9 shows the variations in the normal radiative flux q_{Ry} along x , at the location $y = 0.02$ cm. from the lower wall. These do not appear to vary significantly between the three chemistry models. However, in all three cases, the q_{Ry} value increases rapidly after the shock.

Figures 5.10–5.13 show the computed results for reacting flows with and without radiation, for the three chemistry models. It is seen that the 2-step model shows only

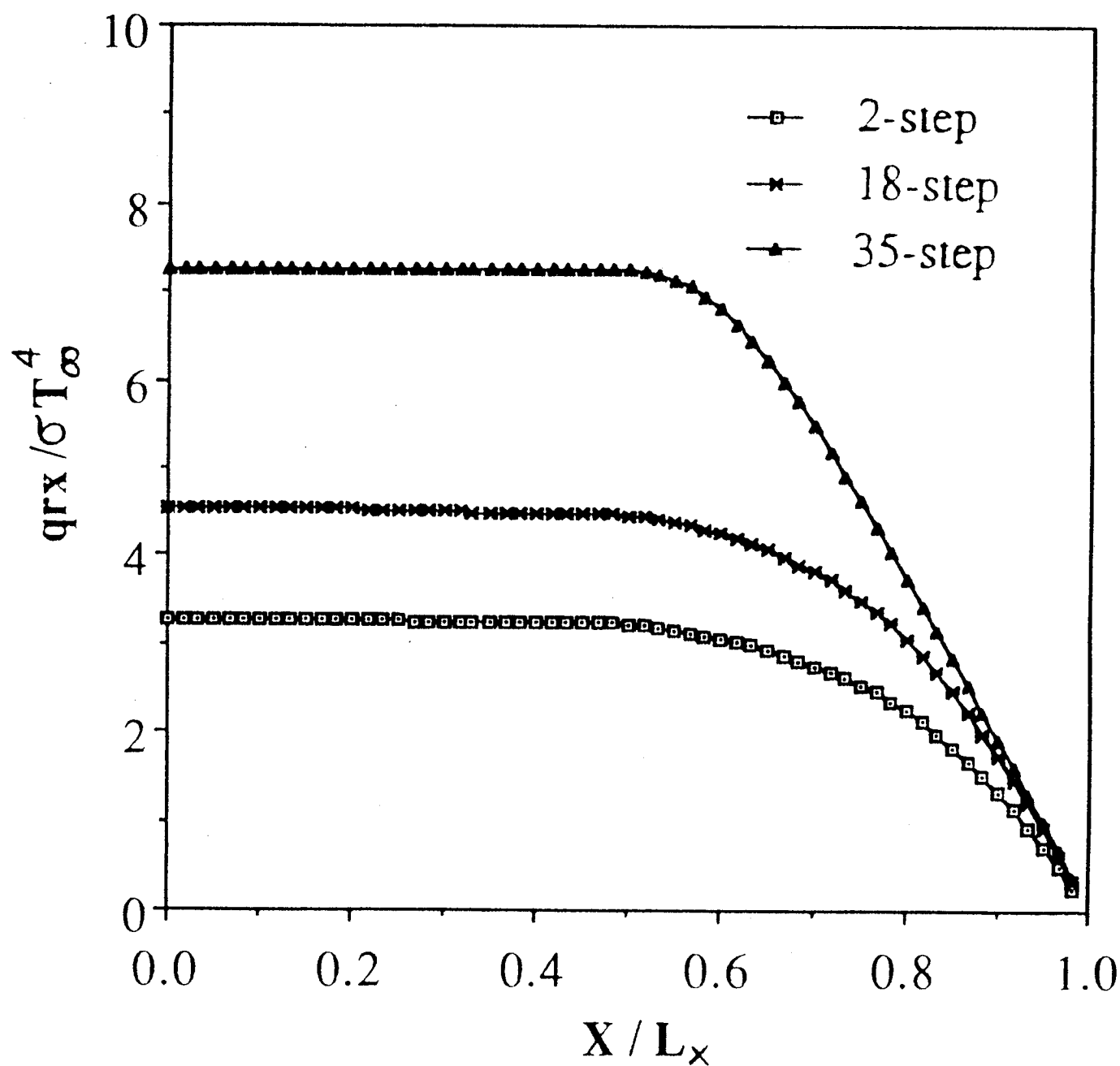


Fig. 5.8 Profiles of streamwise radiative flux

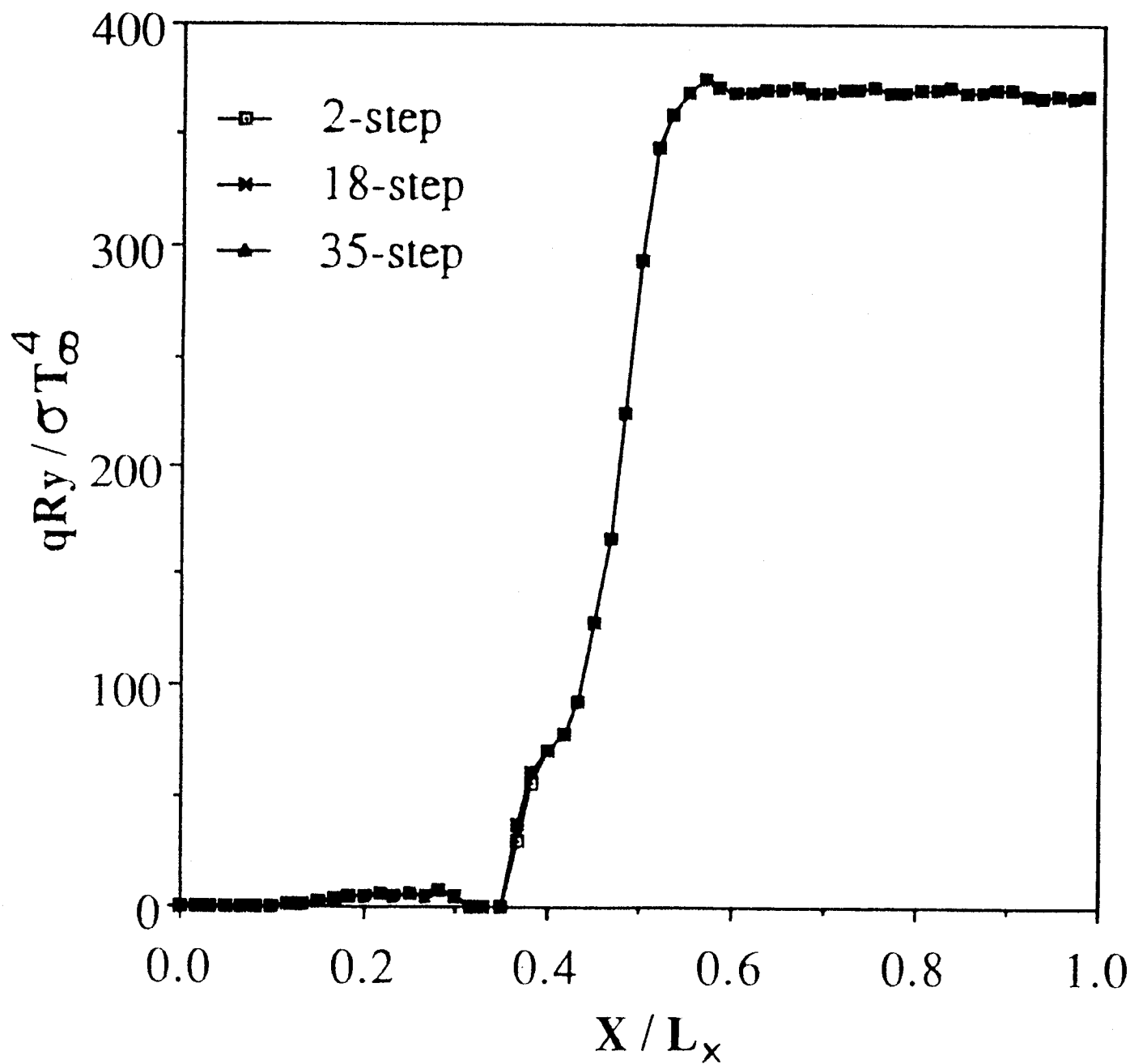


Fig. 5.9 Profiles of normal radiative flux

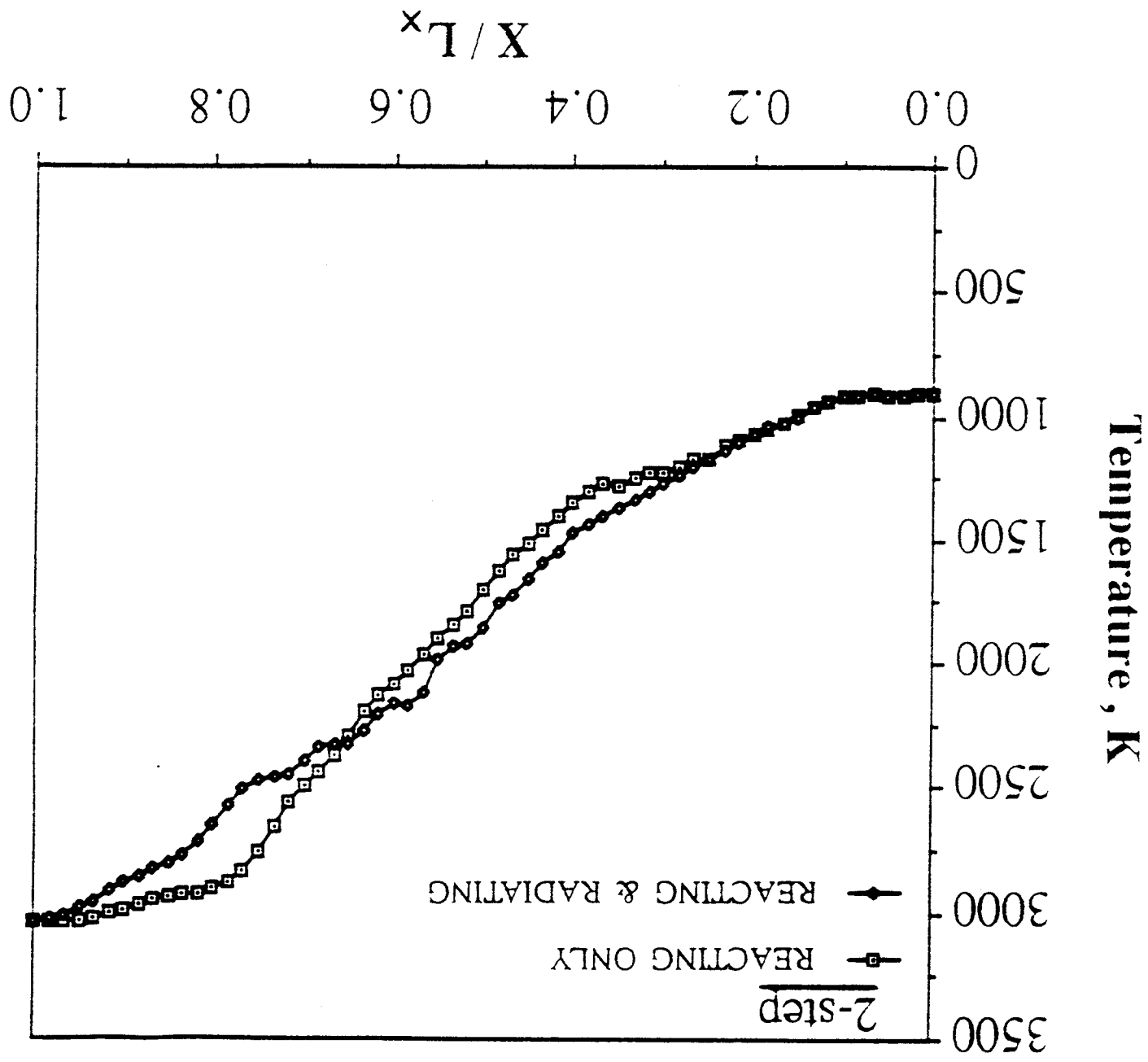


Fig. 5.10a Radiation effects on temperature profiles (2-step model)

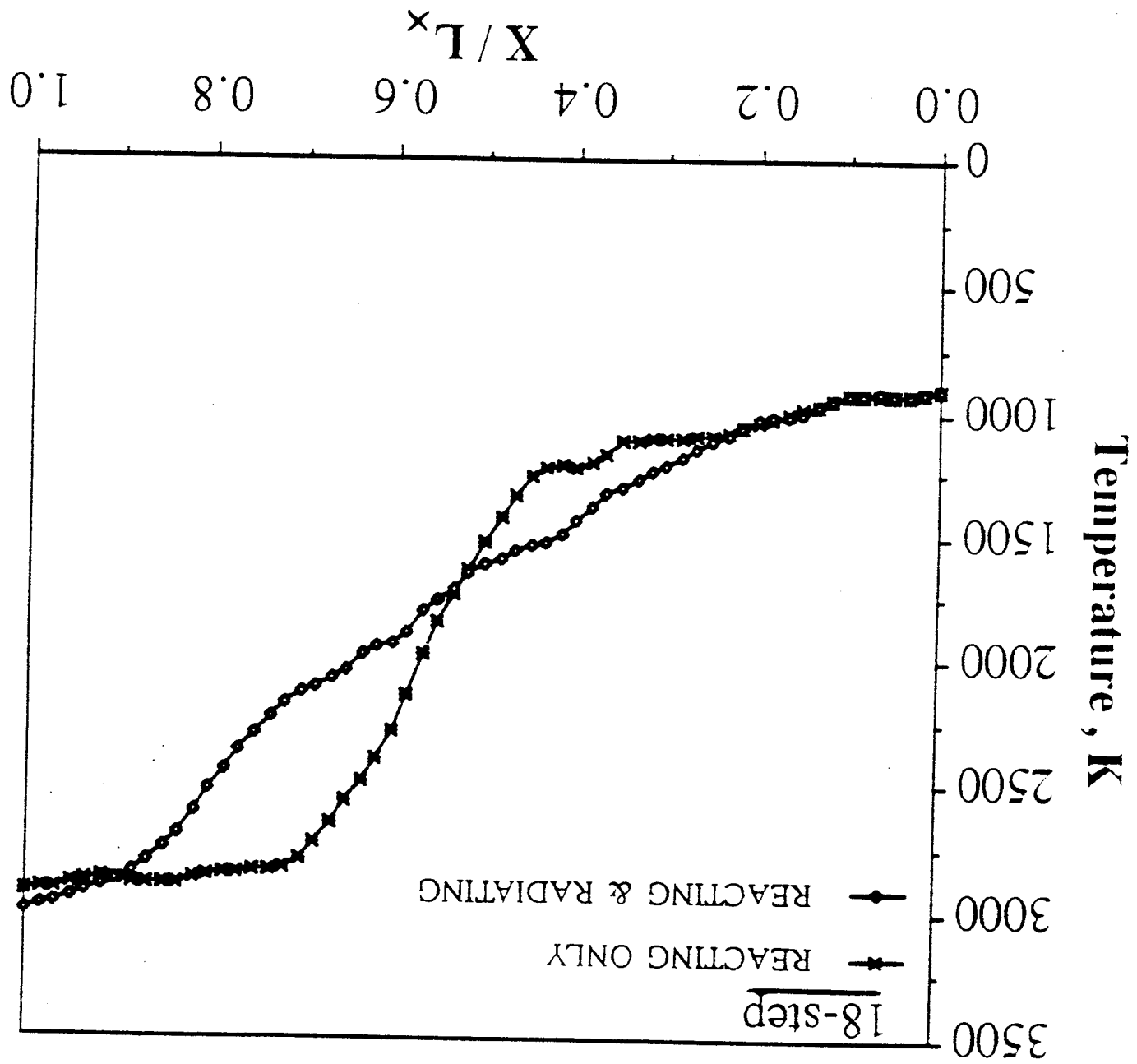


Fig. 5.10b Radiation effects on temperature profiles (18-step model)

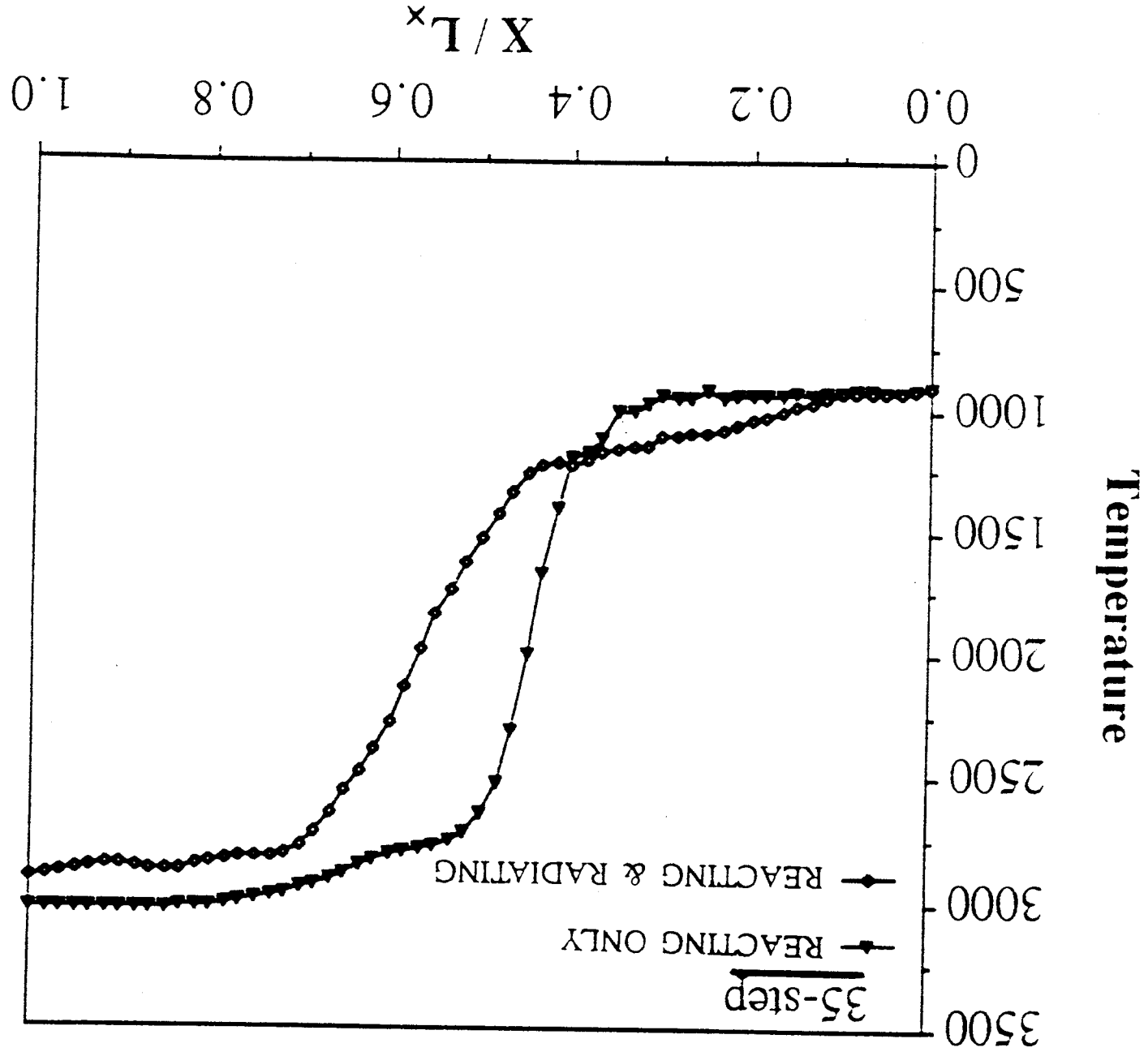


Fig. 5.10c Radiation effects on temperature profiles (35-step model)

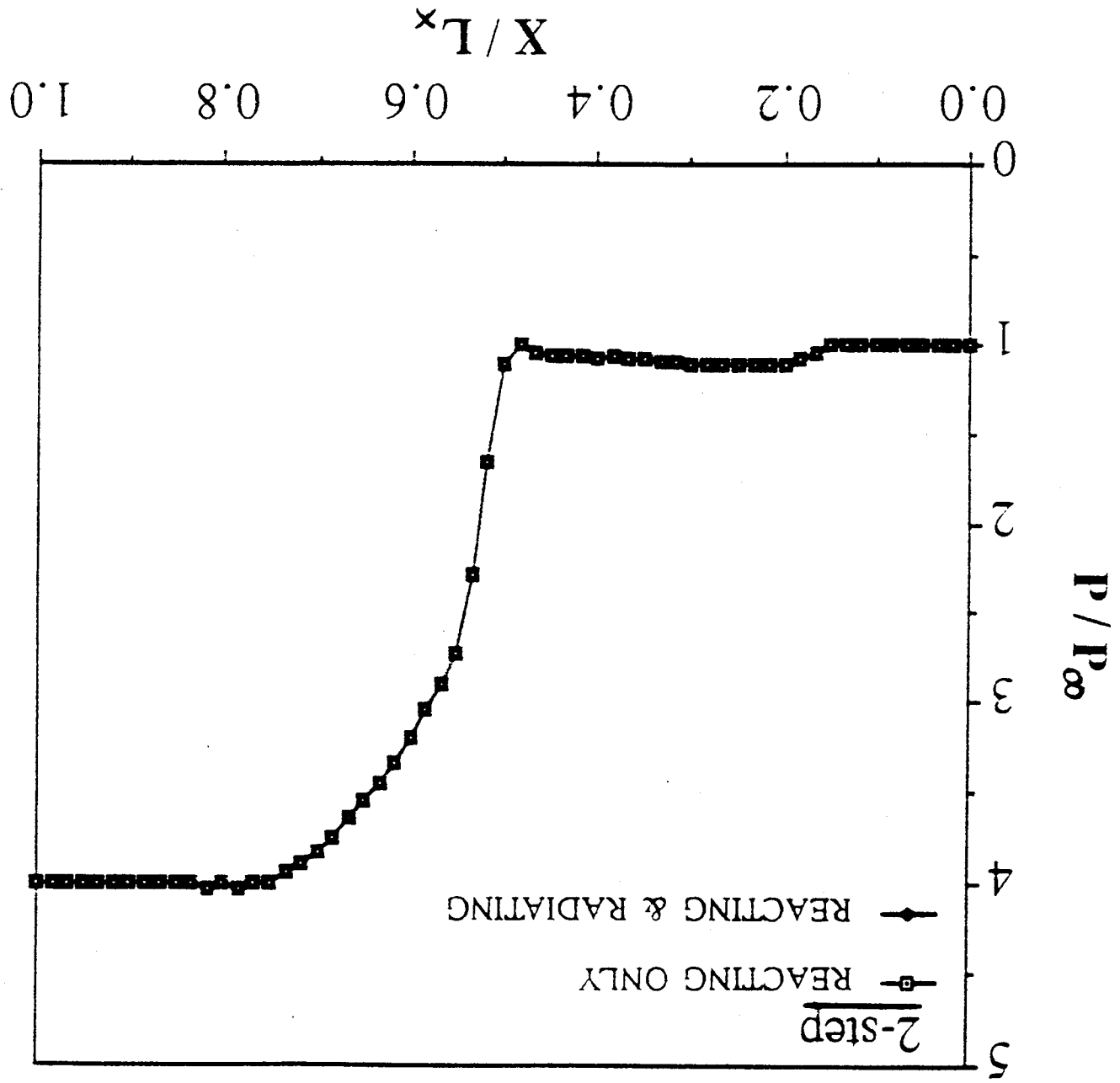


Fig. 5.11a Radiation effects on pressure profiles at $y = 0.13$ cm. (2-step model)

Fig. 5.11b Radiation effects on pressure profiles at $y = 0.13$ cm. (18-step model)

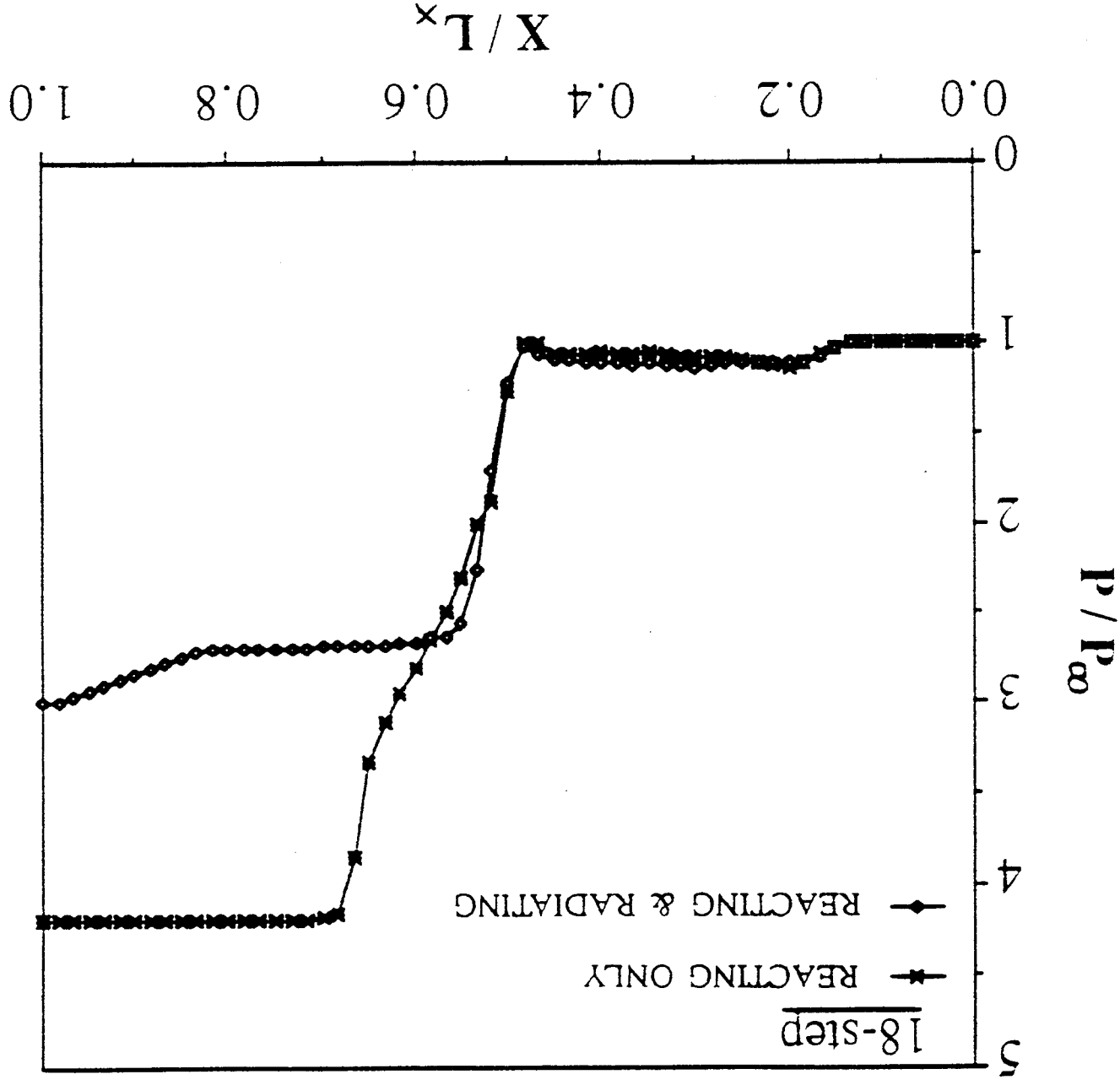
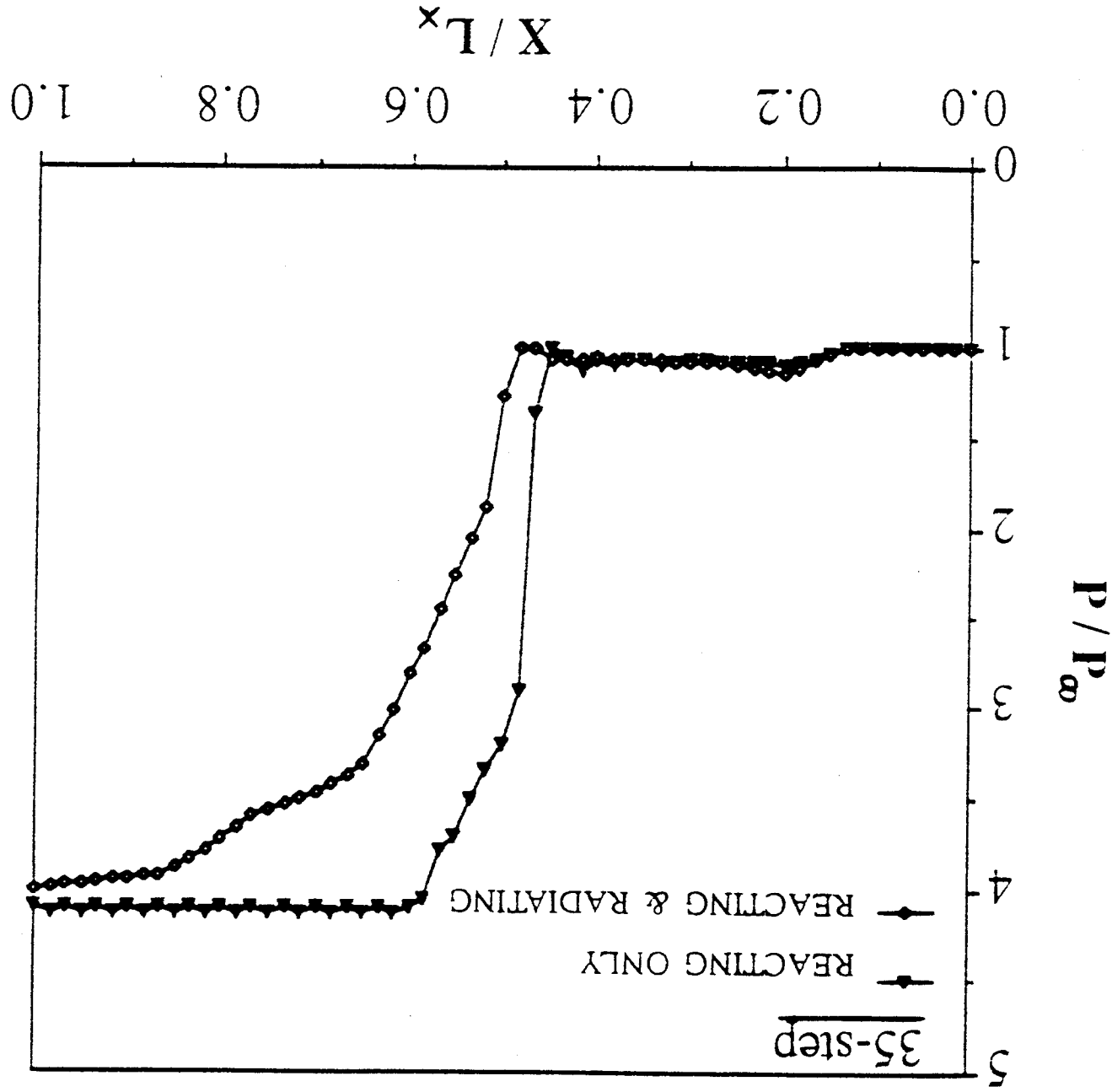


Fig. 5.11c Radiation effects on pressure profiles at $y = 0.13$ cm. (35-step model)



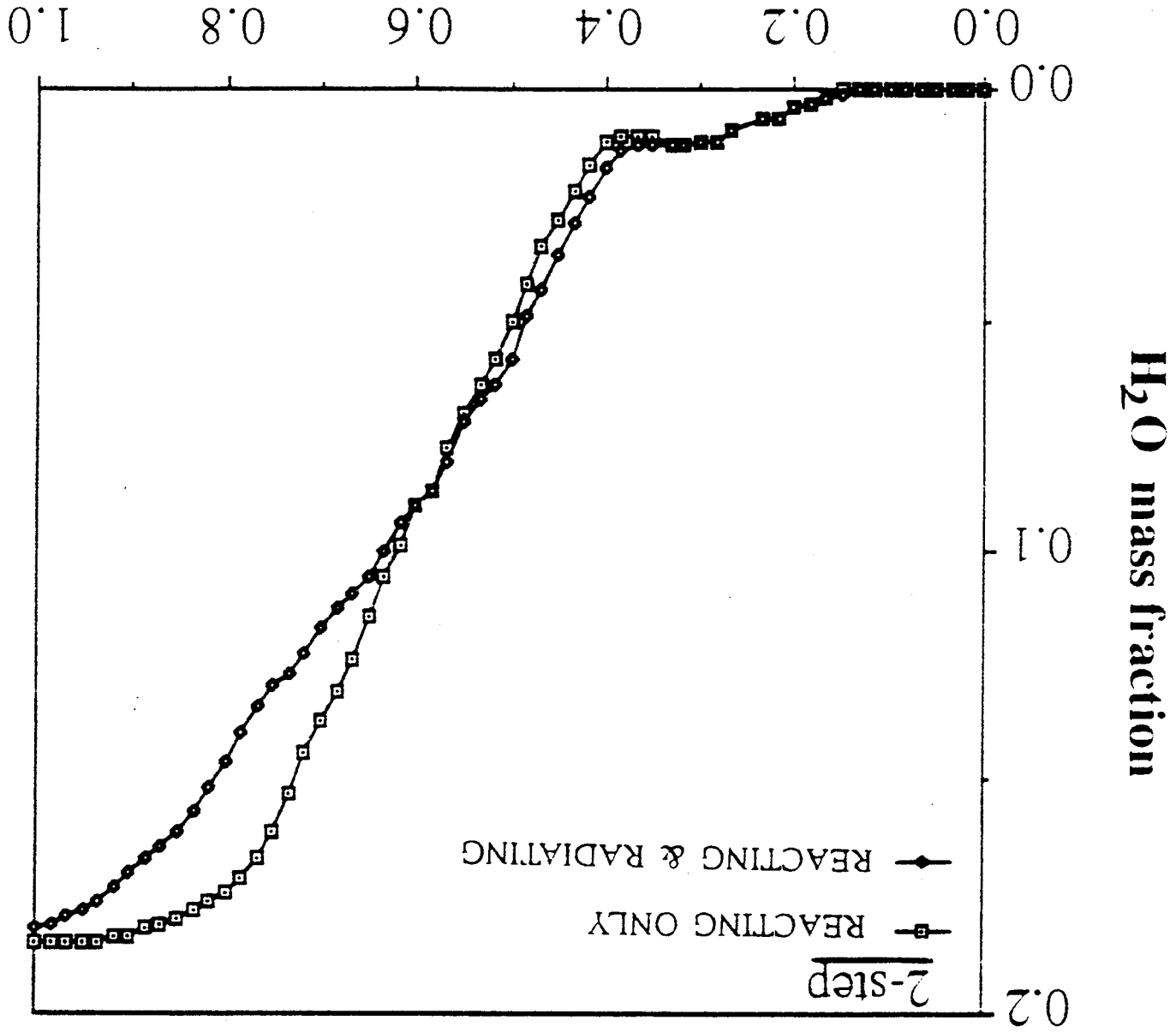


Fig. 5.12a Radiation effects on H₂O profiles (2-step model)

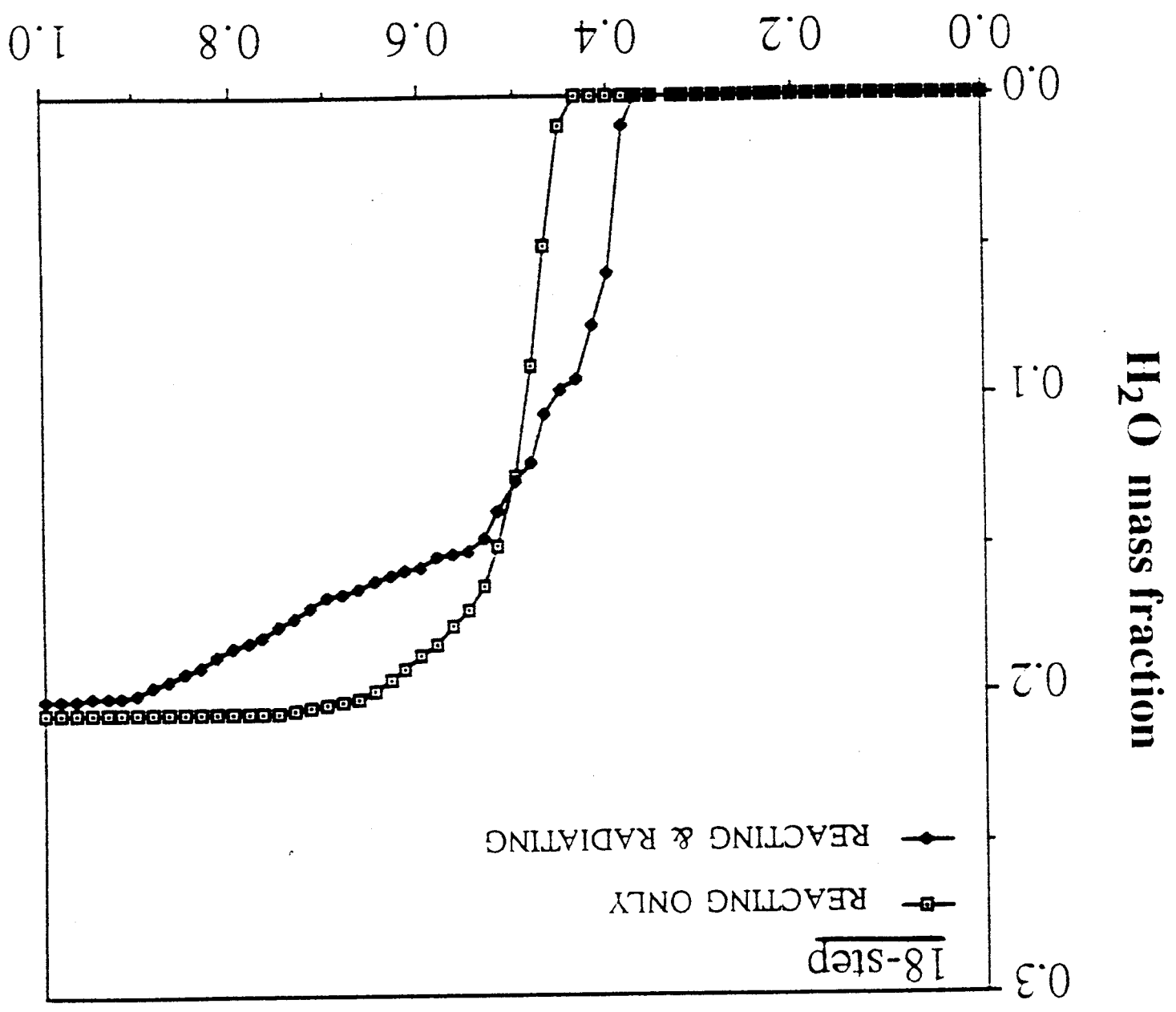


Fig. 5.12b Radiation effects on H_2O profiles (18-step model)

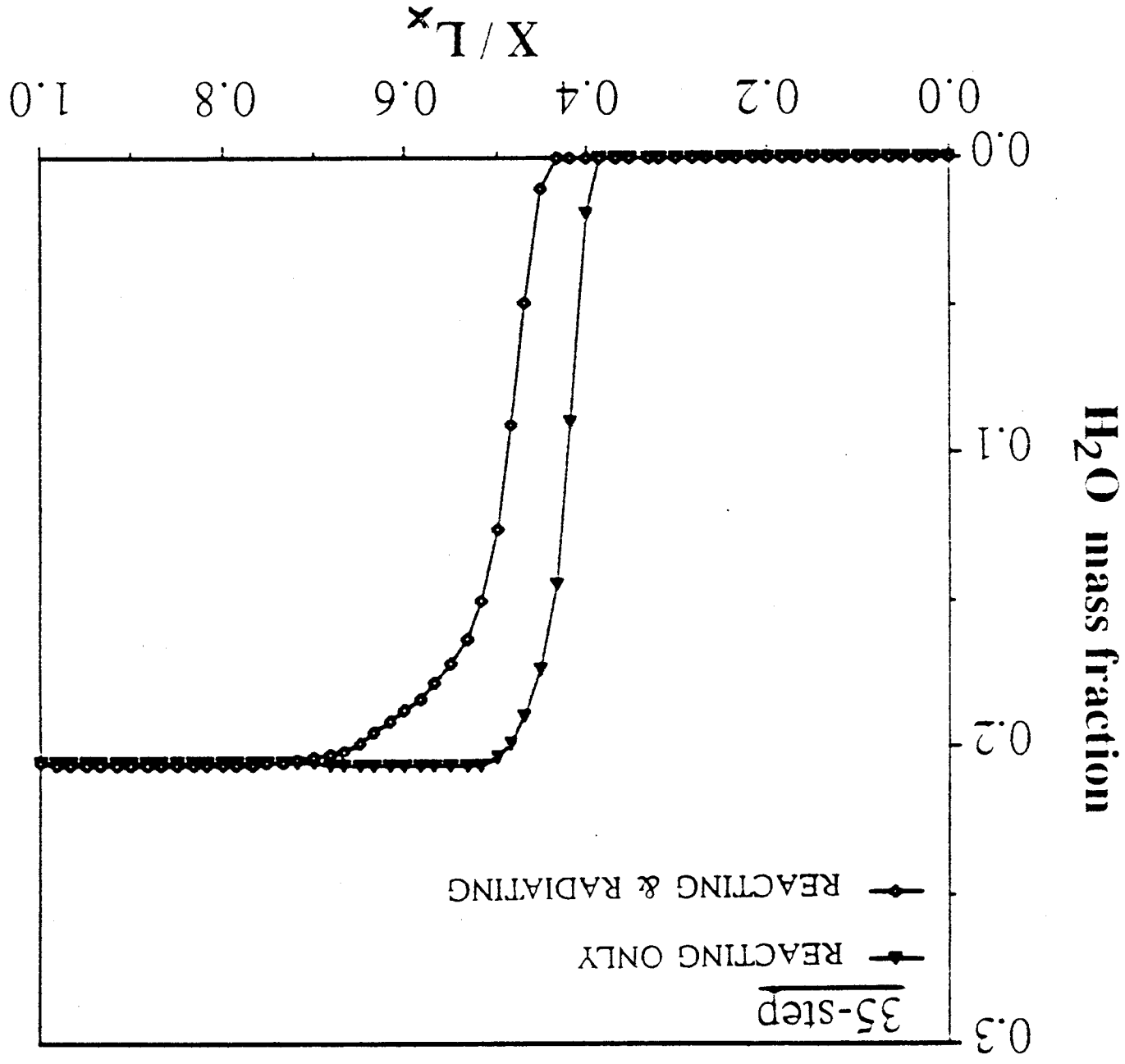


Fig. 5.12c Radiation effects on H₂O profiles (35-step model)

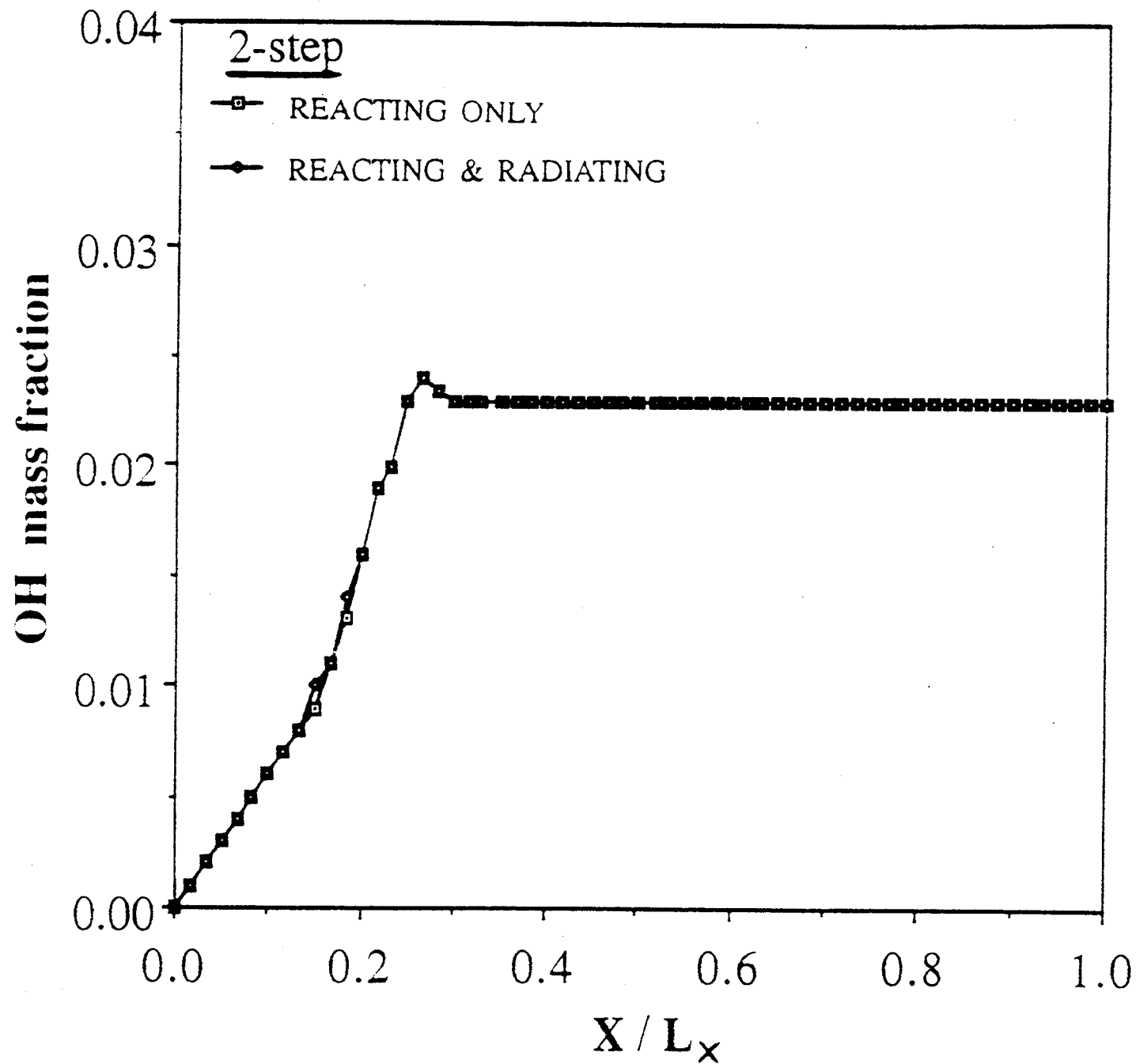


Fig. 5.13a Radiation effects on OH profiles (2-step model)

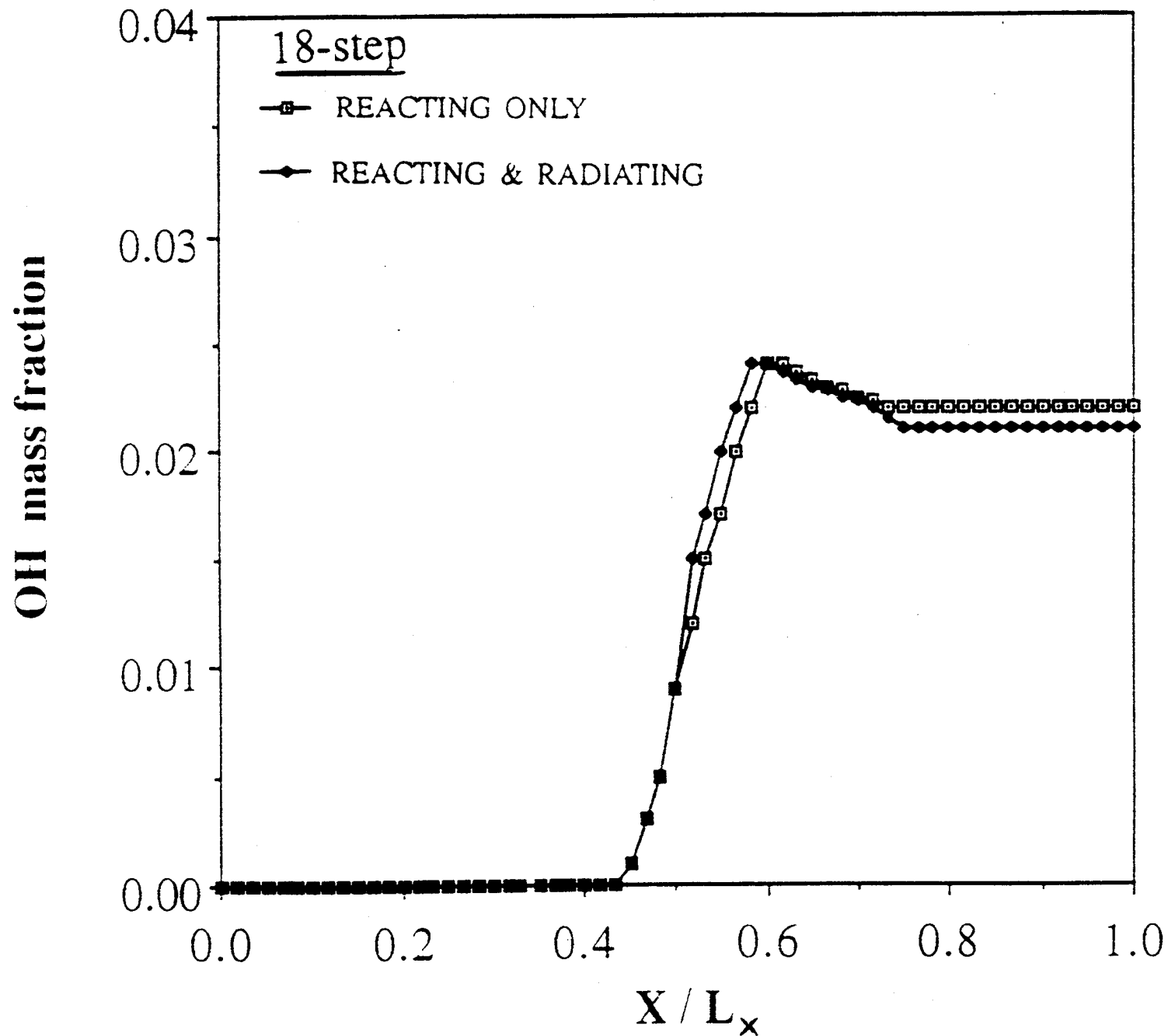


Fig. 5.13b Radiation effects on OH profiles (18-step model)

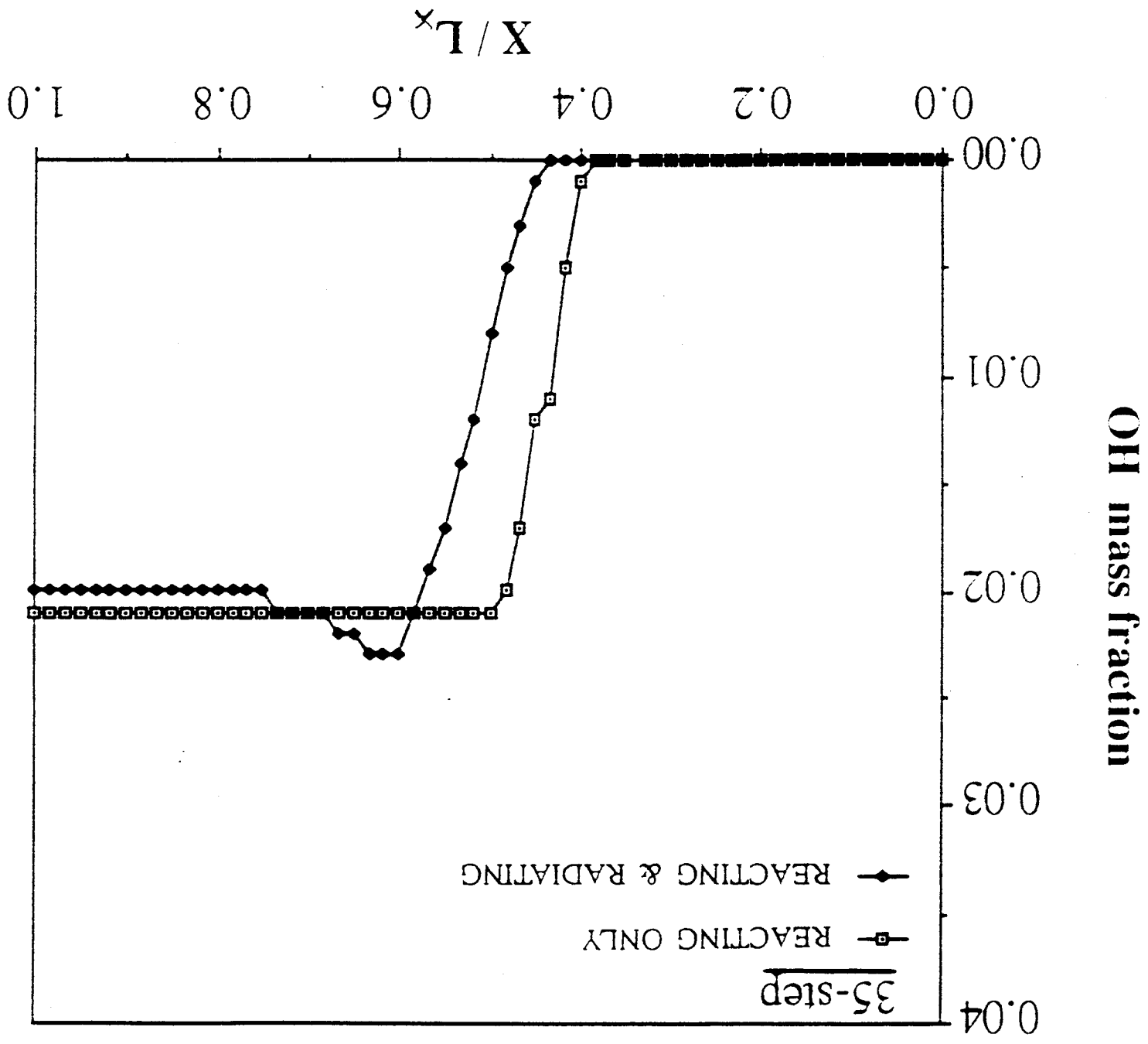


Fig. 5.13c Radiation effects on OH profiles (35-step model)

a slight effect of radiative interaction, as compared to the 18-step and 35-step models. The 18- and 35-step models, with radiative interaction, predict lower temperature and lower H_2O and OH concentrations after the shock. This is because of the q_{RX} flux which reduces the total energy. For reacting flows without radiation, it was seen earlier from Figs. 5.3 and 5.4 that the 18-step model had a longer ignition delay (ignition at $x/L_x = 0.43$), while the 35-step model had a shorter ignition delay (ignition at $x/L_x = 0.38$). Another effect of radiative interactions, seen in Fig. 5.12, is to nullify this difference in predictions of ignition delay. For both 18-step and 35-step models, with radiation, the shift in ignition is seen to occur by the same amount, $x/L_x = 0.05$. No such effect is seen on the ignition characteristics of the 2-step model. The results of Figs. 5.10–5.13 show the “cooling effect” of radiative interactions. The heat release from exothermic chemical reactions usually thickens the boundary layer, but the lower temperatures produced by the radiative interactions oppose this nonequilibrium effect. Since the ignition temperature is lowered, the ignition delay is also affected by the radiative heat transfer.

5.2 Thermochemical Nonequilibrium and Radiative Interactions

Studies were conducted to investigate the extent of radiative heat transfer in supersonic reacting flows undergoing vibrational relaxation. For the temperature range considered in this study, the important radiating species are OH and H_2O . The LTE (local thermodynamic equilibrium) radiative fluxes have been computed using the same formulation used in Sec. 5.1 of this chapter. The non-LTE radiative fluxes are calculated using a new approach discussed in Chap. 3. In order to avoid expensive computer usage, the chemistry model used in this study is a truncated 7-species, 7-step mechanism, derived from the first 7 reactions in Table 2.1. The five chemical species undergoing

vibrational relaxation are H_2 , O_2 , H_2O , OH and N_2 . The monatomic species H and O do not subscribe to the “dumbbell” theory of harmonic oscillators, and so are in equilibrium.

In order to validate the theoretical formulations discussed in Chap. 3, comparisons were made with results from a hypersonic workshop [53]. The physical model for this study is shown in Fig. 3.1. Even though the present study is for H_2 — air chemistry, and the results presented in [53] are for N_2 — O_2 reactions, this was the best comparison available. Figure 5.14 shows the one-dimensional results for translational and vibrational temperature obtained for air chemistry in an expanding nozzle. A total of 101 grid points were used in the flow direction. It can be seen from Fig. 5.14 that the thermochemical nonequilibrium model used in the present study, compares quite favorably with the one used in [53]. The slight discrepancy in prediction of vibrational temperature T_v is due to differences in the method of computing the relaxation time. In the present work, the relaxation time is calculated using a relation given by Millikan [63], whereas the method used in [53] is based on a relation given by Vincenti and Kruger [24].

The physical model used for the remaining part of this study is the nozzle and is shown in Fig. 3.2. The first step was to assume chemical nonequilibrium (CNE) in all cases. Figure 5.15 shows the one-dimensional results, using 101 grid points, for the temperature and pressure variations along x . The temperatures exhibit relaxation along the nozzle (Fig. 5.15a). The vibrational temperature T_v is shown for the species (H_2O) that exhibits strongest nonequilibrium effect, and it deviates significantly from the translational-rotational temperature T . This shows that thermochemical nonequilibrium (TCNE) is still present in the nozzle, and reduces the translational temperature. The pressure profiles (Fig. 5.15b) do not show any effect of thermal nonequilibrium.

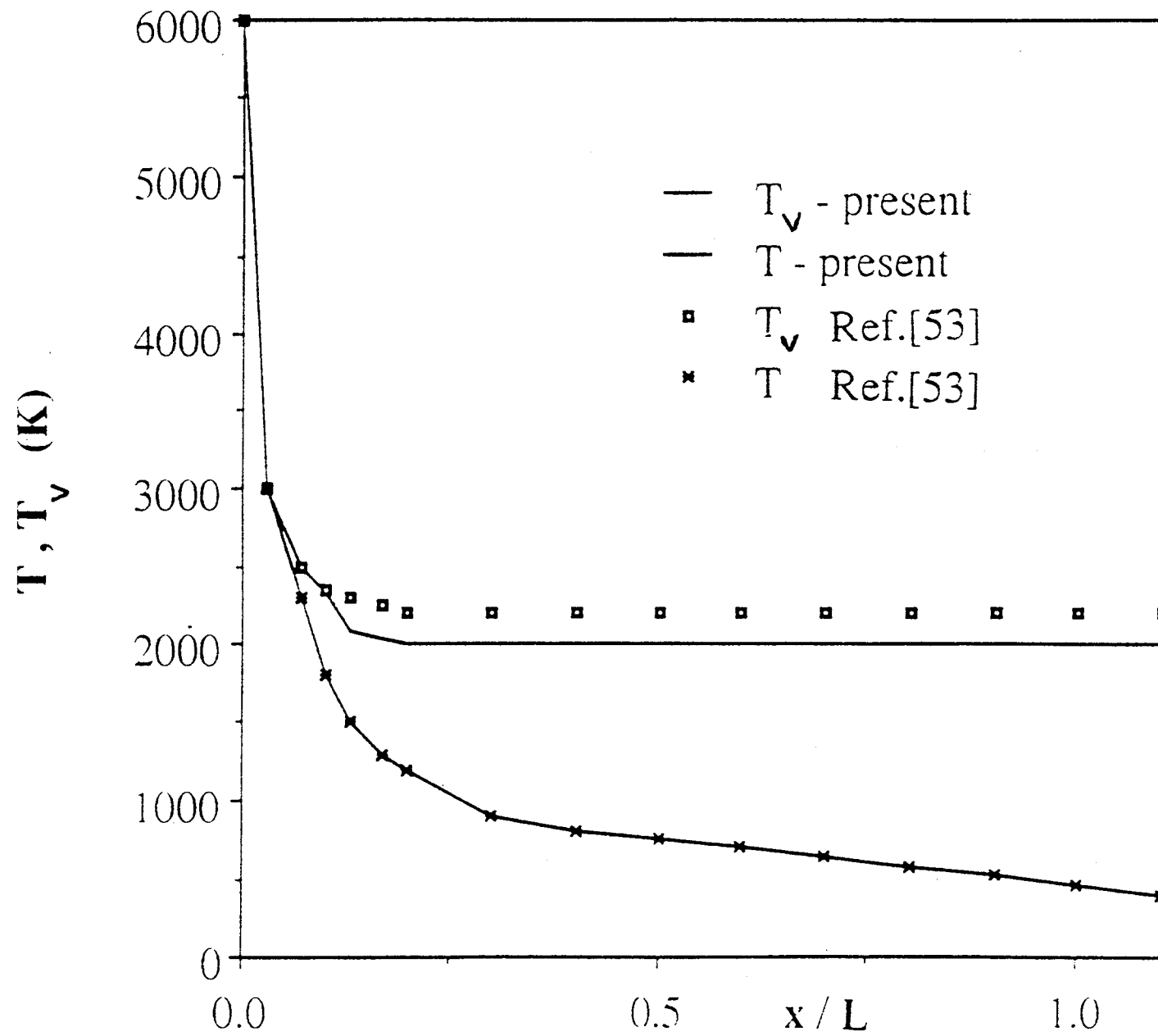


Fig. 5.14 Air chemistry temperature profiles (1-D)

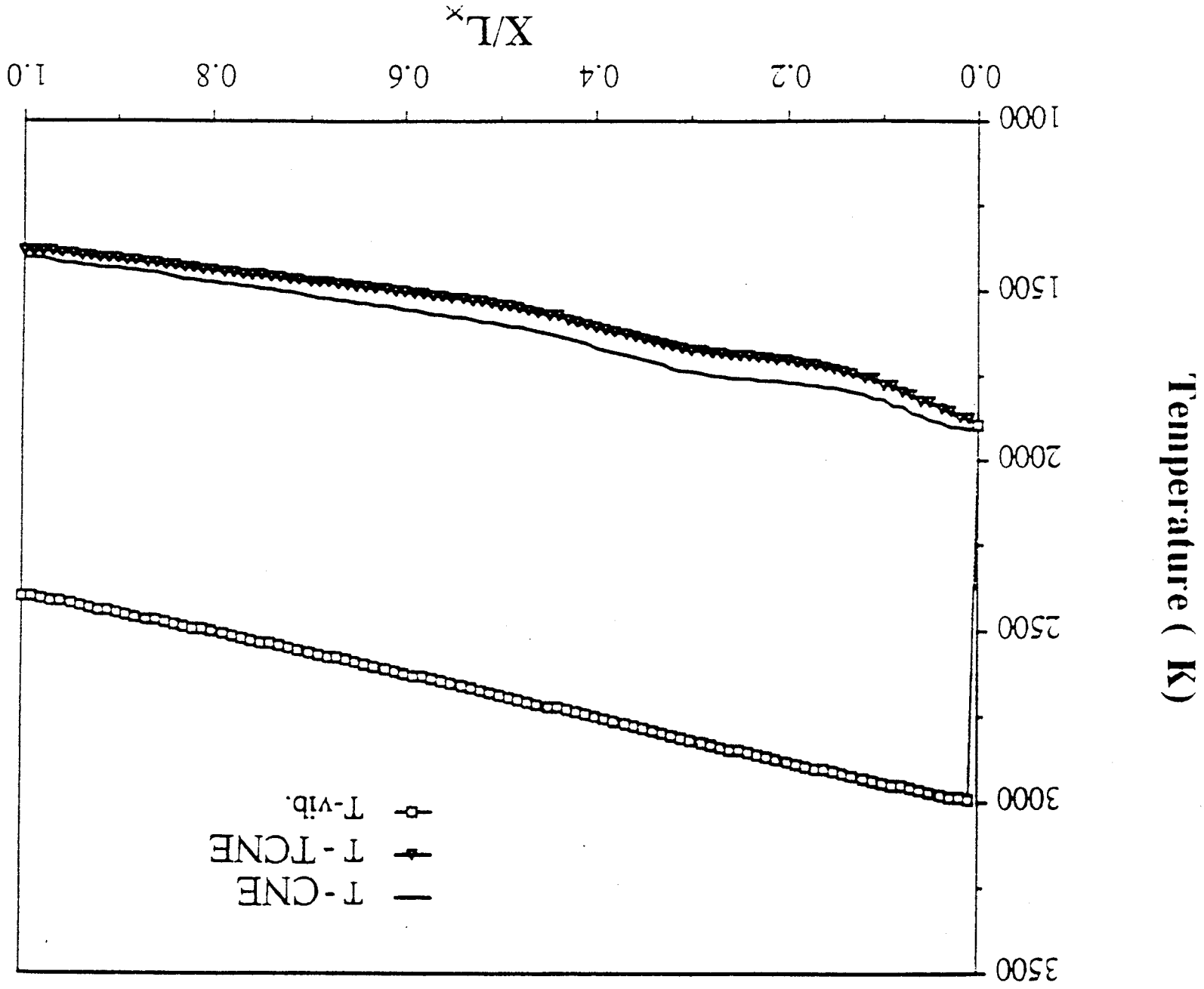


Fig. 5.15a Temperature profiles (1-D)

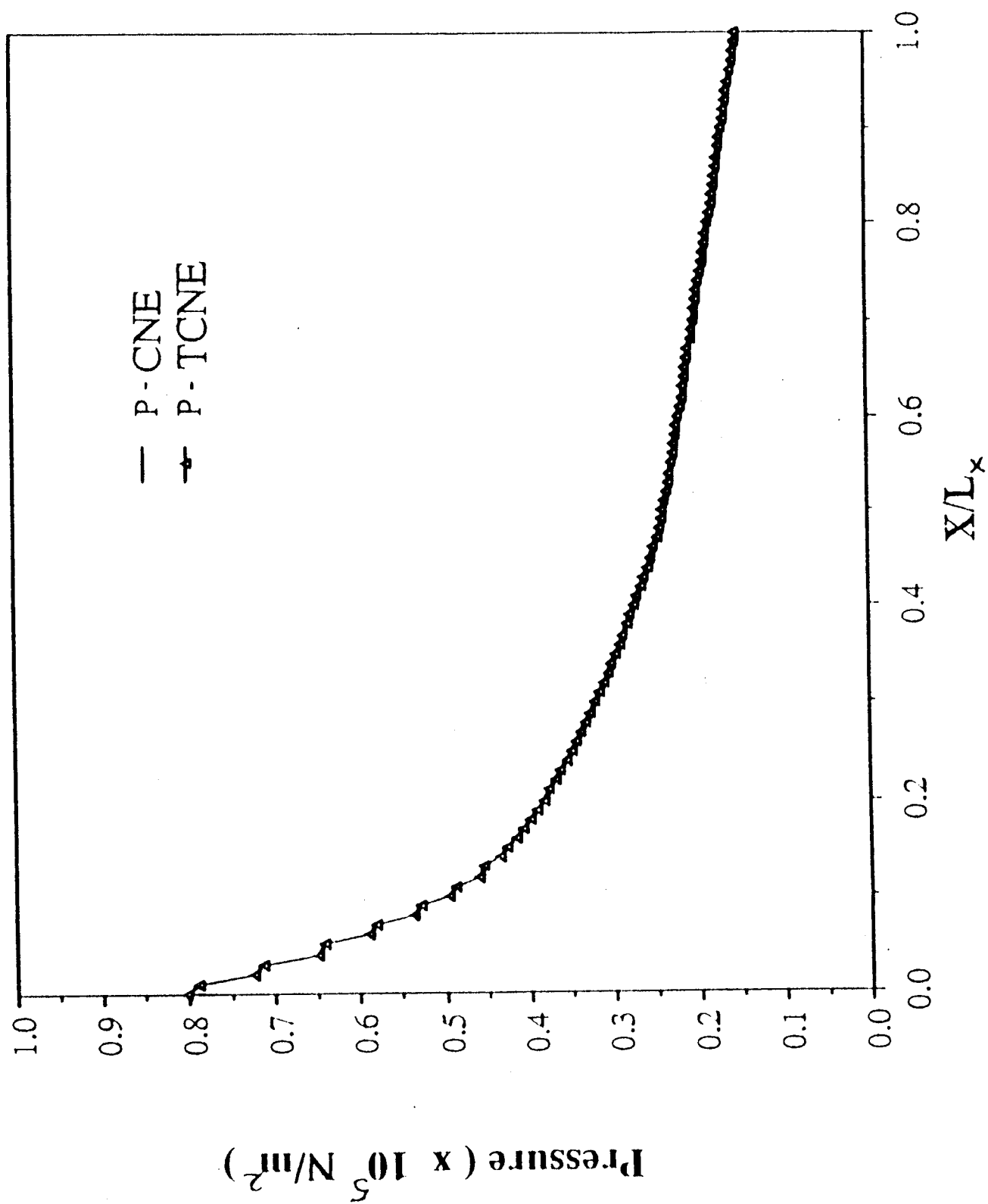


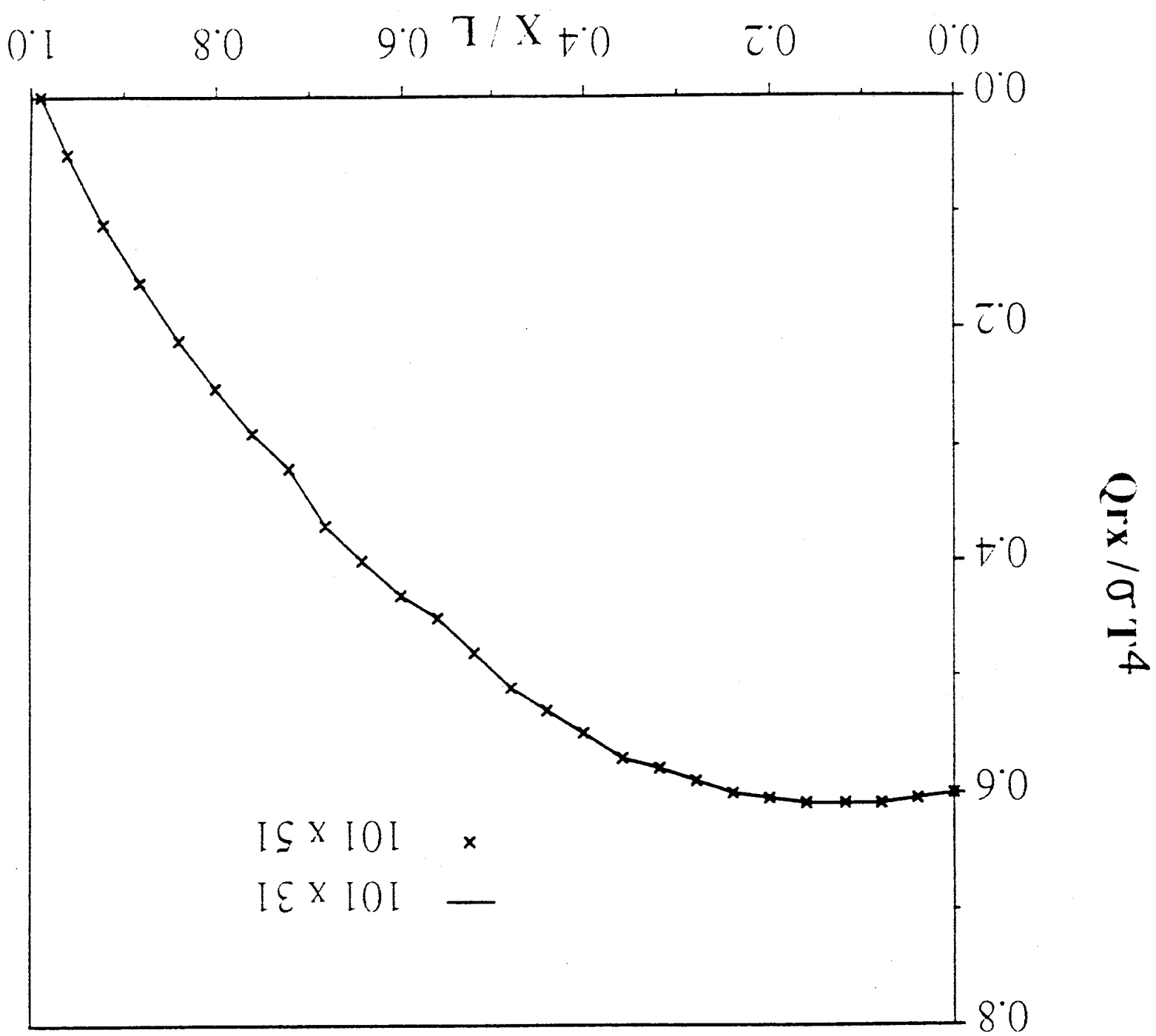
Fig. 5.15b Pressure profiles (1-D)

Based on the above understanding of thermochemical nonequilibrium in supersonic hydrogen-air flames, the radiative interactions were examined for a two-dimensional flow. A 101×31 grid was used for this part of the study. Only the upper half of the flow was computed, since the nozzle is symmetric about the centerline. The results were plotted after every four grid points. Three y locations were considered, viz. $j = 1$, $j = j_{mid}$, and $j = j_{max}-1$, corresponding to the centerline, midway between centerline and wall, and wall boundary layer, respectively. The local thermodynamic equilibrium (LTE) and non-LTE results were obtained by using a value of $\eta = \eta_c/\eta_r = 0.0$ and 5.0 respectively, for the nonequilibrium parameter in Eq. (3.13).

Figure 5.16a shows profiles of streamwise radiative flux using 101×31 and 101×51 grids, for the purpose of a grid resolution study. It appears that the 101×31 grid used in the present study is sufficient. Figure 5.16b shows the profiles of the normalized streamwise radiative flux q_{Rx} along two y locations. It should be noted that the radiative flux at the centerline $j = 1$, is negligible, and hence is not plotted. It can be seen that the q_{Rx} flux in the wall boundary layer $j = j_{max}-1$, (Fig. 5.16c) is higher than at the other two locations. This is due to the adiabatic wall boundary condition, which precludes any heat transfer to or from the wall. An important effect of thermal nonequilibrium is to reduce the radiative interactions. The q_{Rx} decreases towards the nozzle exit due to cancellation of fluxes in the positive and negative directions.

Figure 5.17 shows the variations of the normal radiative flux q_{Ry} along x , at two y locations. Here also, the radiative flux at the centerline $j = 1$, is zero (because of the symmetry boundary condition) and is not plotted. It can be seen that the q_{Ry} flux increases only slightly in the positive y direction, reaching a maximum in the wall boundary layer (Fig. 5.17b). This is because of the optically thin assumption, which means that there is negligible loss of radiative flux from the wall to neighboring gas molecules. Also, thermal

Fig. 5.16a: Grid resolution study on streamwise radiative flux — at wall ($j = j_{\max} - 1$)



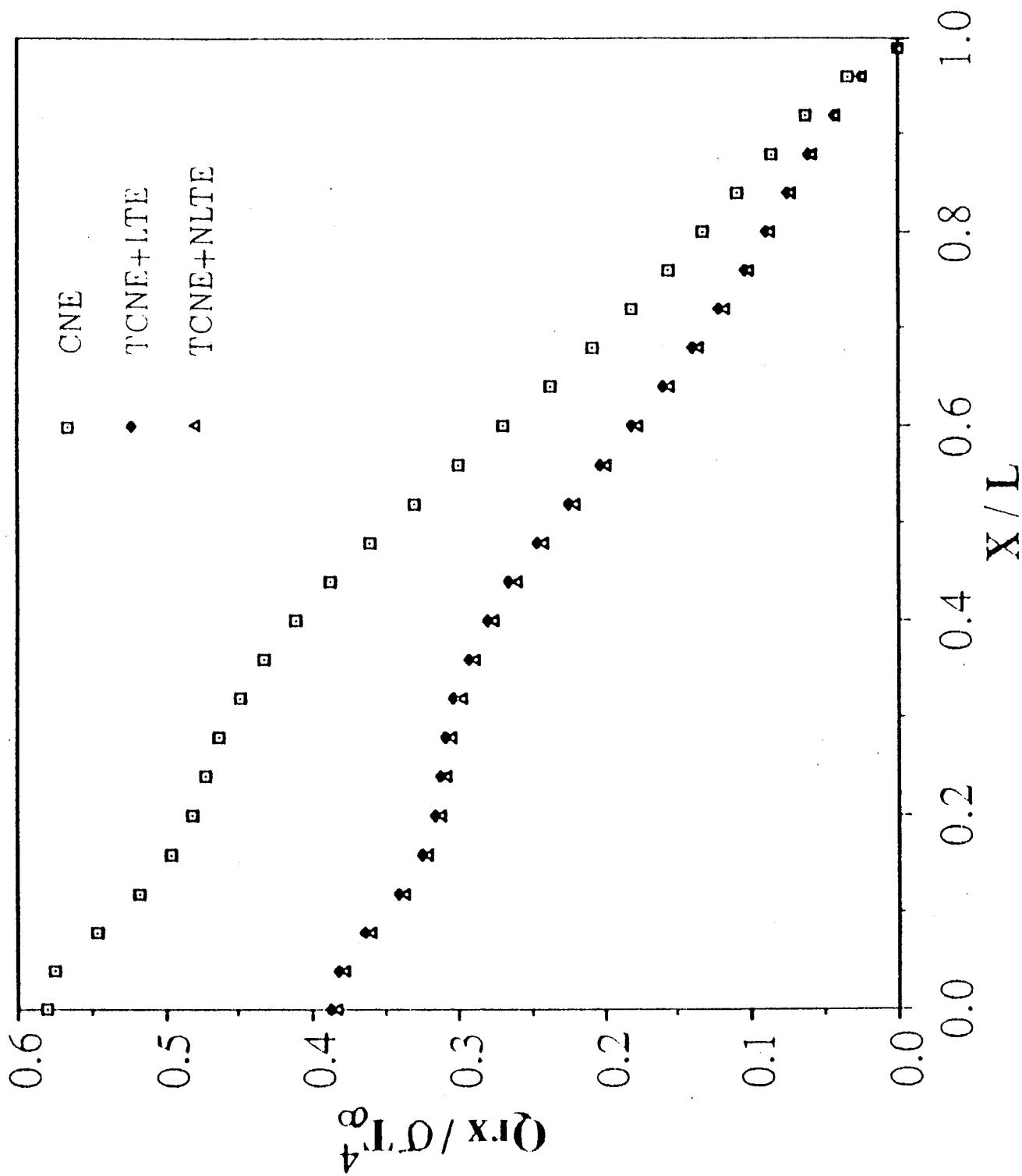


Fig. 5.16b Streamwise radiative flux profiles — midway ($j = j_{mid}$)

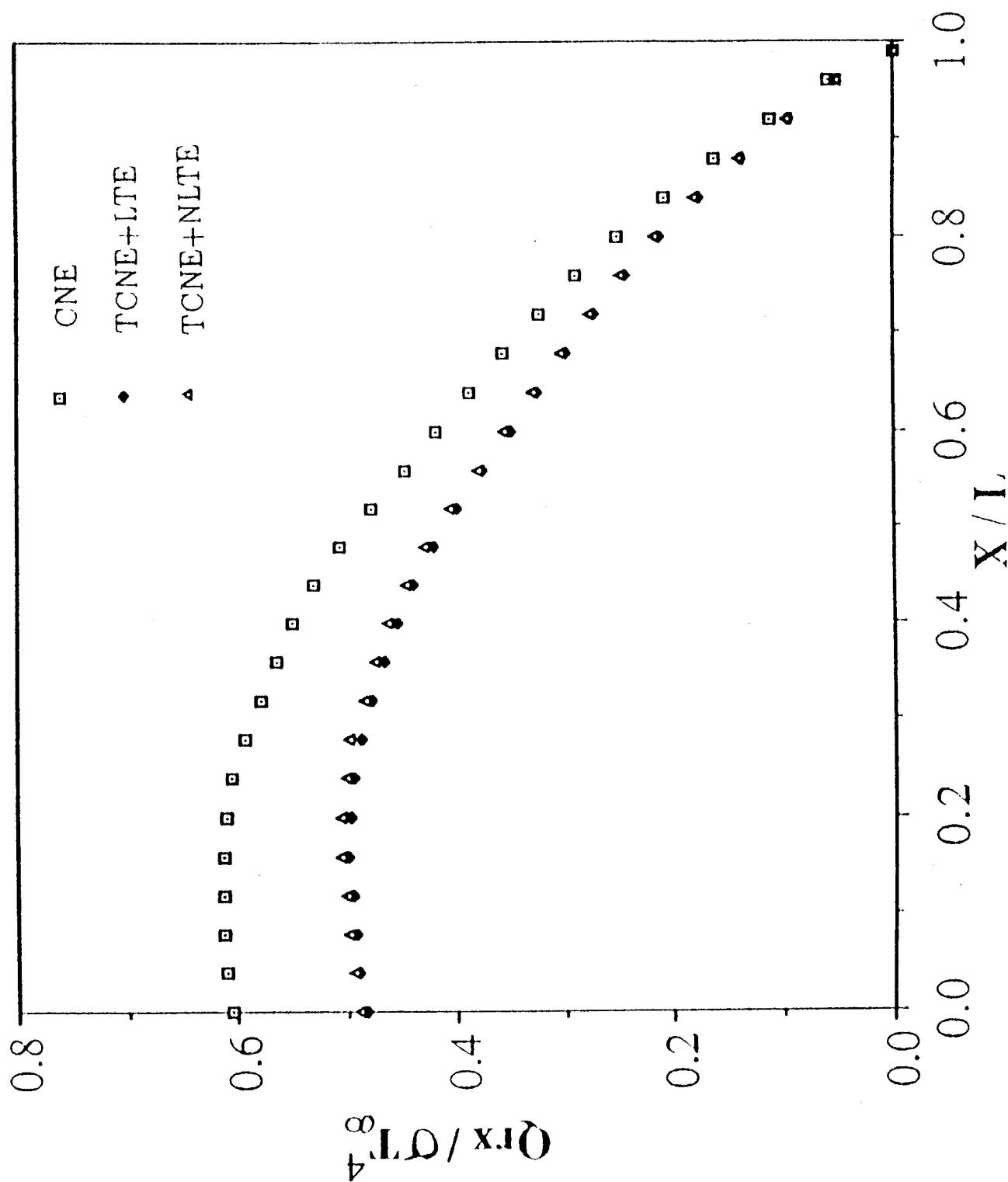


Fig. 5.16c Streamwise radiative flux profiles — wall ($\bar{u} = j_{\max} - 1$)

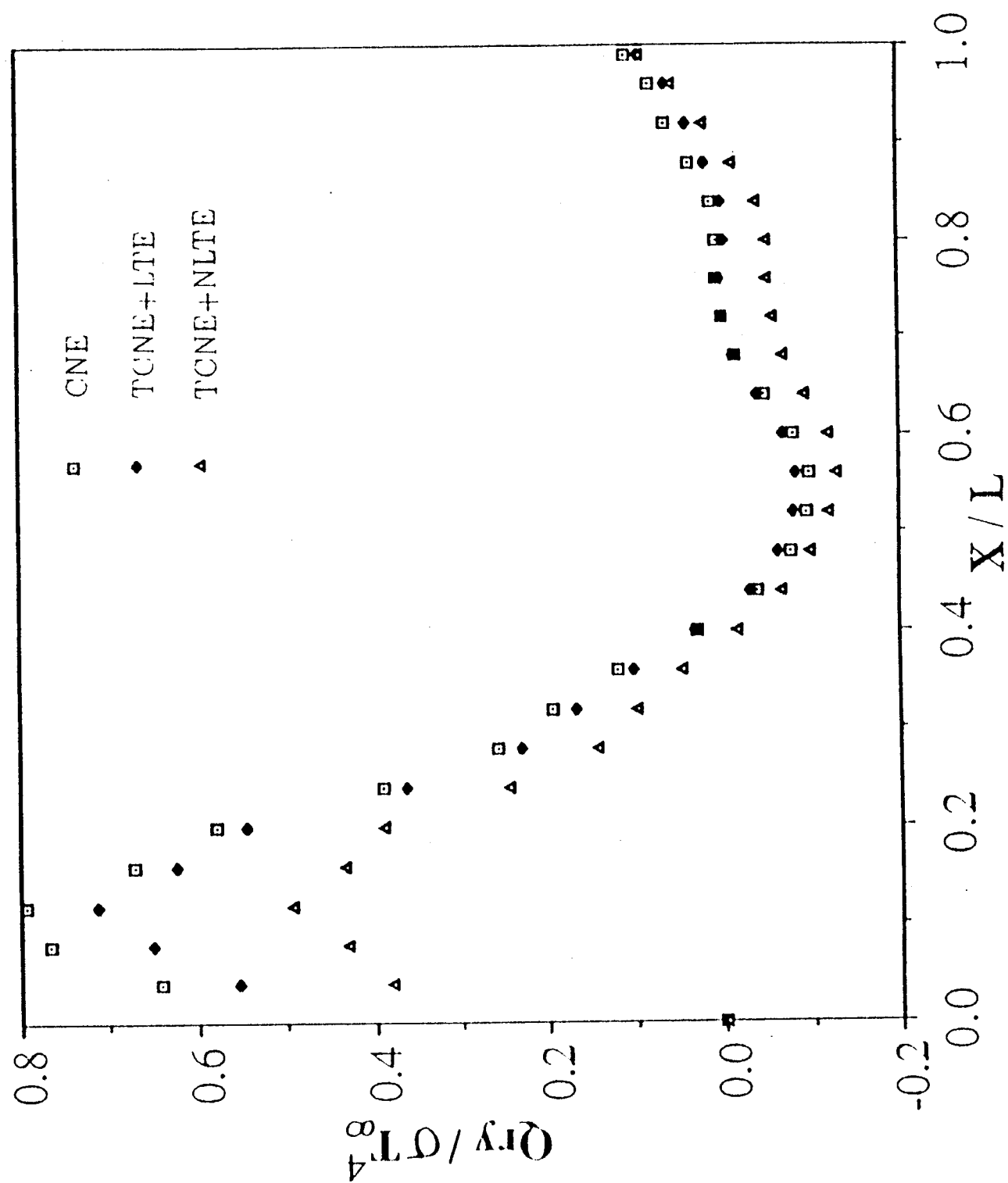


Fig. 5.17a Normal radiative flux profiles ($j = j_{\text{mid}}$)

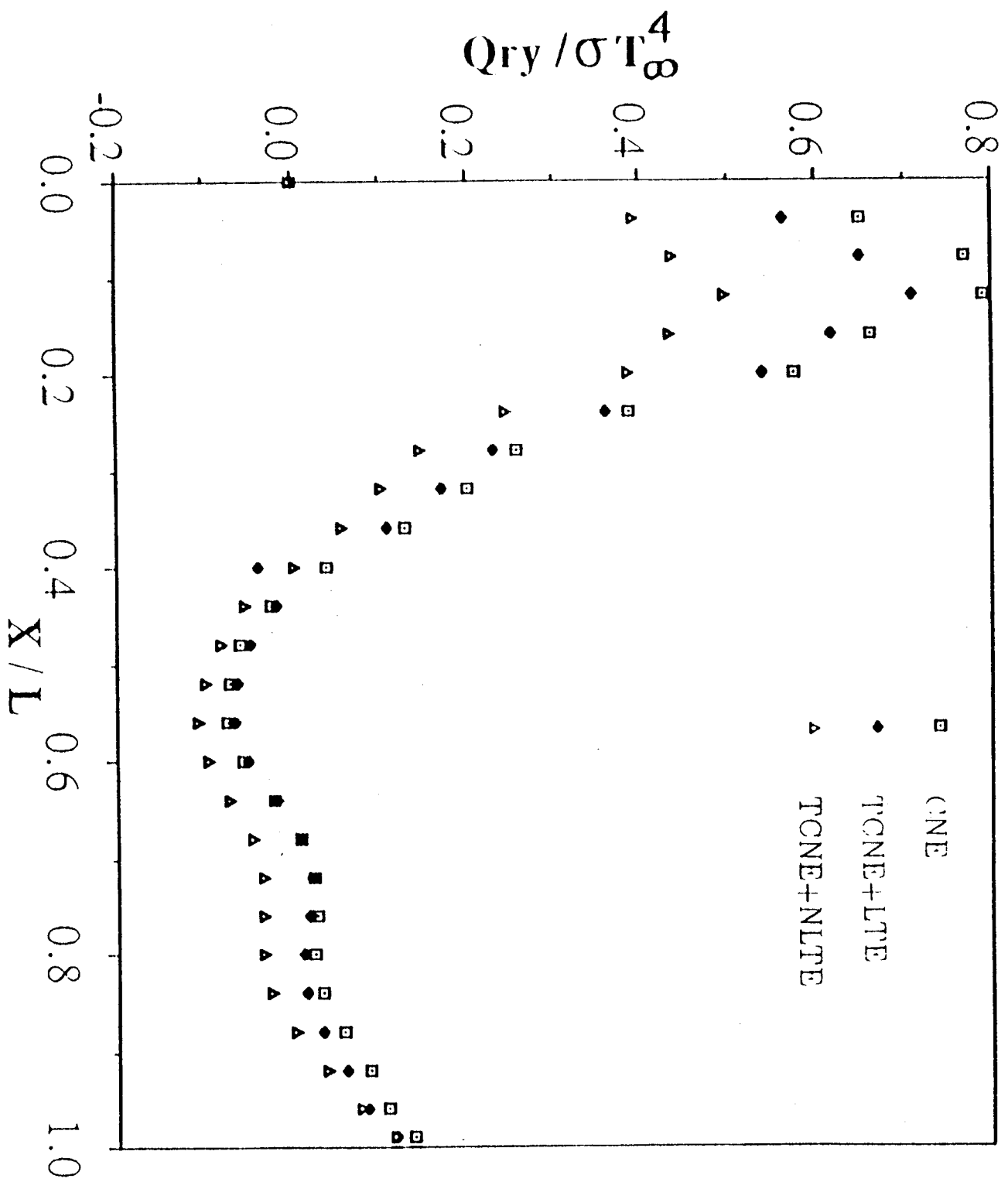


Fig. 5.17b Normal radiative flux profiles ($j = j_{\max} - 1$)

nonequilibrium reduces the radiative interactions. The q_{Ry} profiles exhibit another peak near the nozzle inlet, because of sudden increase in radiating species due to chemical reactions.

Figure 5.18 shows the temperature profiles along the three y locations. It can be seen that vibrational nonequilibrium reduces the translational-rotational temperature. The radiative interactions serve to negate this thermal nonequilibrium effect (especially in the wall boundary layer, Fig. 5.18c). The oscillations in the temperature profiles (Figs. 5.18a and 5.18b), occur only in the presence of radiative interactions. These oscillations are due to assumption of optically thin radiation, wherein there is a negligible loss of q_R to the wall from the gas molecules. It is interesting to see that this numerical disturbance is absent at the wall (Fig. 5.18c). It can be seen that the temperature at the midway ($j = j_{mid}$) location is higher than at the other two locations. This is because of the heat release due to chemical reaction. The temperature in the wall boundary layer ($j = j_{max}-1$) as seen in Fig. 5.18c is lower than the centerline temperature. This is because of the adiabatic wall boundary condition, which prevents heat transfer outside the wall. Consequently, the wall temperature rises towards the nozzle exit.

Figure 5.19 shows pressure profiles along the x direction. The pressure oscillations (Figs. 5.19a and 5.19b) occur only in the presence of radiative interactions. This is because of the optically thin assumption, which means that there is negligible loss of radiative flux from the wall to neighboring gas molecules. A reduction of pressure due to vibrational nonequilibrium can be seen. A trend similar to the temperature profiles (Fig. 5.18) is observed. This is analogous to the thickening of the boundary layer on a flat plate (i.e. lowering of the pressure) in the presence of thermal nonequilibrium.

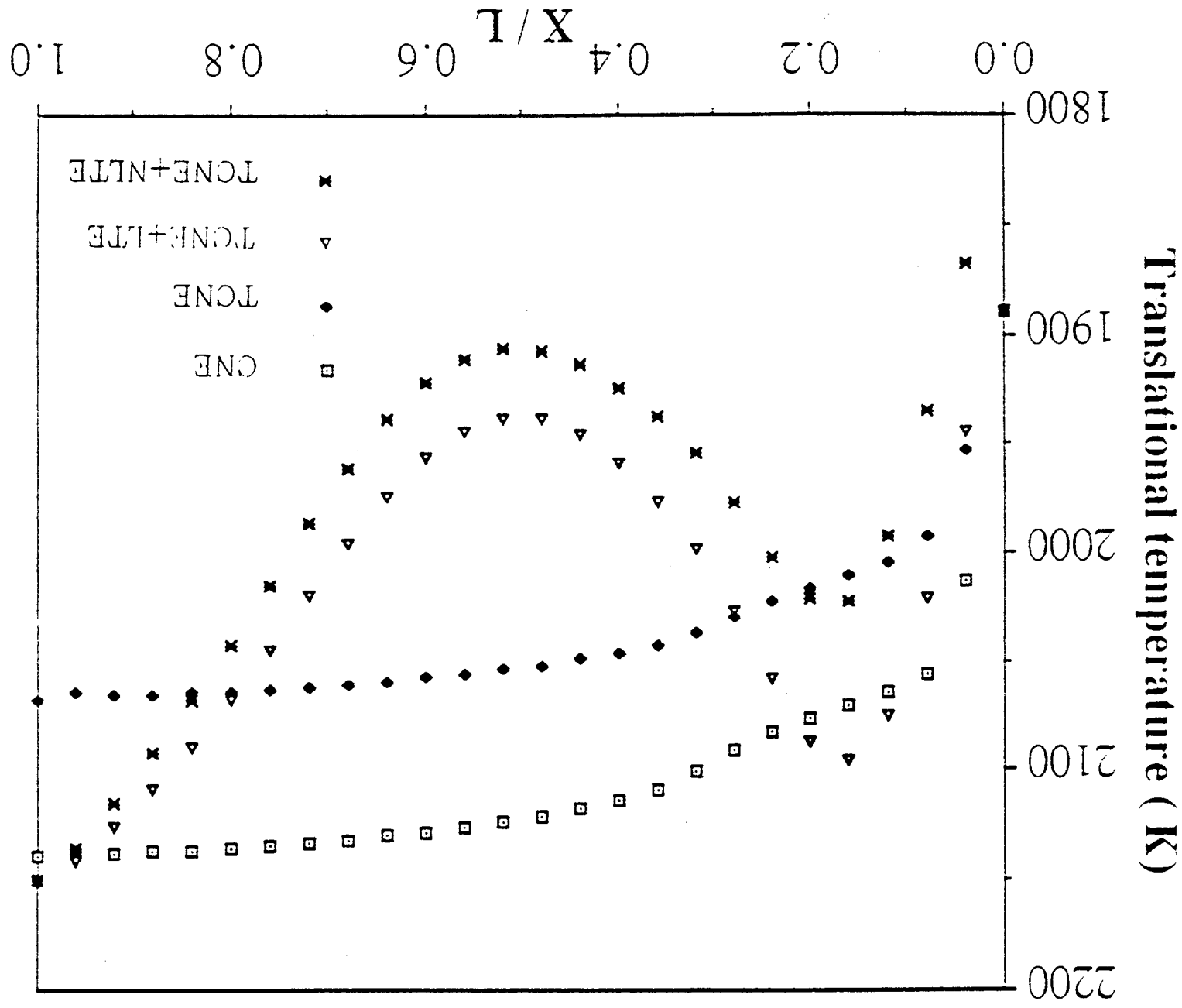
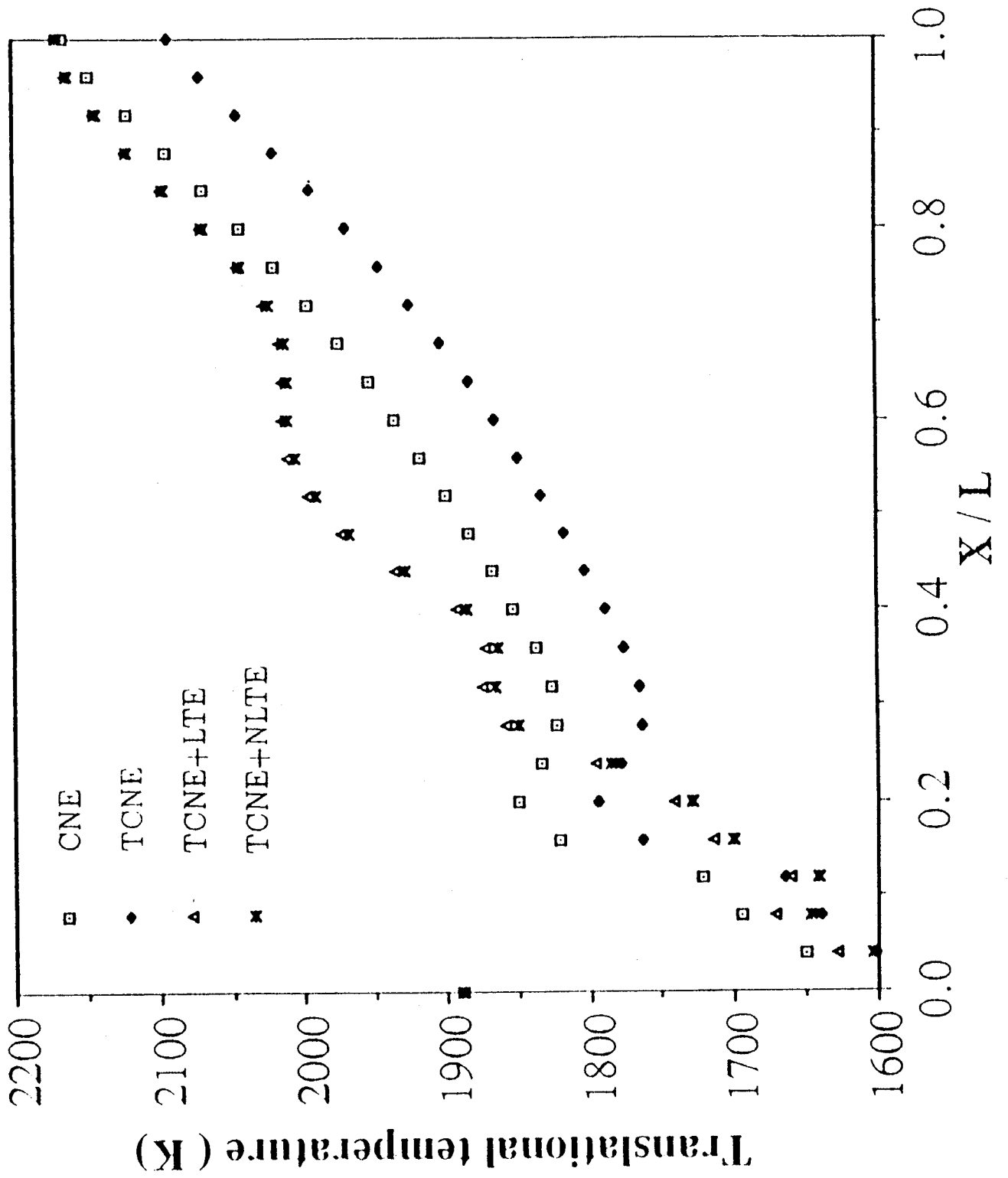


Fig. 5.18a Translational temperatures ($g = 1$)

Fig. 5.18c Translational temperatures ($j = j_{\max} - 1$)

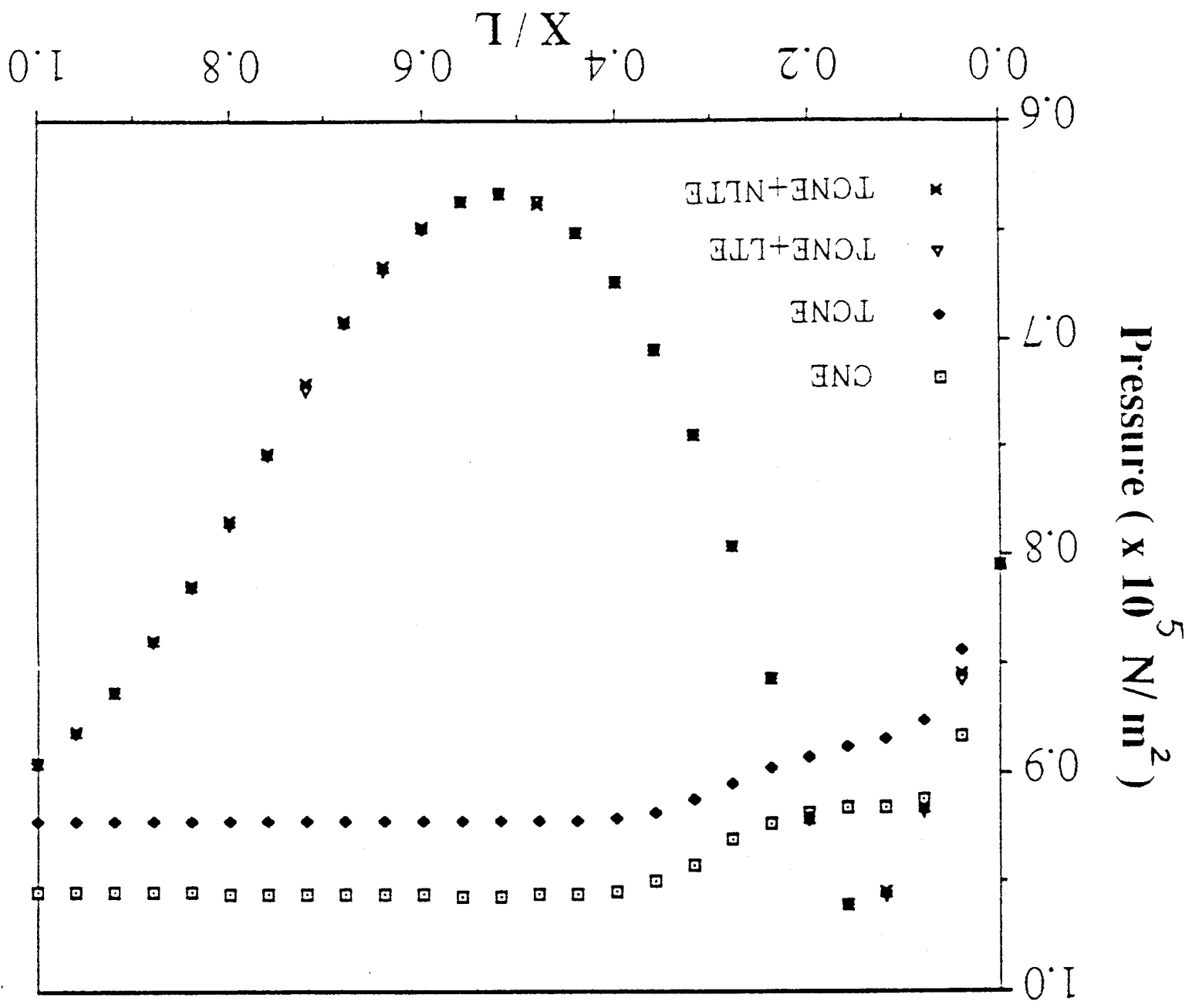


Fig. 5.19a Pressure profiles ($\eta = 1$)

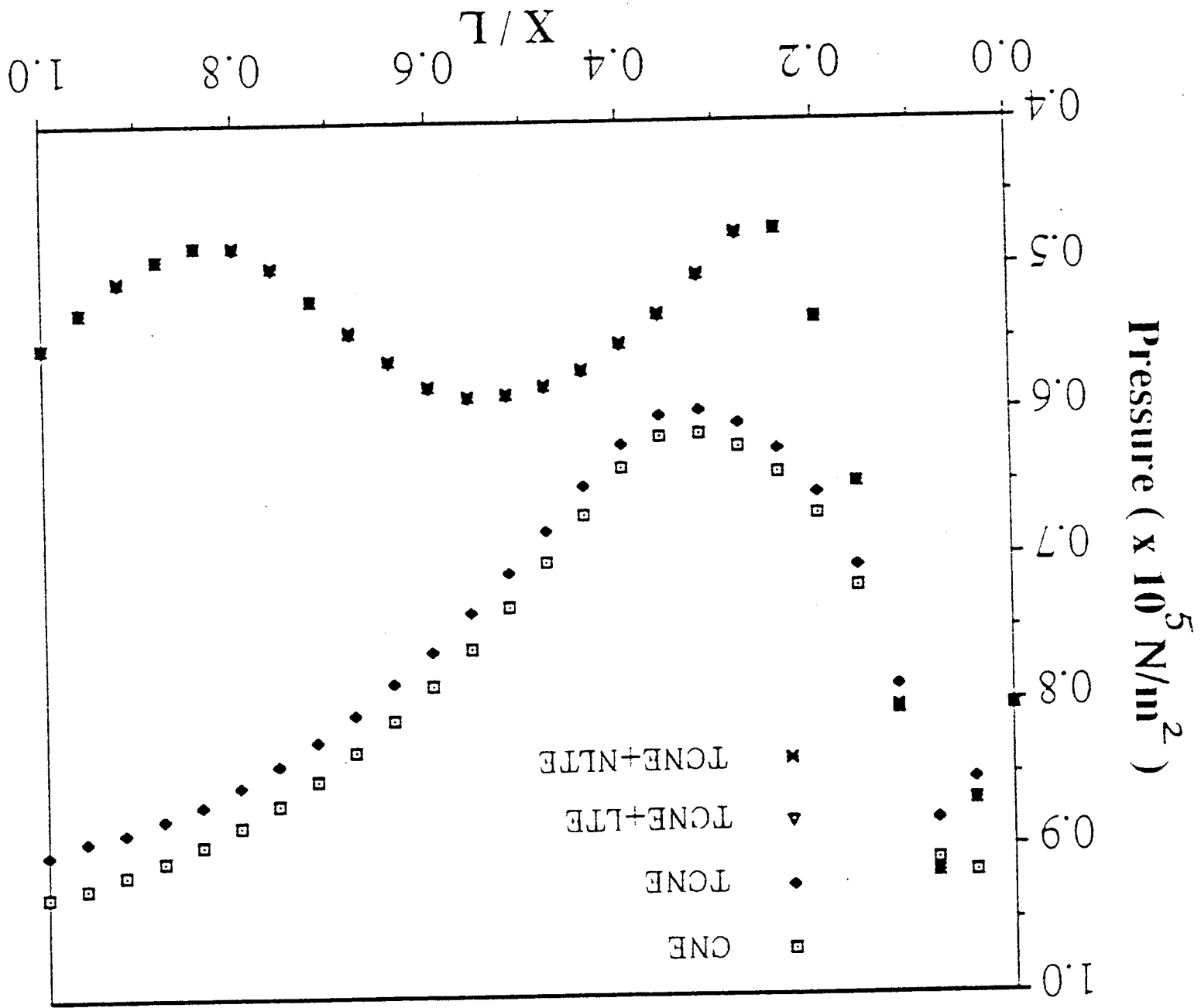


Fig. 5.19b Pressure profiles ($U = \text{jmid}$)

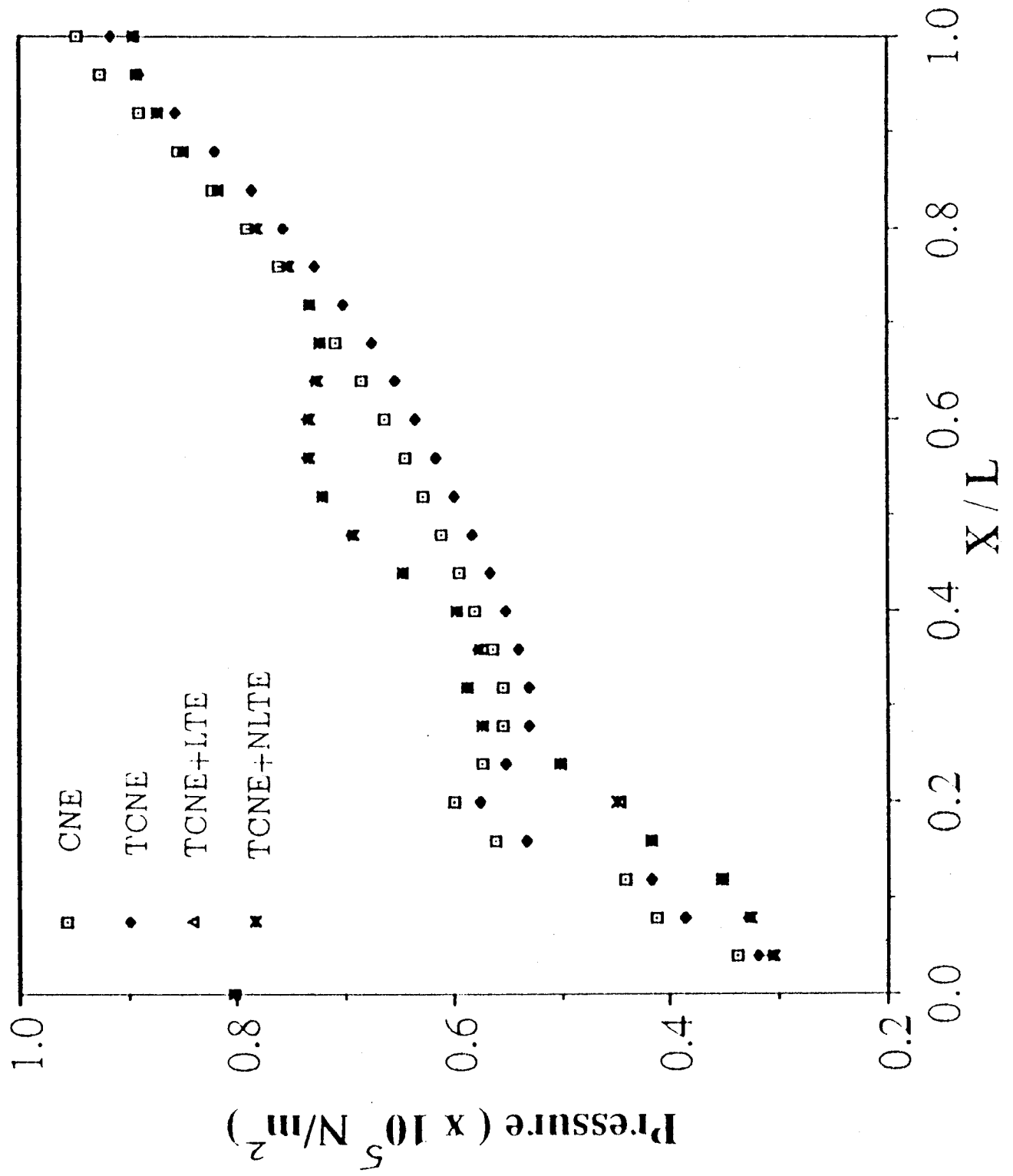
Fig. 5.19c Pressure profiles ($j = j_{\max}-1$)

Figure 5.20 shows variations of the vibrational temperature at three y locations. An interesting effect of radiative interactions is to reduce the vibrational temperature, thereby negating the effect of thermal nonequilibrium. A similar observation has been made in [67]. The reduction in vibrational temperature is due to the q_{R_x} flux which reduces the total energy.

Figure 5.21 shows profiles of water mass fraction at three y locations. They follow a pattern similar to the temperature and pressure profiles (Figs. 5.18 and 5.19). The peak water production is found to occur at $x/L_x = 0.05$. Thus, it can be seen that the nonequilibrium parameter in Eq. (3.13) serves to illustrate the relative importance of vibrational relaxation (collision process) over radiative relaxation (emission process). The non-LTE process is emission dominated. On the other hand, the LTE process is collision dominated.

5.3 Turbulence-Chemistry Interactions

Studies were conducted to investigate the extent of turbulence-chemistry interactions in supersonic flows undergoing hydrogen-air chemical reactions. The SPARK code was modified to include a Reynolds stress turbulence model [89]. The essential modifications in the present work result in the program's capability to compute axisymmetric flows and nonpremixed hydrogen-air combustion. Furthermore, a Beta-PDF has been incorporated into the computer code. In order to avoid expensive computer usage, the chemistry model used in this study is a truncated 7-species, 7-step mechanism derived from the first seven reactions in Table 2.1. The resulting formulation is validated by comparison with experimental data on reacting supersonic axisymmetric jets. The physical models considered for this study, deal with the nonpremixed combustion of supersonic coaxial jets. These are the Beach experiment [89] and the Jarrett-Pitz experiment [90]. Firstly,

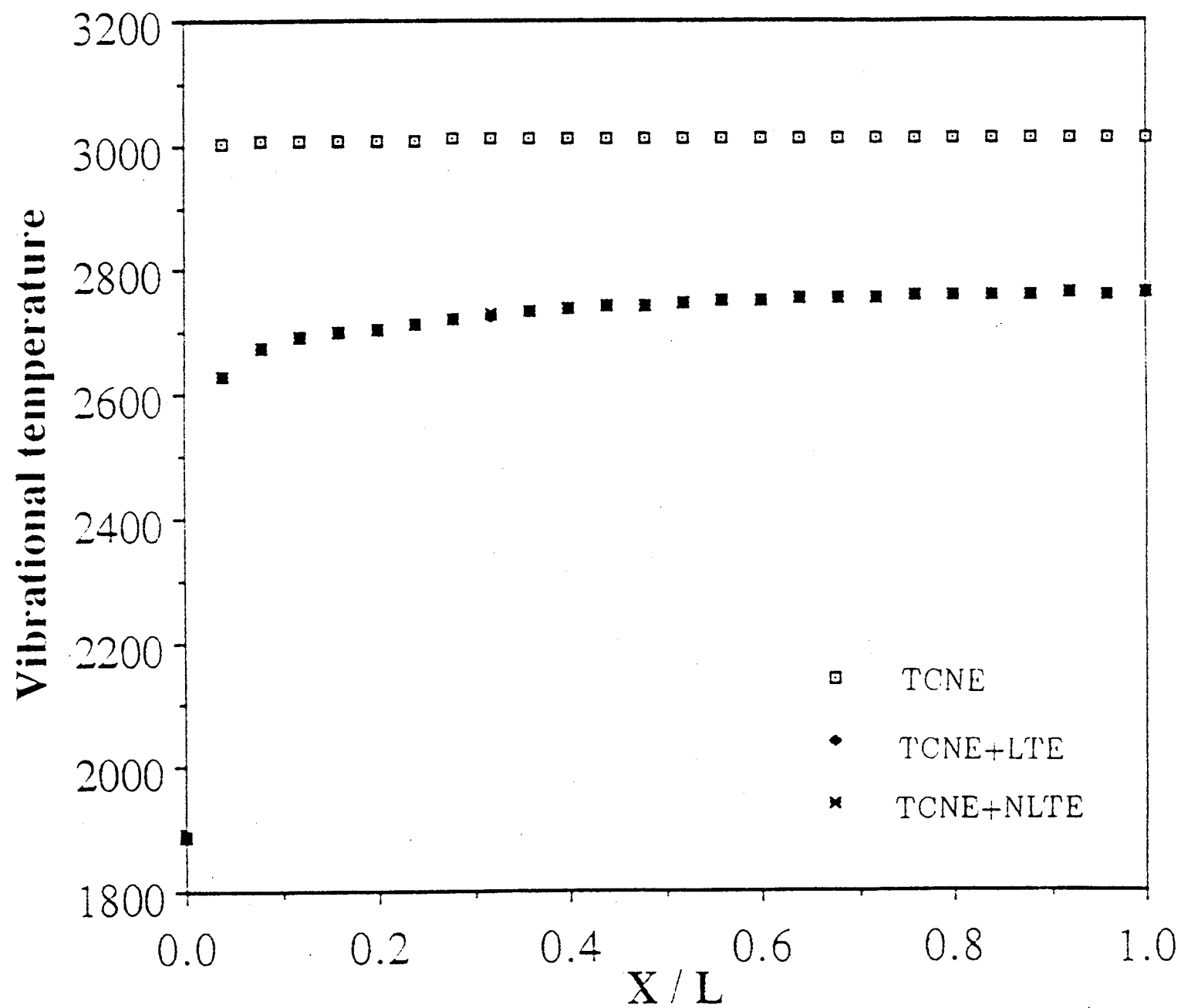


Fig. 5.20a Vibrational temperatures ($j = 1$)

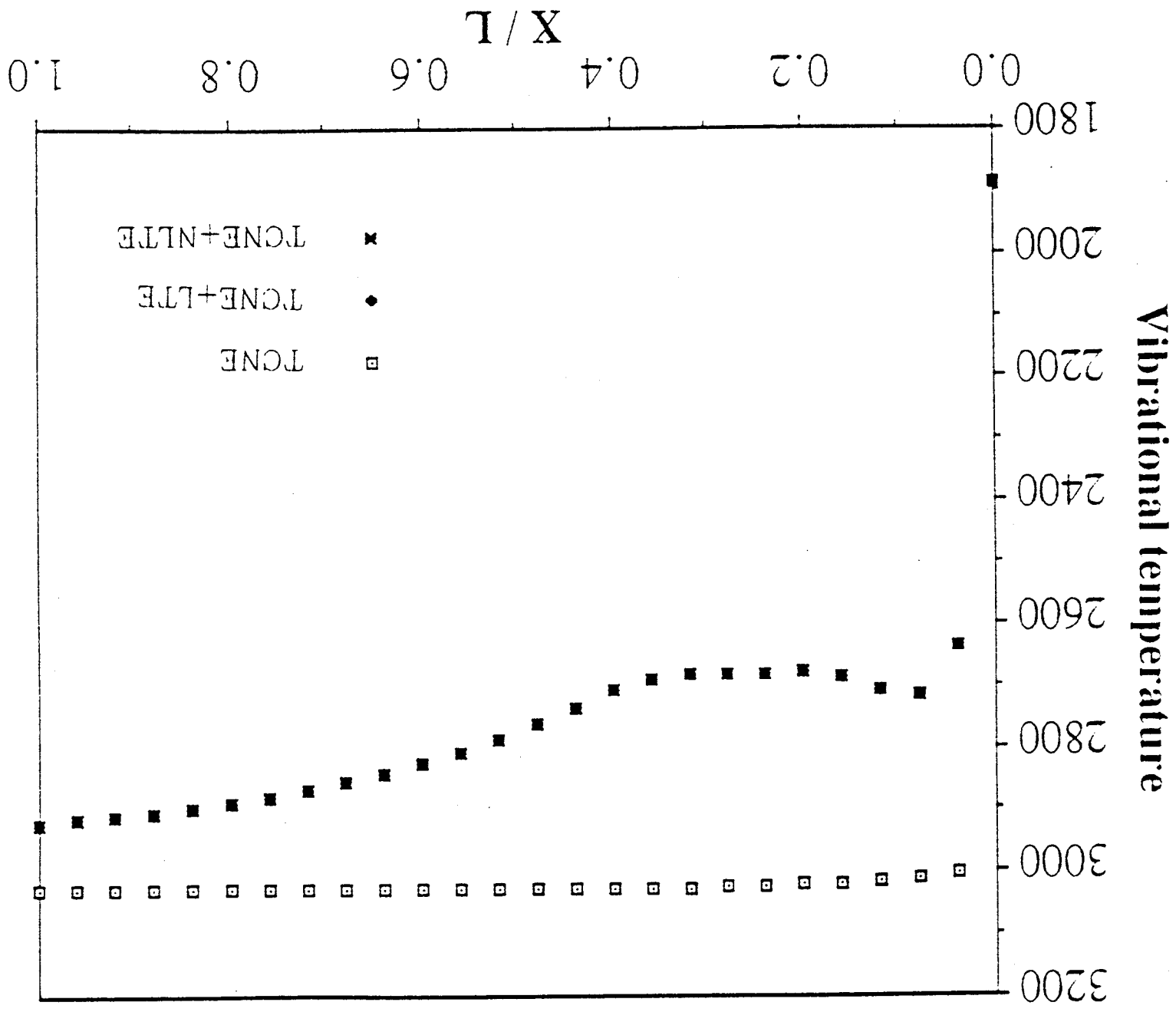
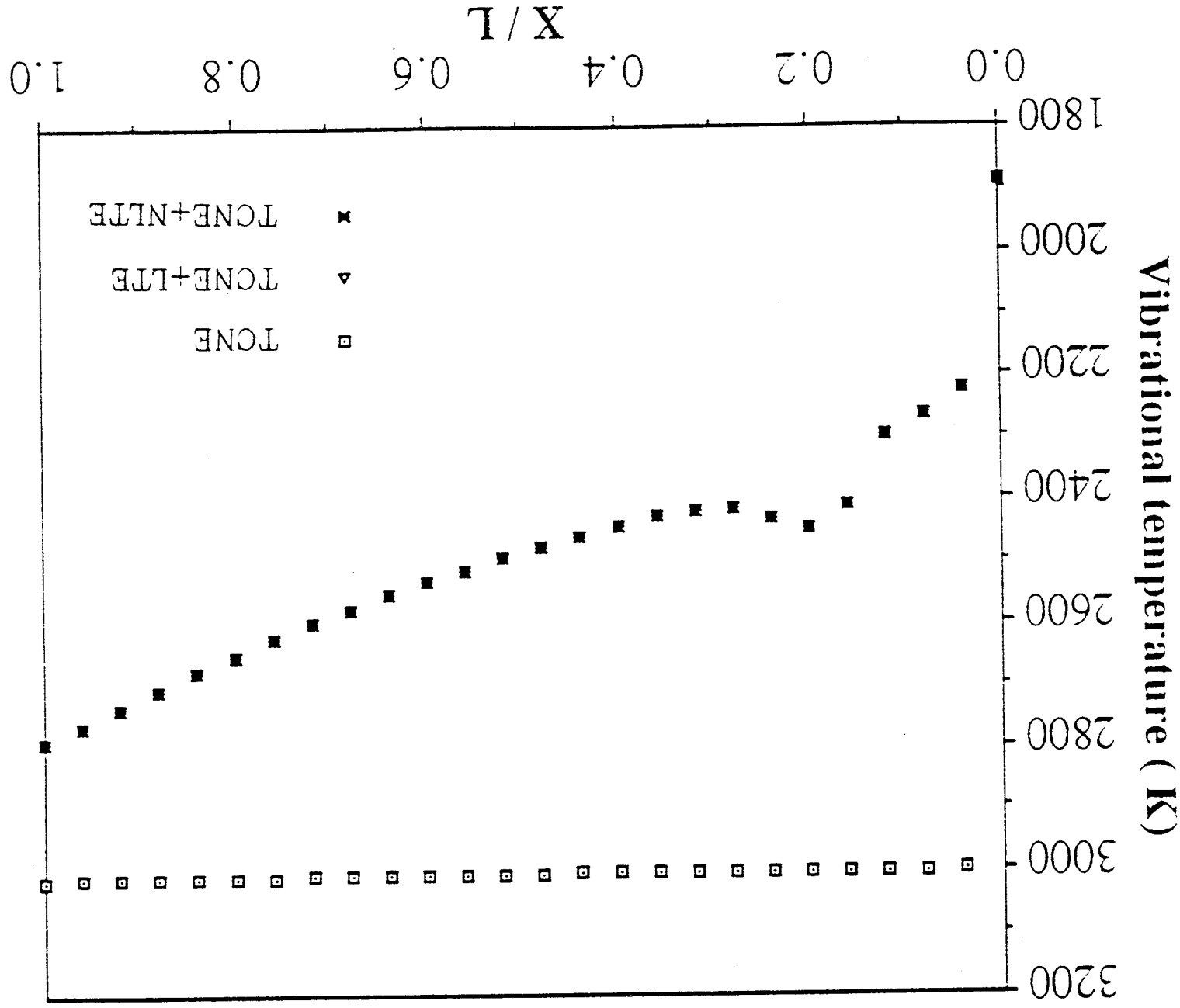


Fig. 5.20b Vibrational temperatures ($\eta = \eta_{\text{mid}}$)

Fig. 5.20c Vibrational temperatures ($i = i_{\max} - 1$)



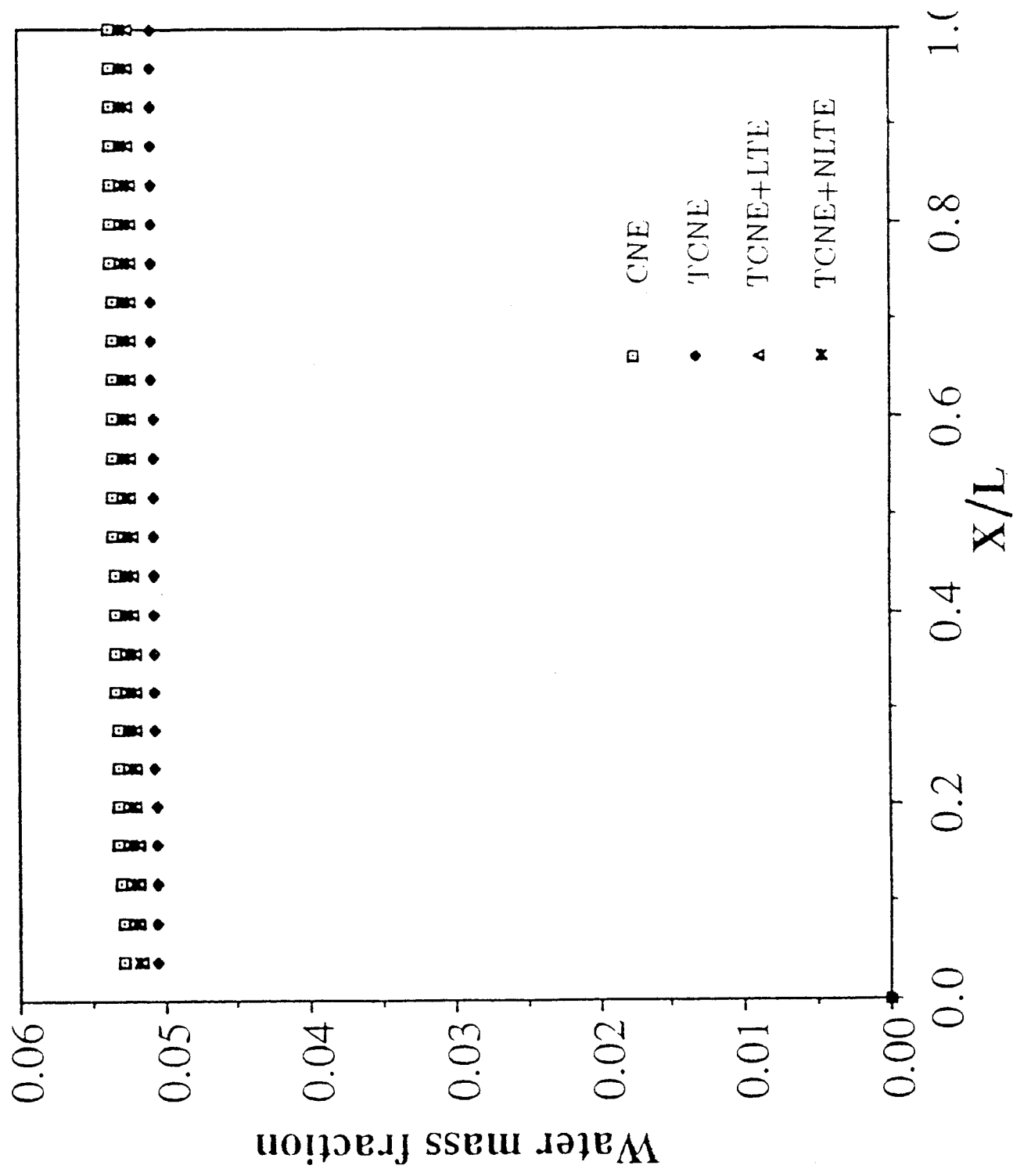


Fig. 5.21a Water mass fraction profiles ($j = 1$)

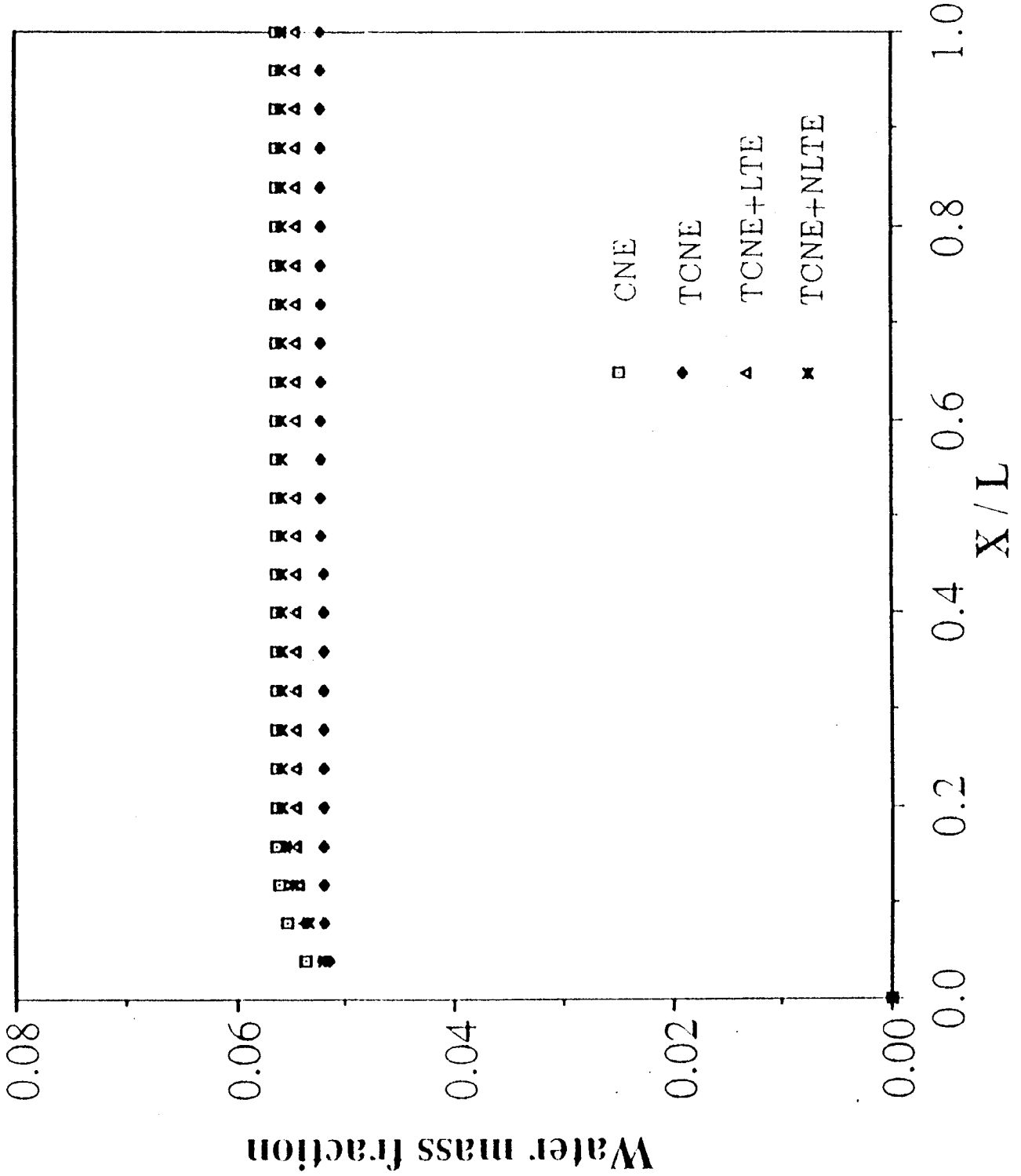


Fig. 5.21b Water mass fraction profiles ($i = \text{imid}$)

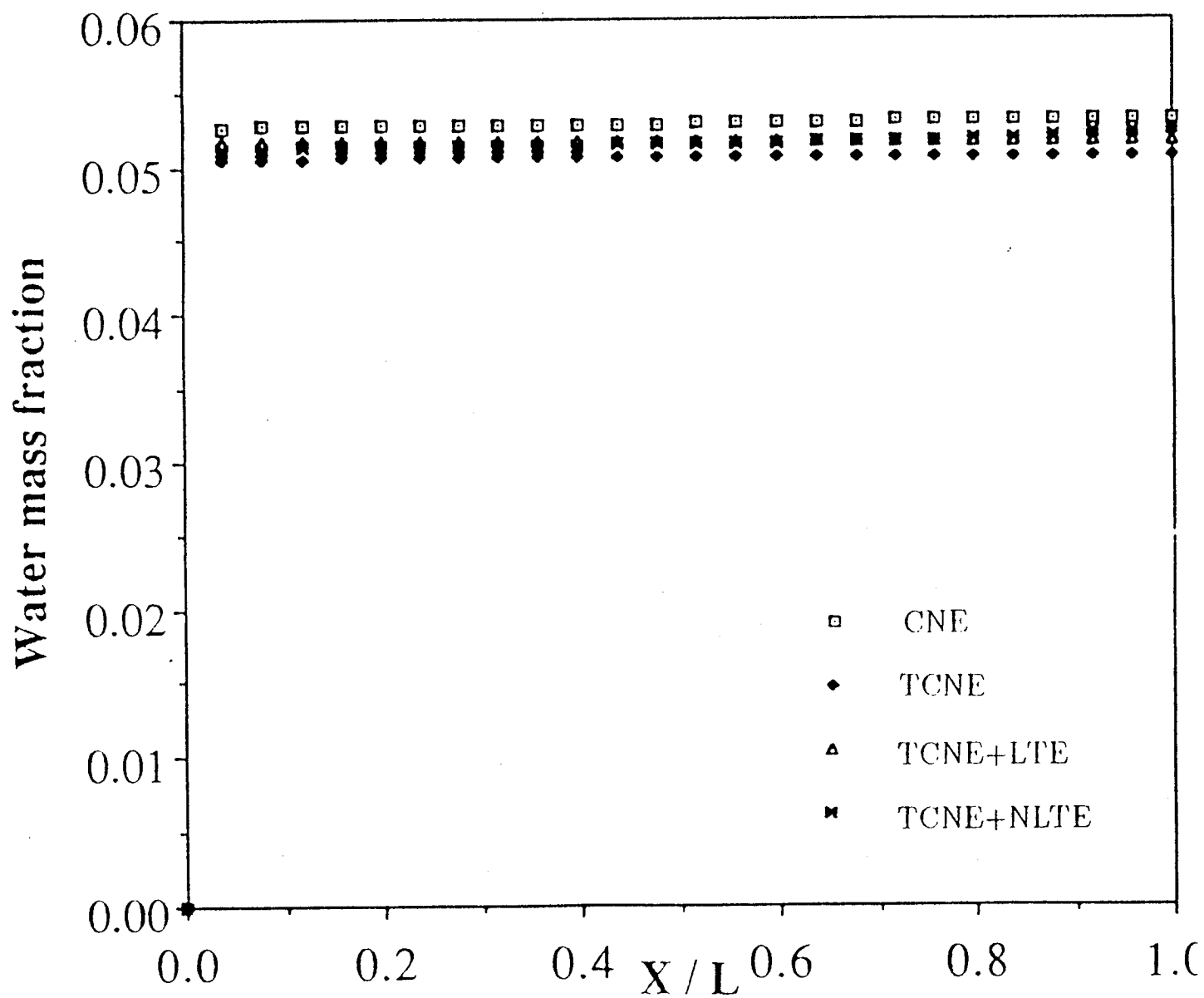


Fig. 5.21c Water mass fraction profiles ($j = j_{\max}-1$)

the computed results for the Beach case will be discussed, and this will be followed by the results for the Jarret-Pitz case.

Figure 4.1 describes the physical model for the Beach and Jarrett-Pitz experiments. The temperature and other exit conditions for the Beach experiment [89] are given in Table 4.1. The outside diameter of the fuel nozzle ($d = 0.009525$ m.) is used to normalize the axial and radial profiles. The length of the flow domain is taken to be 28 diameters, i.e., $x = 0.2667$ m. Initial profiles for the flow variables are obtained by computing flat plate solutions. This is carried out separately for the fuel and air streams and then the two flows are combined. This approach is better than the "ad-hoc" initial profiles chosen by several authors [86, 87]. Figure 5.22 shows the initial temperature profile in the radial direction. The peak temperature is a result of assuming a constant wall temperature of 1700 K for the flat plate flows.

Figure 5.23a shows the density profiles using 61×61 and 81×81 grids, for the purpose of a grid resolution study. It appears that the 61×61 grid is sufficient for the present study. Figure 5.23b shows radial profiles of the major species concentrations at an axial location of $x/d = 8.26$. The computed results are compared with experimental data and the H_2 and N_2 profiles show reasonably good comparison at all radial locations. A good match for the O_2 profiles can be seen at locations greater than or equal to $r/d = 0.6$. This is also the case with the profiles of H_2O mass fraction, where the peak of the flame in the central jet can be observed. Discrepancies between computed and experimental results can be attributed to inadequate predictions of turbulent mixing and initial conditions.

In order to investigate the extent of turbulent mixing, it is possible to examine a mixing scalar, known as the mixture fraction f , which is defined as the normalized mass fraction of an atomic element originating from one of the input streams, viz. usually the

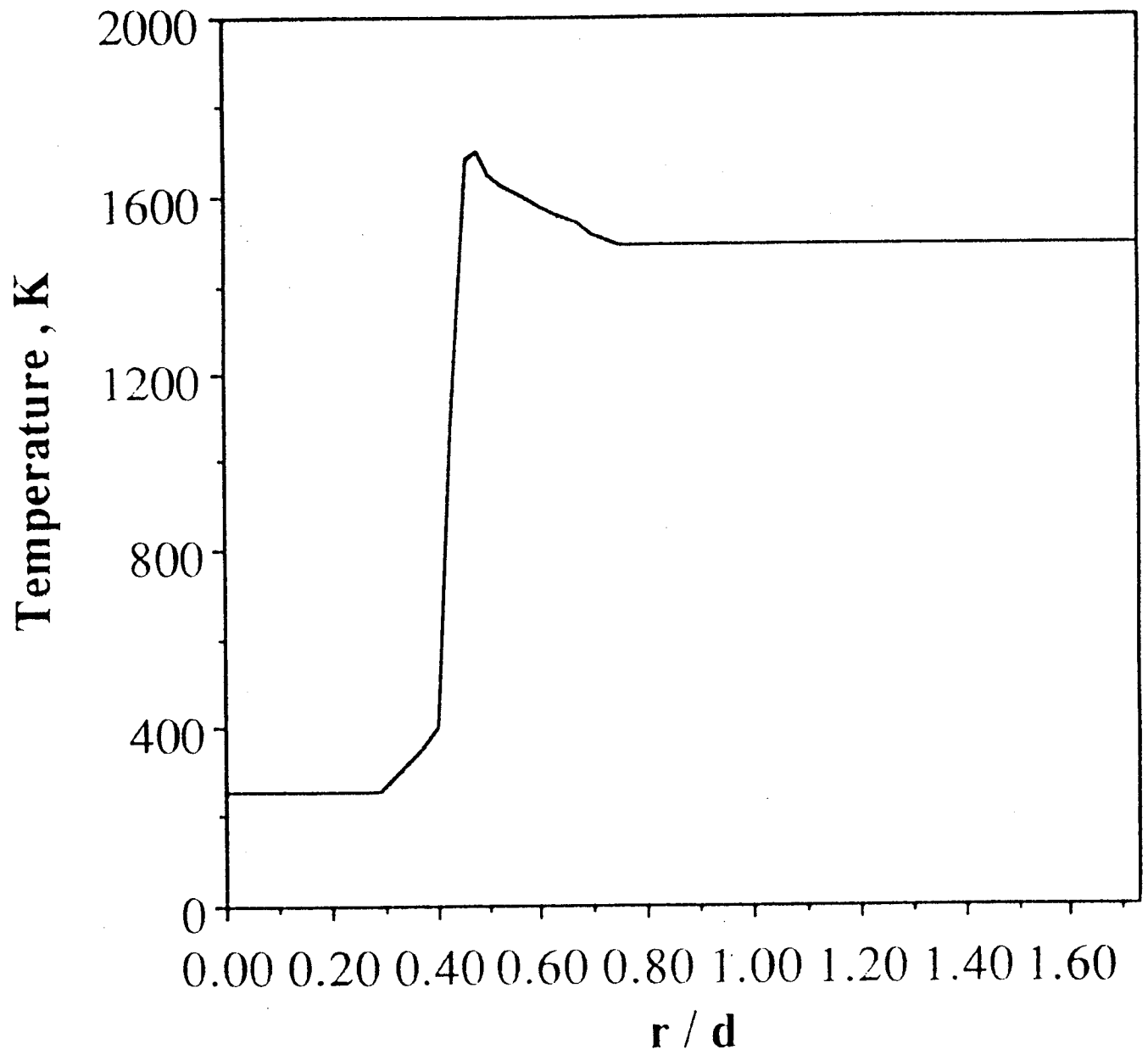
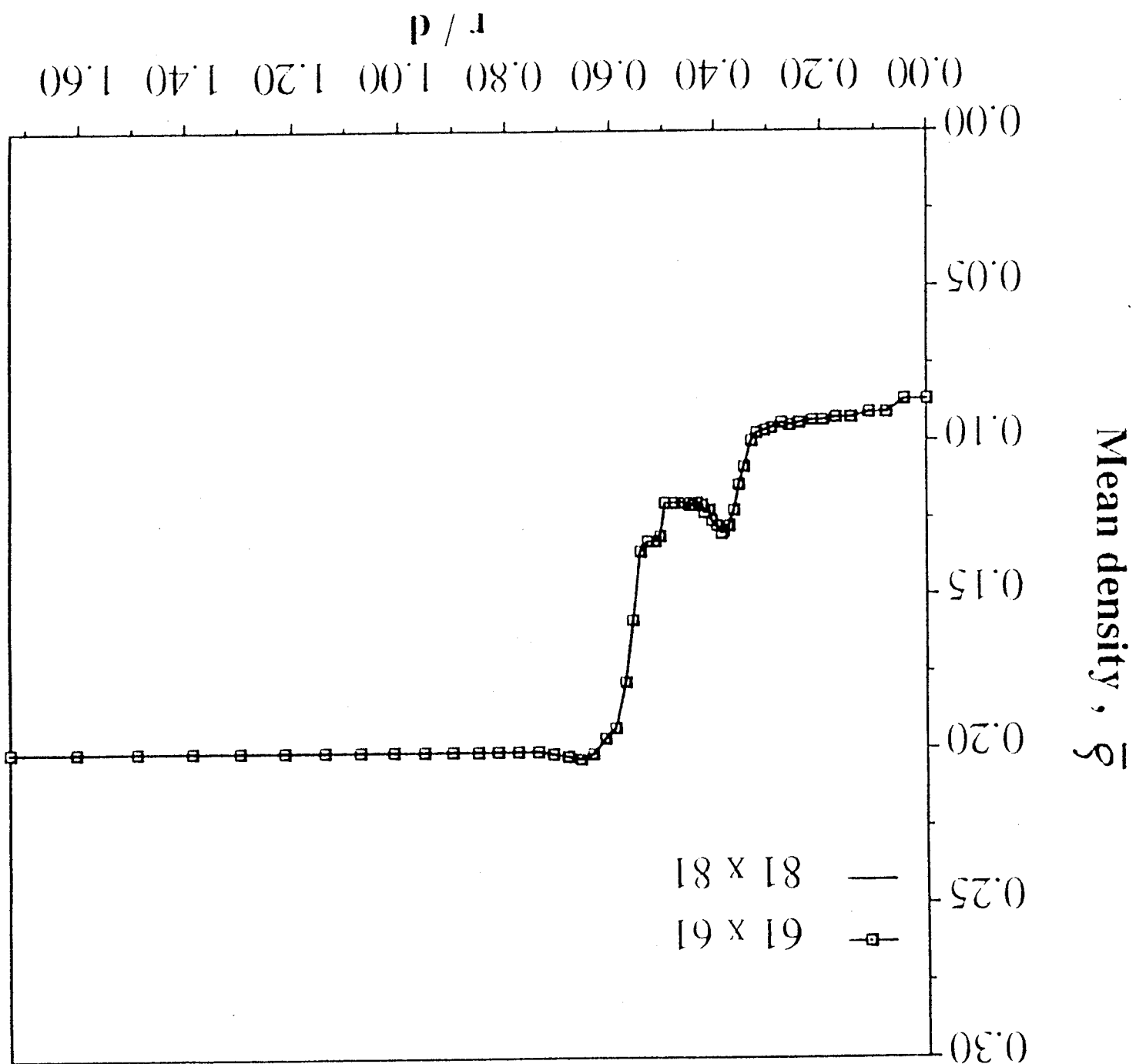


Fig. 5.22 Radial profile of initial temperature

Fig. 5.23a Grid resolution study on mean density



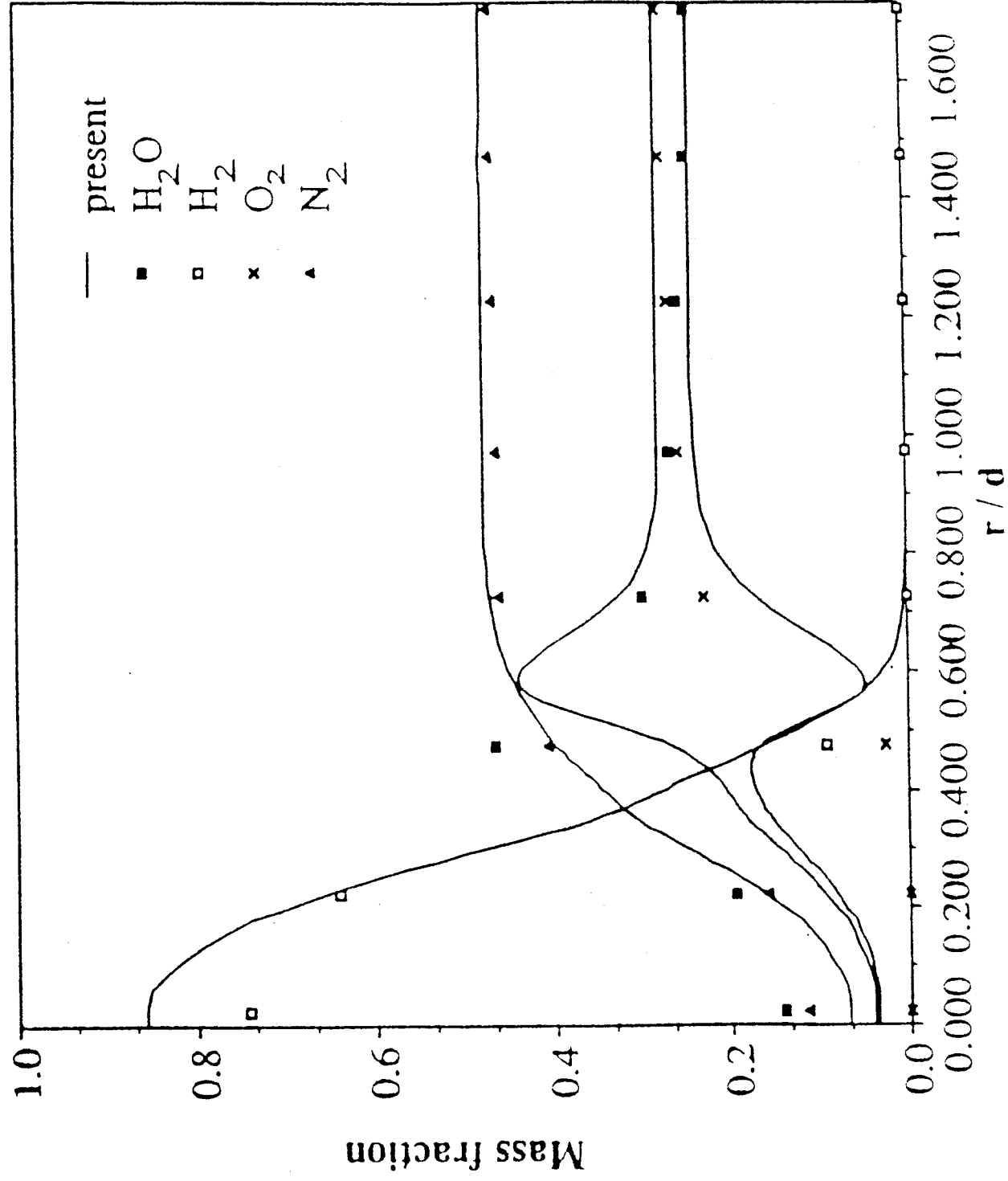


Fig. 5.23b Profiles of major species concentrations

fuel stream. The variable f can only vary from zero to one for a two-stream flow. Under the assumption of equal diffusivities of all species, the mixture fraction is independent of the progress of the chemical reaction. This is an important characteristic of the mixture fraction and serves to indicate the extent of mixing. Experimental data for the mixture fraction are deduced from the measured mass fractions of the major species, using H as the conserved element, i.e.,

$$f = \frac{f_{H_2} + \frac{2}{18}f_{H_2O} - \frac{2}{18}f_{H_2O}^{\infty}}{f_{H_2}^* - \frac{2}{18}f_{H_2O}^{\infty}} \quad (5.1)$$

where superscripts $*$ and ∞ denote the fuel stream and air stream at the nozzle exit, respectively. A similar analysis has been presented in [73]. Figure 5.24 shows predicted and experimental mixture fraction profiles in the radial direction, at the location $x/d = 8.26$. It can be seen that there is reasonable agreement between the computations and the experiment, except near the centerline $r/d = 0.0$. This implies that the turbulent transport model is satisfactorily predicting the extent of turbulent mixing for regions away from the centerline.

Figure 5.25 shows the predicted radial profiles of the minor species mass fractions. The presence of non-negligible amounts of free radicals denotes the extent of chemical nonequilibrium. Also, higher amounts of O and OH radicals are formed relative to the H radicals.

Figure 5.26 shows the predicted density profile in the radial direction, at the same location $x/d = 8.26$. It can be seen that the density of the inner (fuel) jet is lower than the outer (air) jet. However, the density decreases in the vicinity of the central jet ($r/d = 0.4 - 0.5$). This is due to the heat release from the chemical reactions. Figures 5.27a-b show the radial profile of the normalized turbulent shear stress at the axial location $x/d = 8.26$. It is interesting to observe a localized reduction of turbulent shear stress in

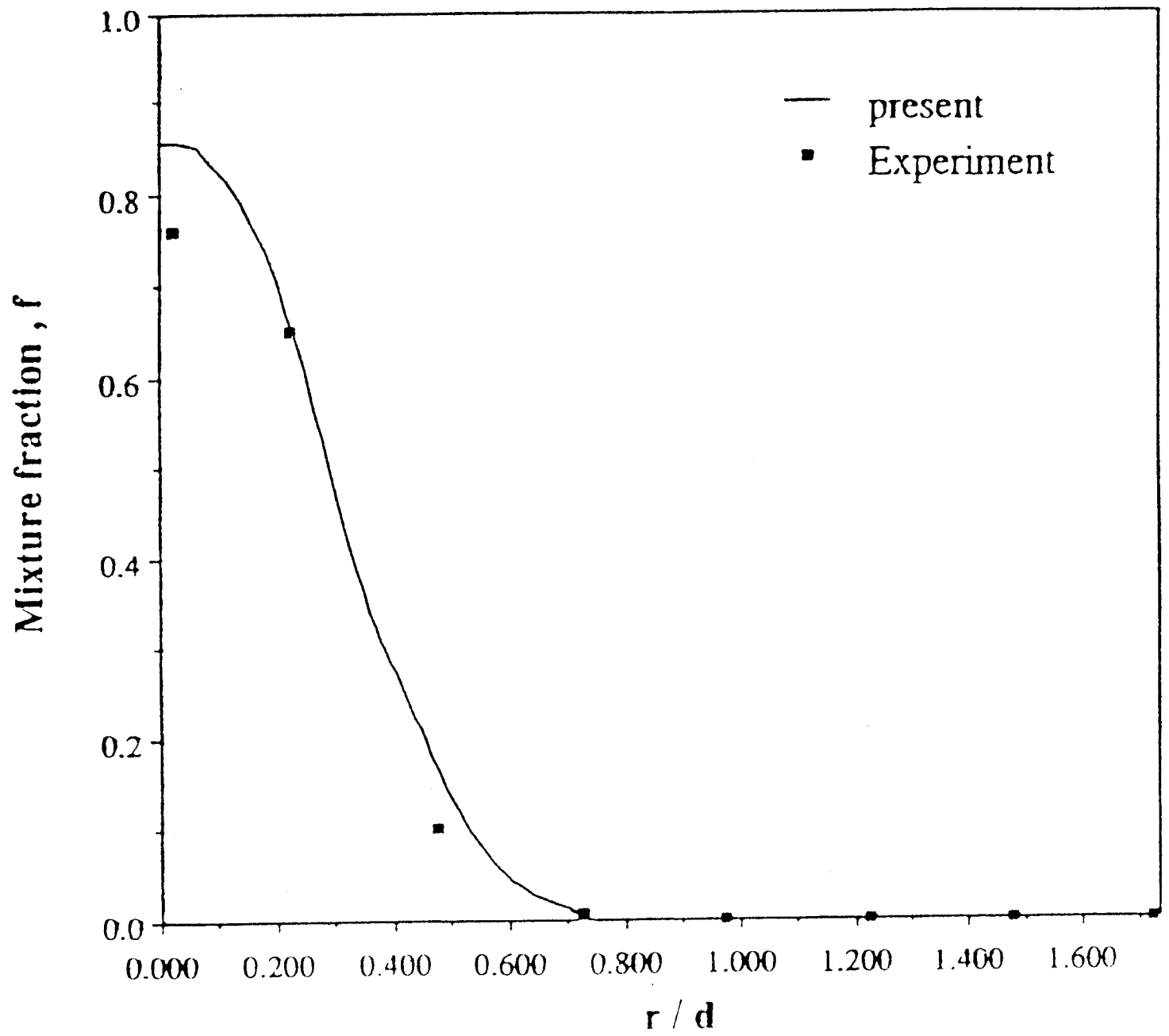


Fig. 5.24 Profiles of mixture fraction

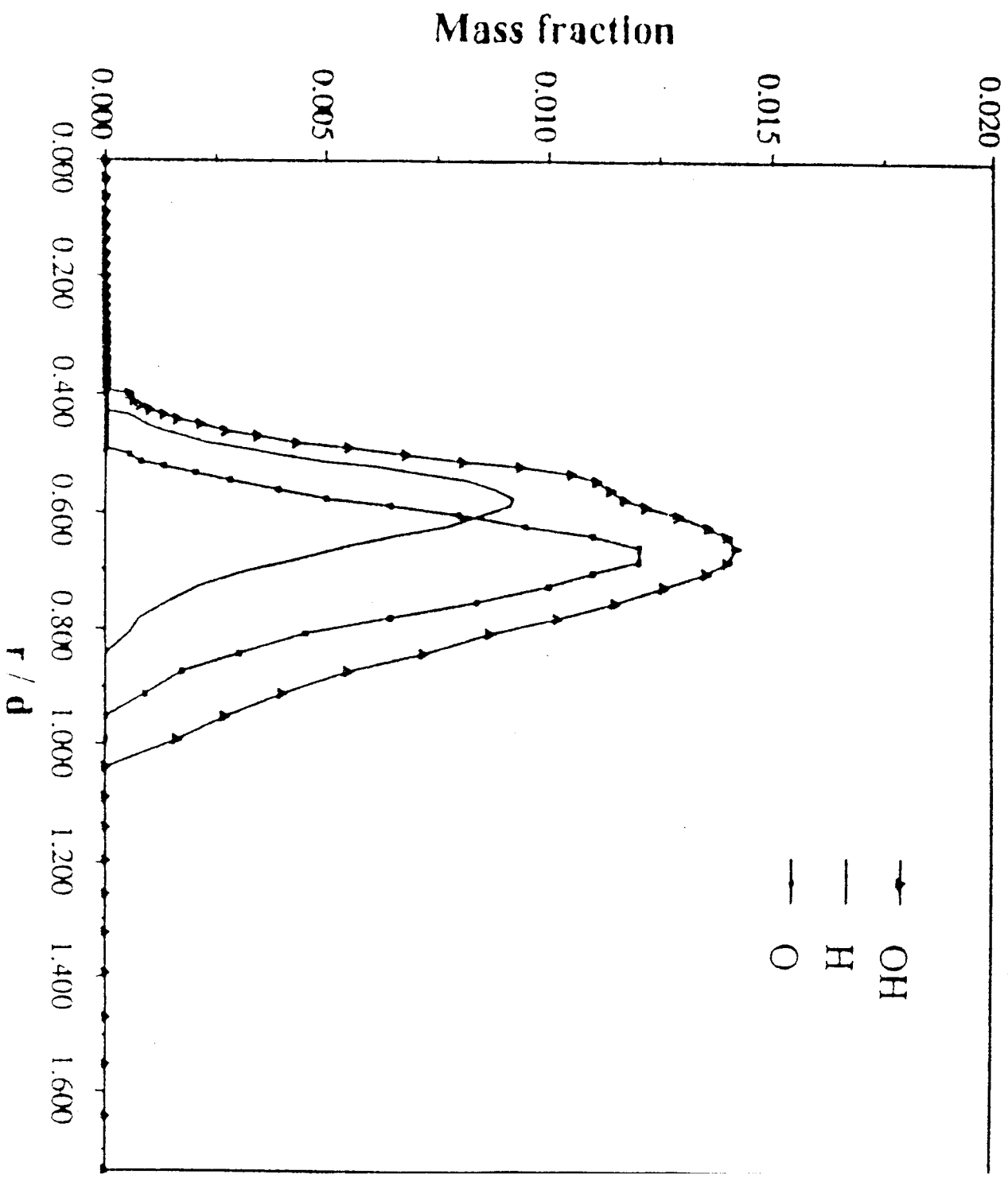


Fig. 5.25 Profiles of minor species fraction

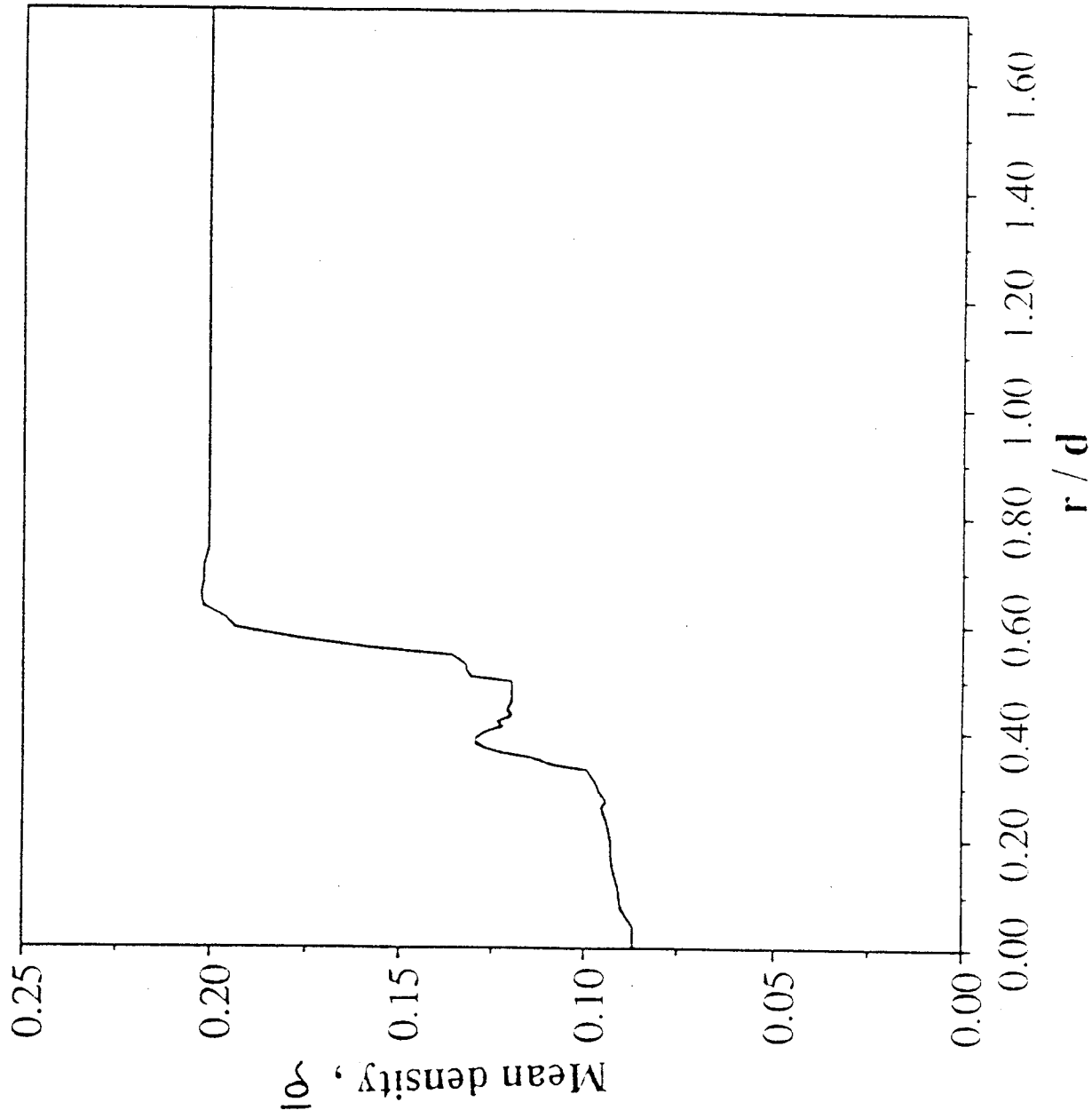


Fig. 5.26 Radial profile of density

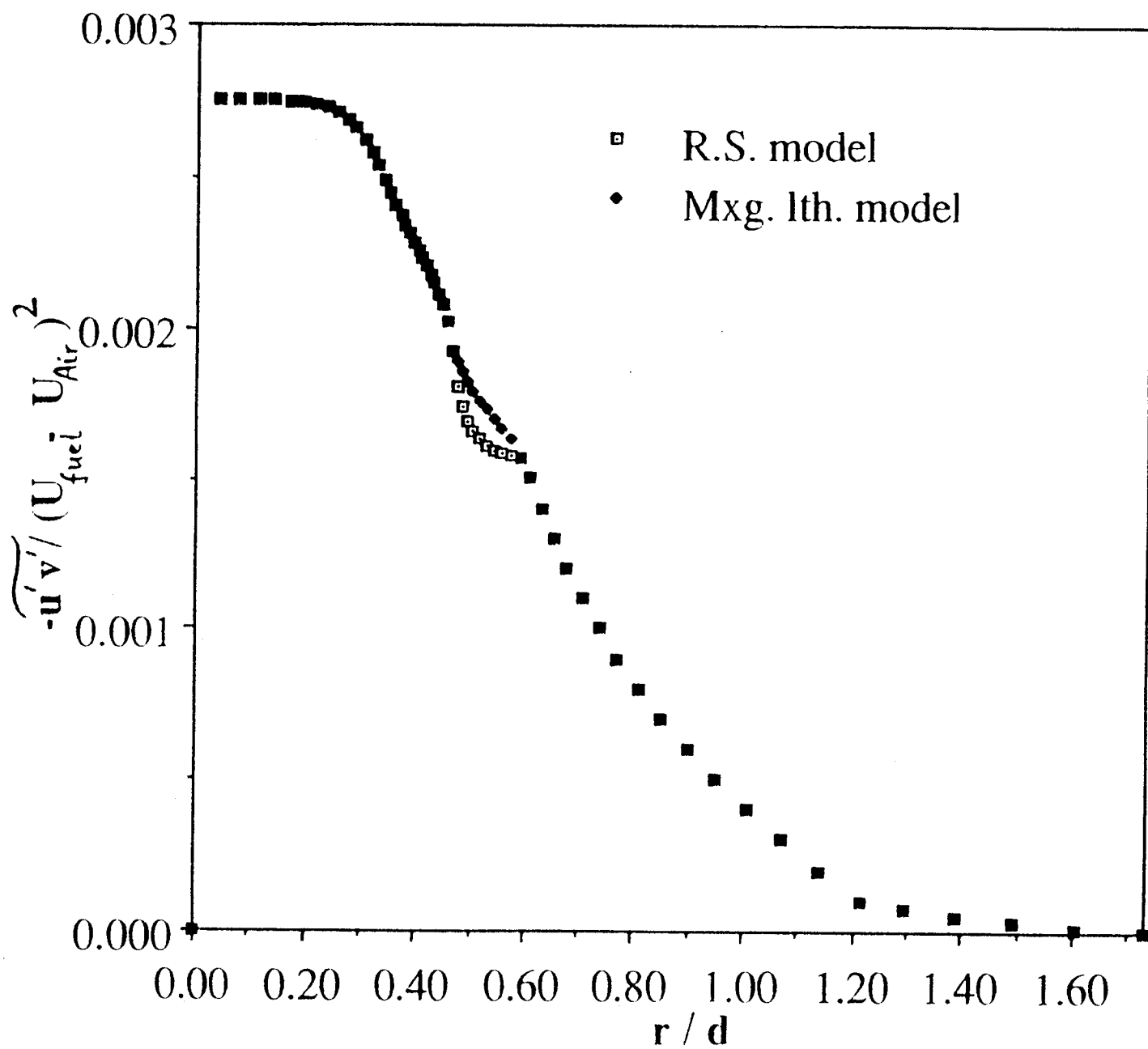


Fig. 5.27a Radial profile of normalized turbulent shear stress

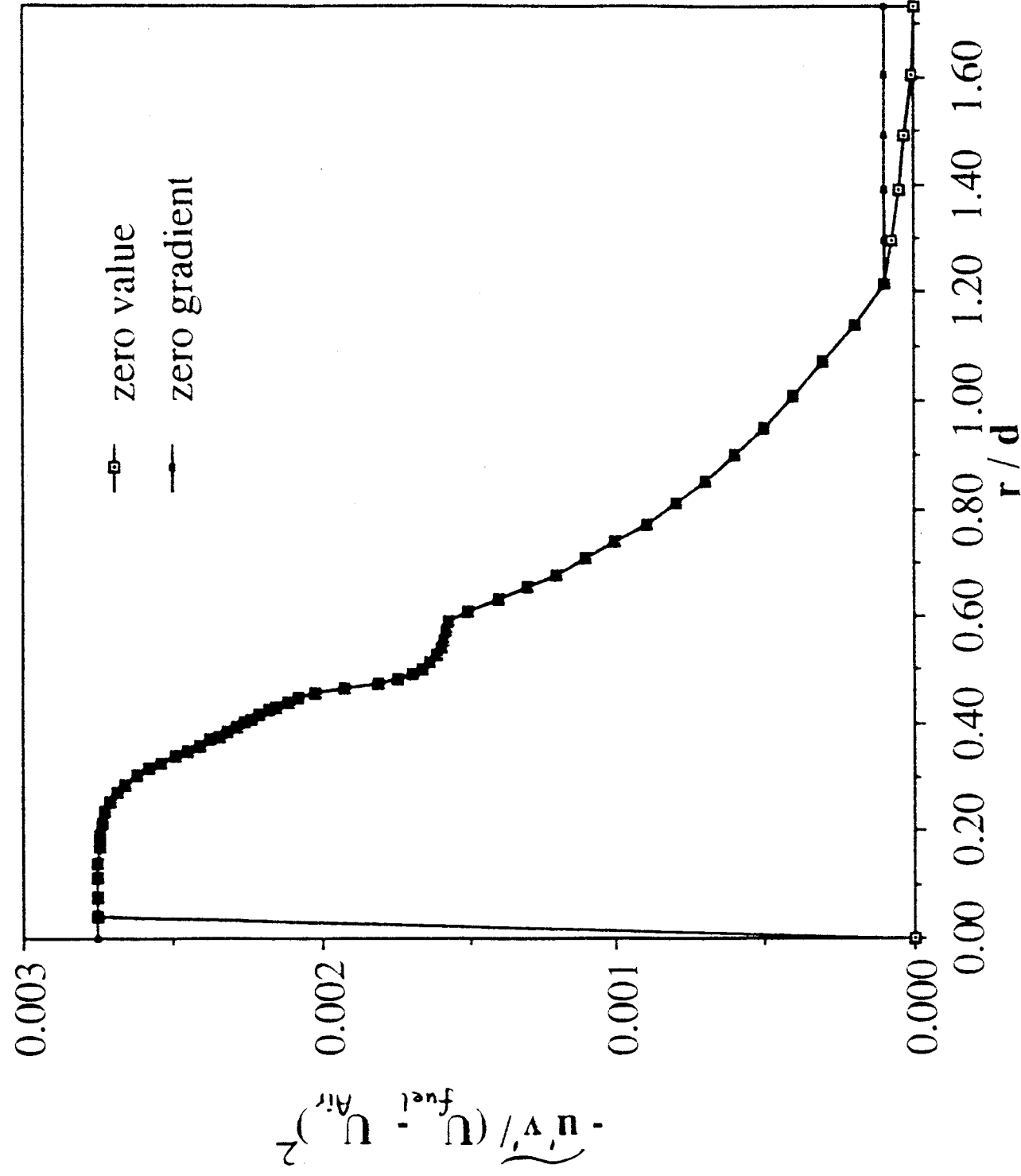


Fig. 5.27b Effect of different B.C.'s on turbulent shear stress

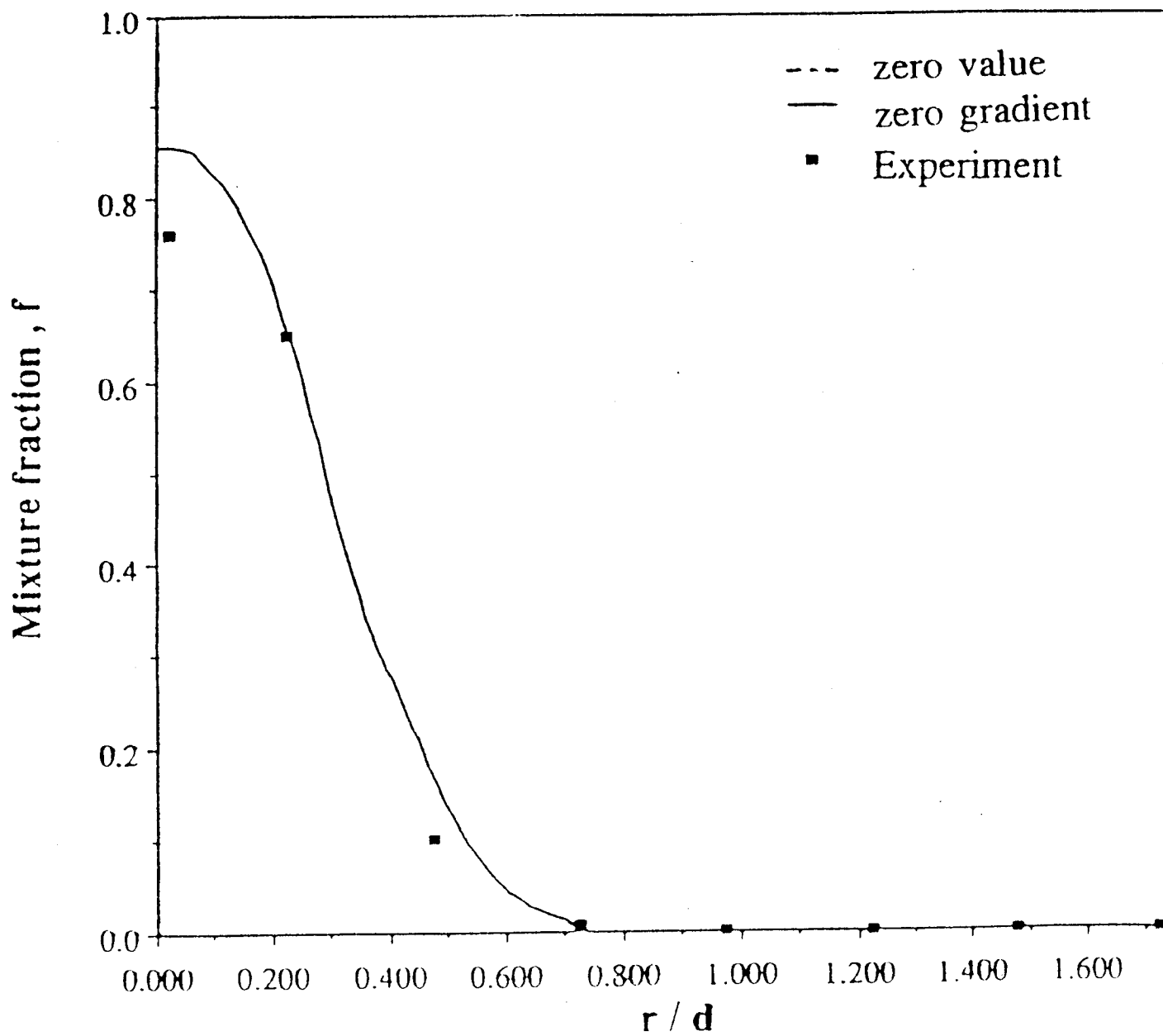


Fig. 5.27c Mixture fraction profile — effect of different shear stress B.C.'s

the same region as the density (Fig. 5.26). This is consistent with the Prandtl's mixing length model

$$\tau = \mu_t \frac{\partial u}{\partial y}, \quad \mu_t = \rho \hat{l}^2 \left| \frac{\partial u}{\partial y} \right| \quad (5.2)$$

where \hat{l} is the mixing length. Equation (5.2) can be expressed as

$$\tau = \rho \hat{l}^2 \left| \frac{\partial u}{\partial y} \right| \frac{\partial u}{\partial y} \quad (5.3)$$

Equation (5.3) suggests that if the mean velocity profile is not strongly altered by heat release, then the turbulent shear stress will decrease with decreasing density. A similar argument has been presented in [92]. Figure 5.27b illustrates the turbulent shear stress profiles using two different boundary conditions, viz. zero gradients or zero value at the boundaries. Figure 5.27c shows that this change in the shear stress boundary condition, does not produce any appreciable change in the mixture fraction.

The schematic diagram for the Jarrett-Pitz experiment [90] is also given by Fig. 4.1. The temperature and other exit conditions for this experiment are given in Table 4.2. The outside diameter of the nozzle ($D = 0.01778$ m.) is used to normalize the axial and radial profiles. The length of the flow domain is taken to be 5.7 diameters, i.e., $x = 0.1016$ m. Initial profiles for the flow variables are obtained by computing flat plate solutions. This is carried out separately for the fuel and air streams and then the two flows are combined. A fixed location of $x/D = 0.85$ is chosen since experimental data are available for CFD code validation.

The mixture fraction is defined in the same manner as in the Beach experiment [89]. Figure 5.28 shows predicted and experimental mixture fraction profiles in the radial direction, at the location $x/D = 0.85$. It can be seen that there is reasonable agreement

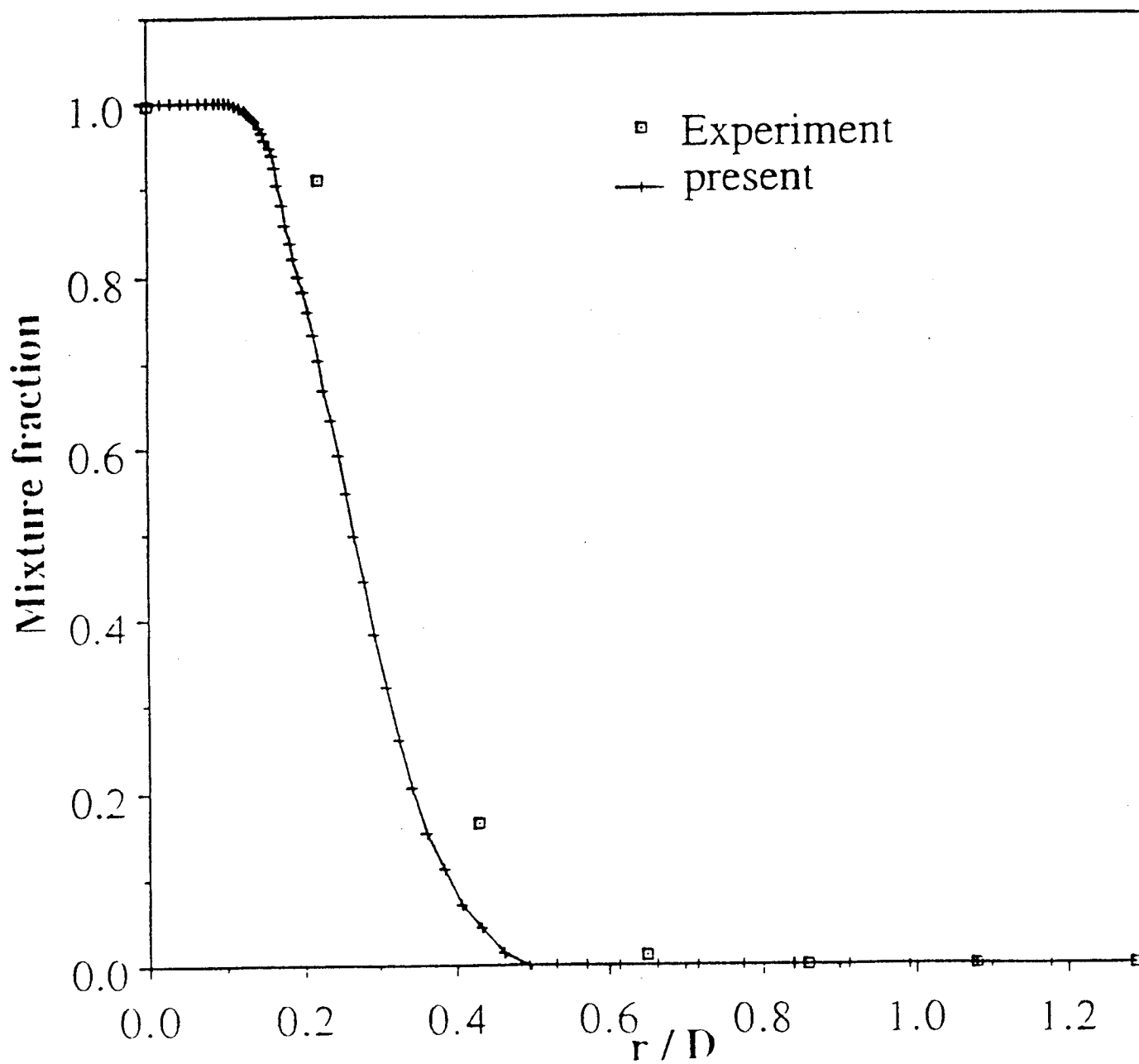


Fig. 5.28 Radial profile of mixture fraction

between the computations and the experiment. This implies that the turbulent transport model is satisfactorily predict the extent of turbulent mixing.

Figure 5.29 shows the predicted and experimental radial profiles of the temperature. The presence of a central peak denotes the main mixing and combustion zone. It can be seen that this peak near 1500 K is predicted correctly. Discrepancy in the location of this peak can be attributed to non-symmetric experimental results. Similar shifting of temperature peaks has been observed earlier [72].

Figure 5.30 shows the radial profile of the water mass fraction, viz. the flame. A peak H_2O mass fraction is observed at the same location as the temperature peak. A more diffuse profile after $r/D = 0.6$ could be achieved, if some OH radical seeding [$\sim 1-3\%$] were carried out. This would alter the ignition profile, as discussed in Sec. 5.1.

Figure 5.31 shows the radial profile of the normalized turbulent shear stress at the same axial location $x/D = 0.85$. It is again interesting to observe a localized reduction of turbulent shear stress in the same region as the flame. This is because of the reduction in density due to heat release.

Figure 5.32 shows the radial profile of the normalized right hand side (R.H.S.) of the turbulent shear Reynolds Stress equation, Eq. (13). It is interesting to note that the initially isotropic (i.e. initial R.H.S. = 0.0) turbulent shear stress undergoes “nonequilibrium” in the region of the diffusion flame. This is because, in the flame region, the R.H.S. is non-zero. Away from the flame, the turbulent shear stress “returns-to-isotropy”. Therefore, this can be termed as a “relaxation” process.

Figures 5.33–5.34 show the effects of three different “pressure-strain” models on the flow characteristics. These models are — LRR (Launder, Reece and Rodi), SSG (Sarkar, Speziale and Gatski), and S-L (Shih-Lumley). Details of the pressure-strain models are

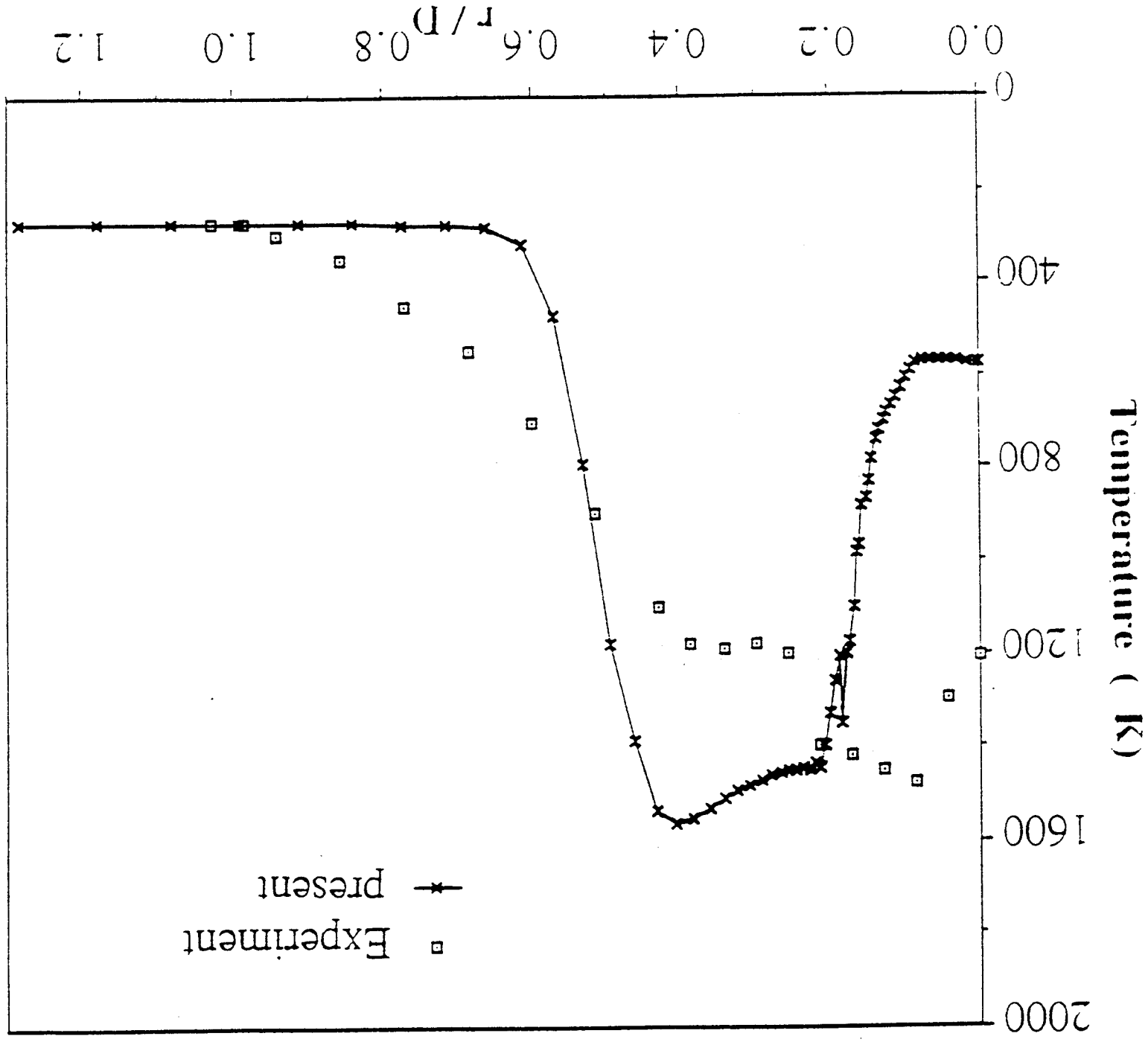


Fig. 5.29 Radial profile of temperature

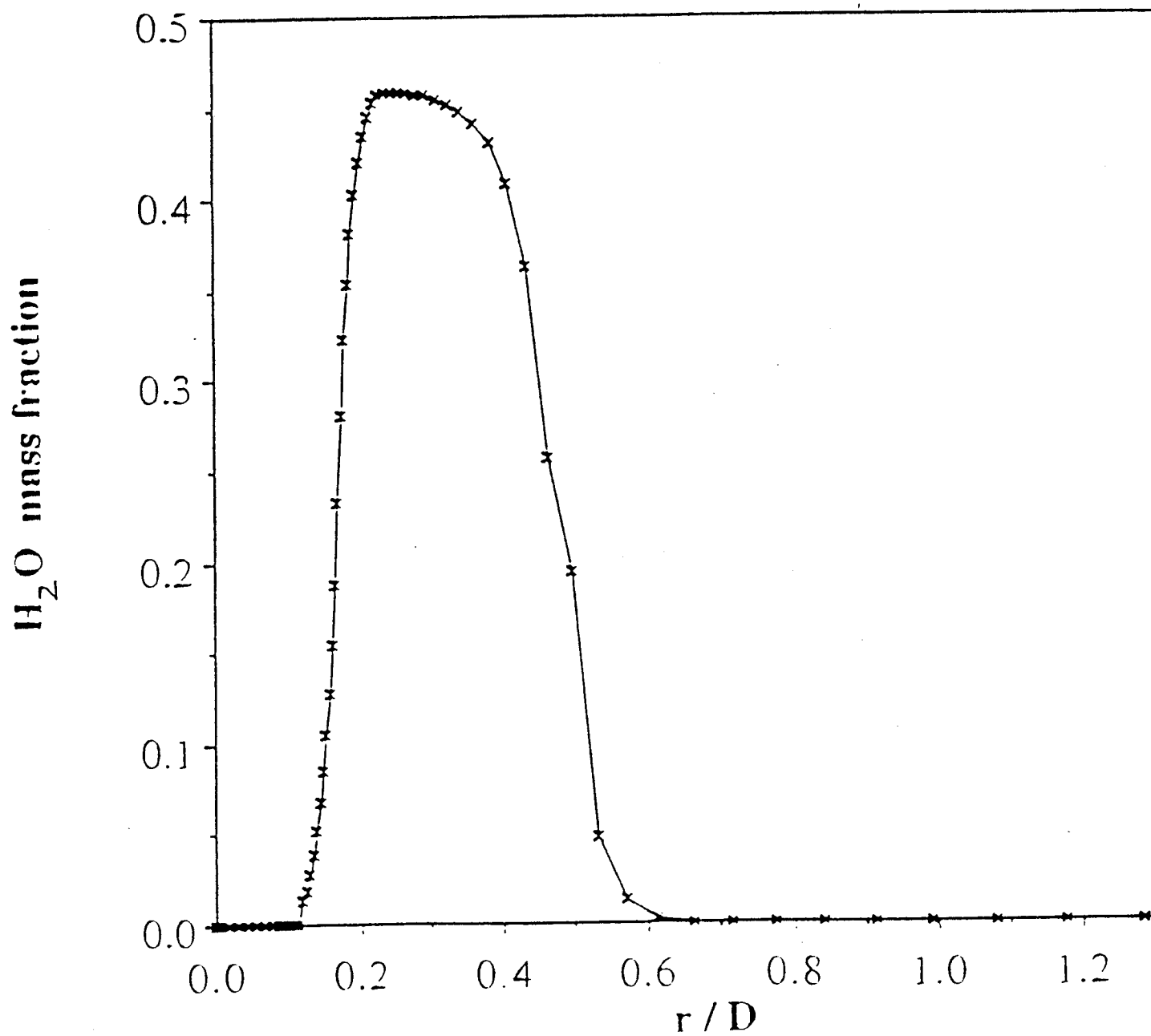


Fig. 5.30 Profile of water mass fraction

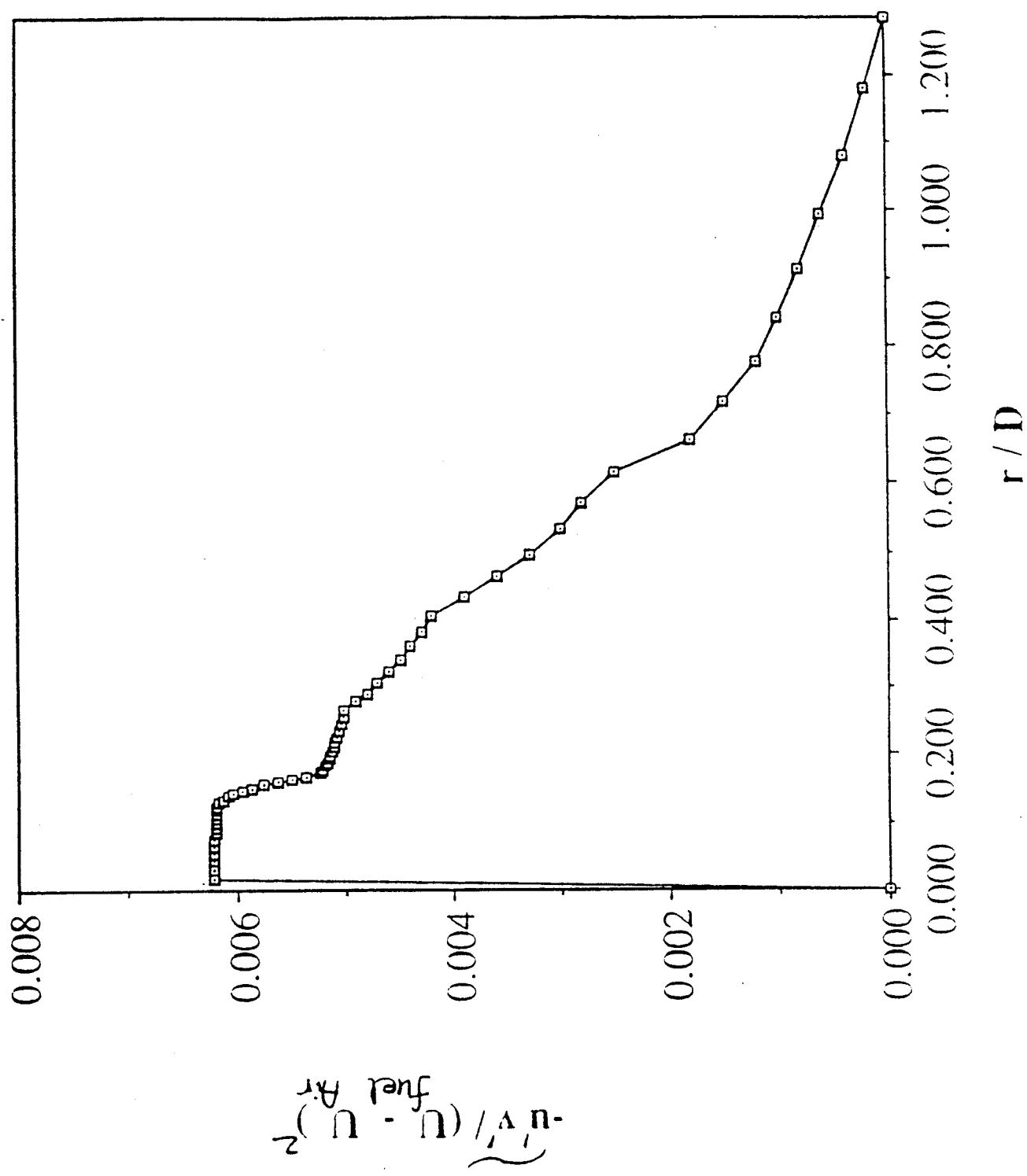


Fig. 5.31 Radial profile of normalized turbulent shear stress

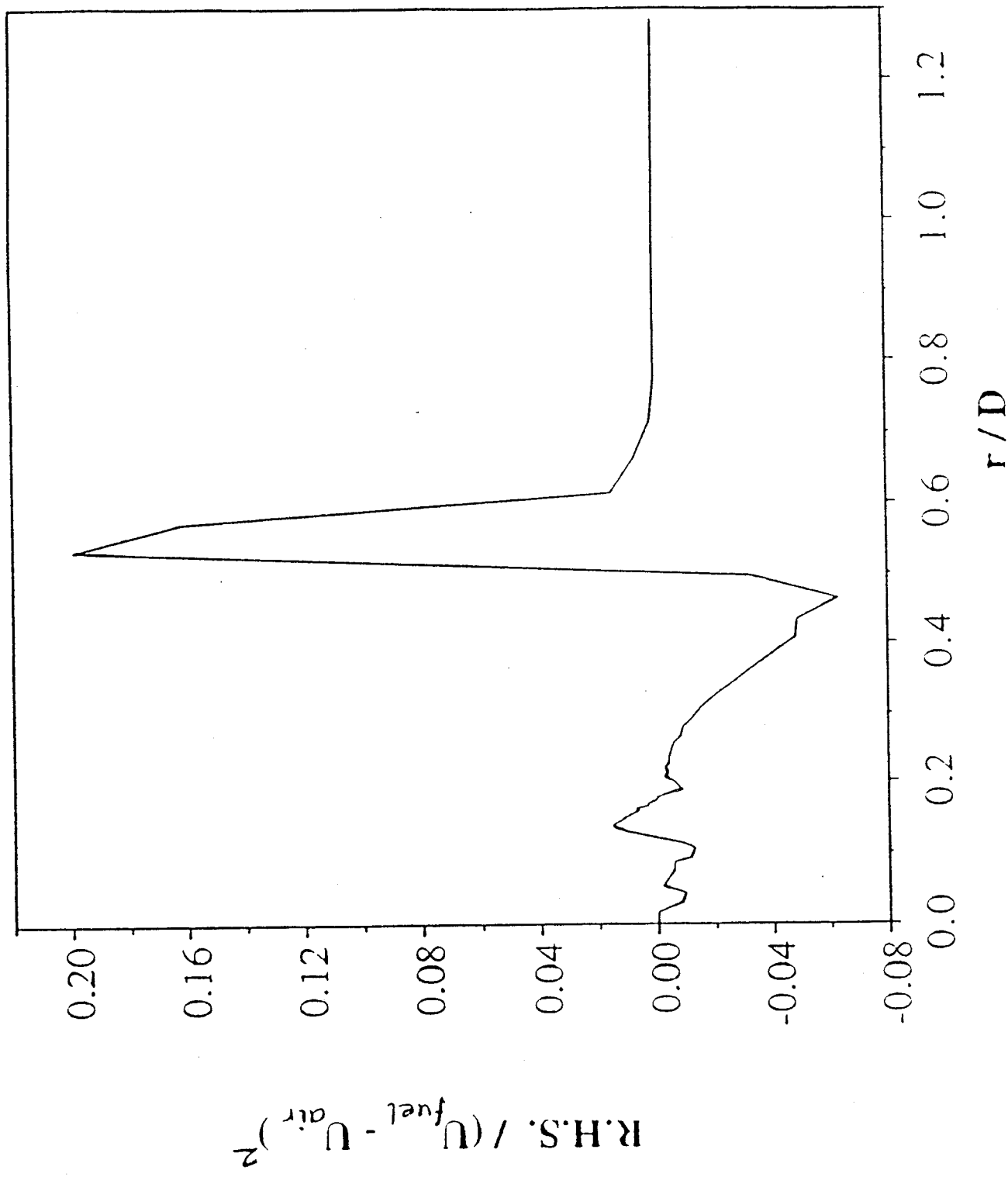


Fig. 5.32 Profile of R.H.S. of $\overline{u'v'}$ equation

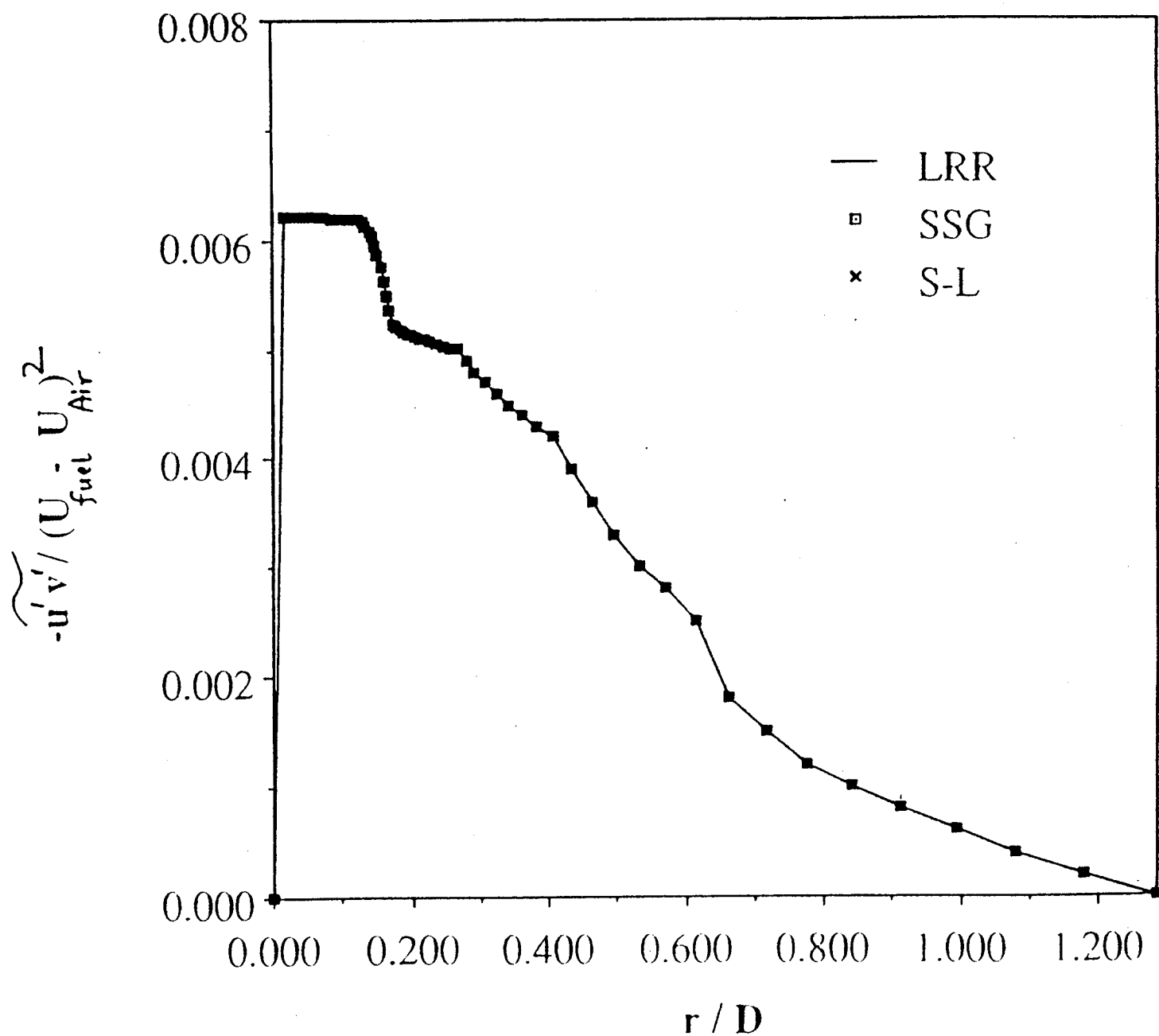


Fig. 5.33 Effect of "pressure-strain" model on turbulent shear stress

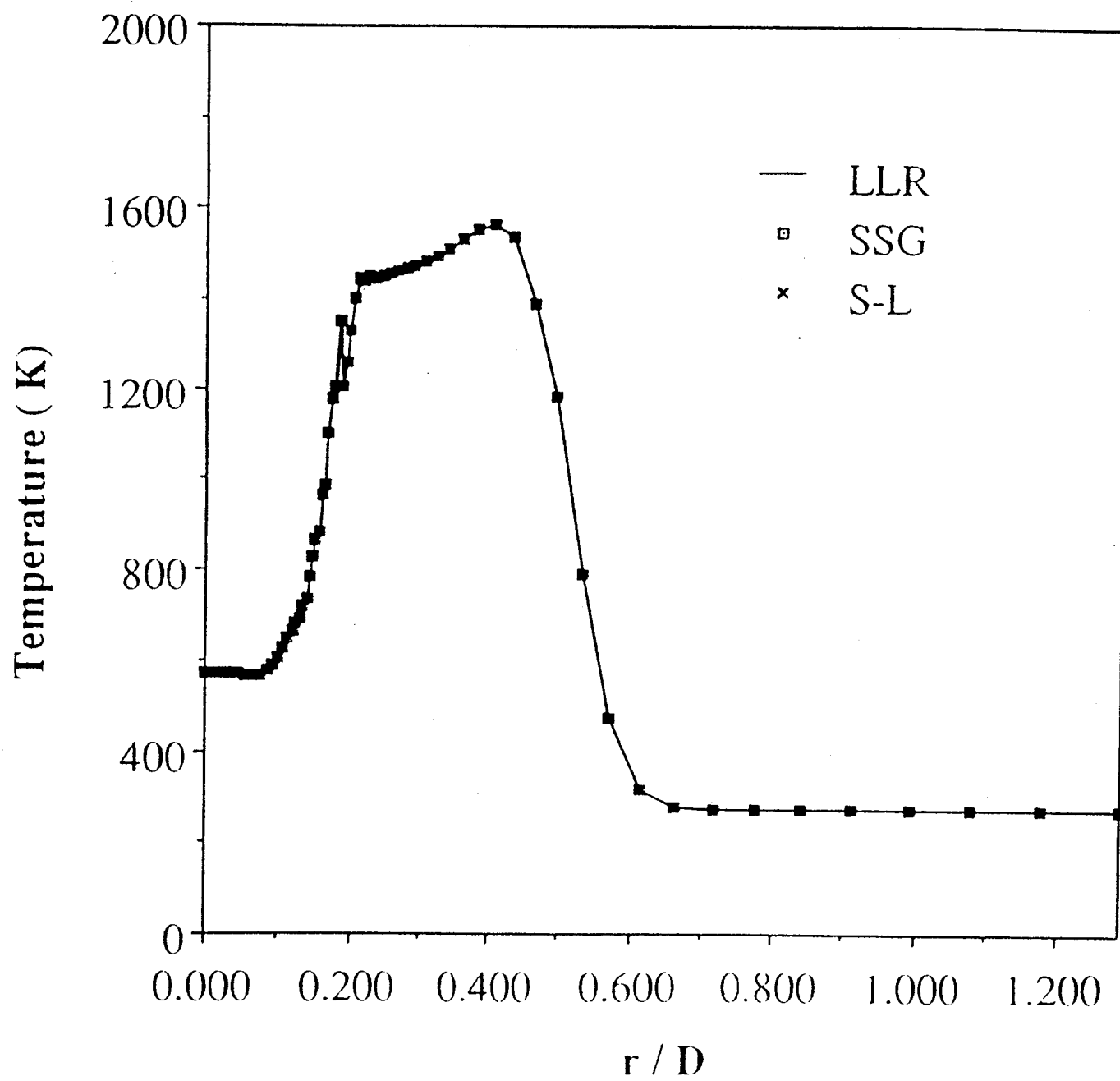


Fig. 5.34 Effect of "pressure-strain" model on temperature

available in [93]. Figure 5.33 shows that there is no difference between the effects of the three pressure-strain models on the normalized turbulent shear stress. Figure 5.34 also shows no difference in the temperature predictions. This is because the flow considered in this study does not have very strong anisotropies, and is mainly combustion-dominated. A similar argument regarding “pressure-strain” models for diffusion flames has been presented in [87]. However other kinds of flows, e.g. swirling combustion, could offer better opportunities for testing these “pressure-strain” models.

Figure 5.35 shows the H_2O mass fraction profile, based a preliminary study conducted on the effect of a multivariate Beta PDF for species fluctuations. Details of this PDF are given in [94]. A special case of the mixing of two scalars was conducted. The N_2 species mass fraction was one scalar and the sum of the remaining species mass fractions was the second scalar. It can be seen from Fig. 5.35 that the species PDF in the present form does not show an effect on the H_2O mass fraction. This is because individual reactions in the chemistry models respond differently to the PDF. Some reaction rates are accelerated, while others are slowed down. Furthermore, some critical reactions are absent from the 7-step model used in this study. A sensitivity analysis for hydrogen-air chemical reactions has been discussed earlier in Sec. 5.1 of this chapter. In addition, chemical equilibrium has likely been reached (reactions have run to completion), implying that changes to the R.H.S. of Eq. (4.12) will not produce significant effects. This is very similar to the result shown in Fig. 5.14, wherein two different methods have been used for computing the vibrational relaxation time. Despite this, the final equilibrium value of T_v , is nearly the same in both cases.

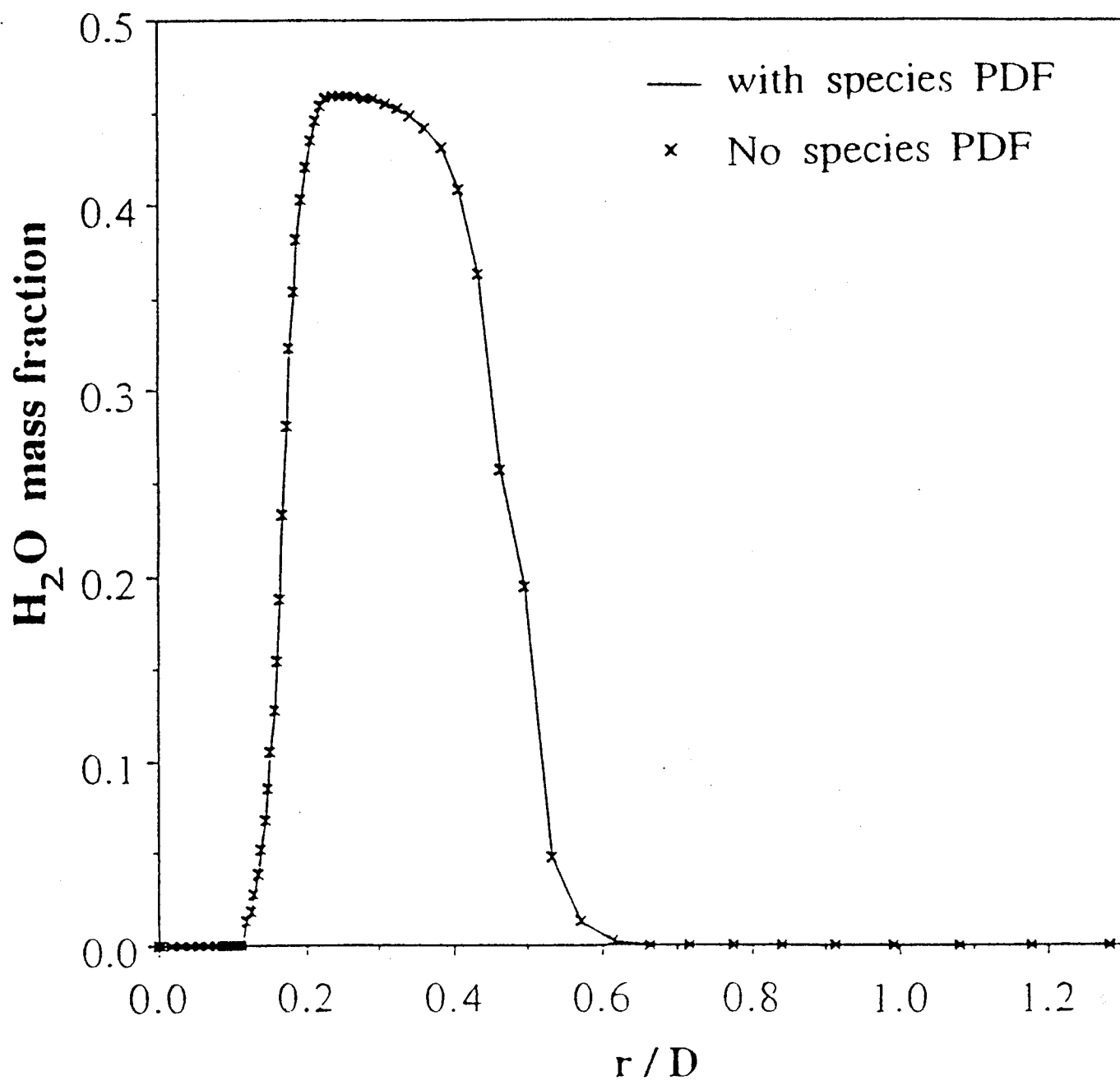


Fig. 5.35 Effect of multivariate species PDF on water mass fraction

5.4 Turbulence-Radiation Interactions

Studies were conducted to investigate the extent of radiative heat transfer in supersonic turbulent reacting flows undergoing hydrogen-air chemical reactions. For the temperature range considered in this study, the important radiating species are OH and H₂O. The turbulence models used in this study are the same as in Sec. 5.2 of this chapter — the turbulence is accounted for via a Reynolds Stress model and the temperature fluctuations are modeled with a Beta-PDF. The radiative interactions have been computed using the same formulation used in Sec. 5.1 of this chapter — the radiative heat transfer is simulated with a tangent slab model employing the pseudo-gray formulation. The chemistry model used in this study is a truncated 7-species, 7-step mechanism, derived from the first seven reactions in Table 2.1. The resulting formulation is a simple extension of Sec. 5.2, and the physical model used for the present work is the Jarrett-Pitz experiment [90].

A schematic diagram of this experiment is given in Fig. 4.1. The temperature and other exit conditions for the nozzle are given in Table 4.2. The outside diameter of the nozzle ($D = 0.01778$ m.) is used to normalize the axial and radial profiles. The length of the flow domain is taken to be 5.7 diameters, i.e. $x = 0.1016$ m. Initial profiles for the flow variables are obtained by computing flat plate solutions. This is carried out separately for the fuel and air streams and then the two flows are combined. A fixed location of $x/D = 0.85$ is chosen since experimental data are available for CFD code validation.

Figure 5.36 shows radial profiles of the streamwise radiative flux q_{RX} . Two interesting phenomena can be observed here. Firstly, the radiative flux increases in the region of the flame. This is because radiative heat transfer is a strong function of temperature and H₂O mass fraction. Secondly, the radiative heat transfer is enhanced by accounting for the

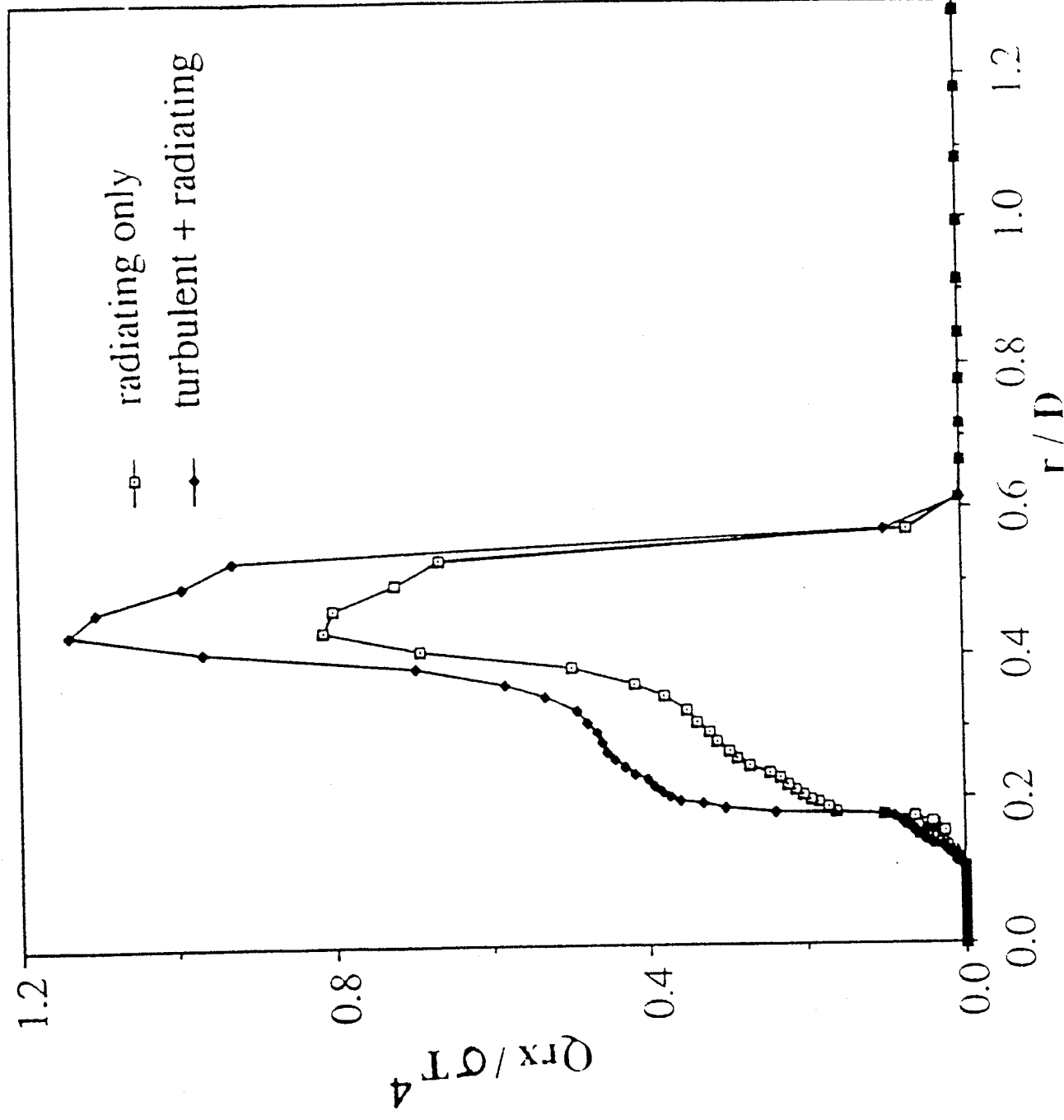


Fig. 5.36 Profiles of streamwise radiative flux — Jarret-Pitz expt.

turbulent fluctuations in temperature. In this case, a fixed value of 0.4 for the variance of the temperature fluctuation is assumed, i.e. $\widetilde{T_0'^2}/\widetilde{T} = 40\%$. This parametric approach is preferred over solving a “g-equation” for the temperature variance. This coupling of turbulence and radiation is achieved via a Beta PDF for temperature.

Figure 5.37 shows that the effect of radiative heat transfer is to lower the temperature. This is the “radiative cooling effect” and is strongest only in the flame region.

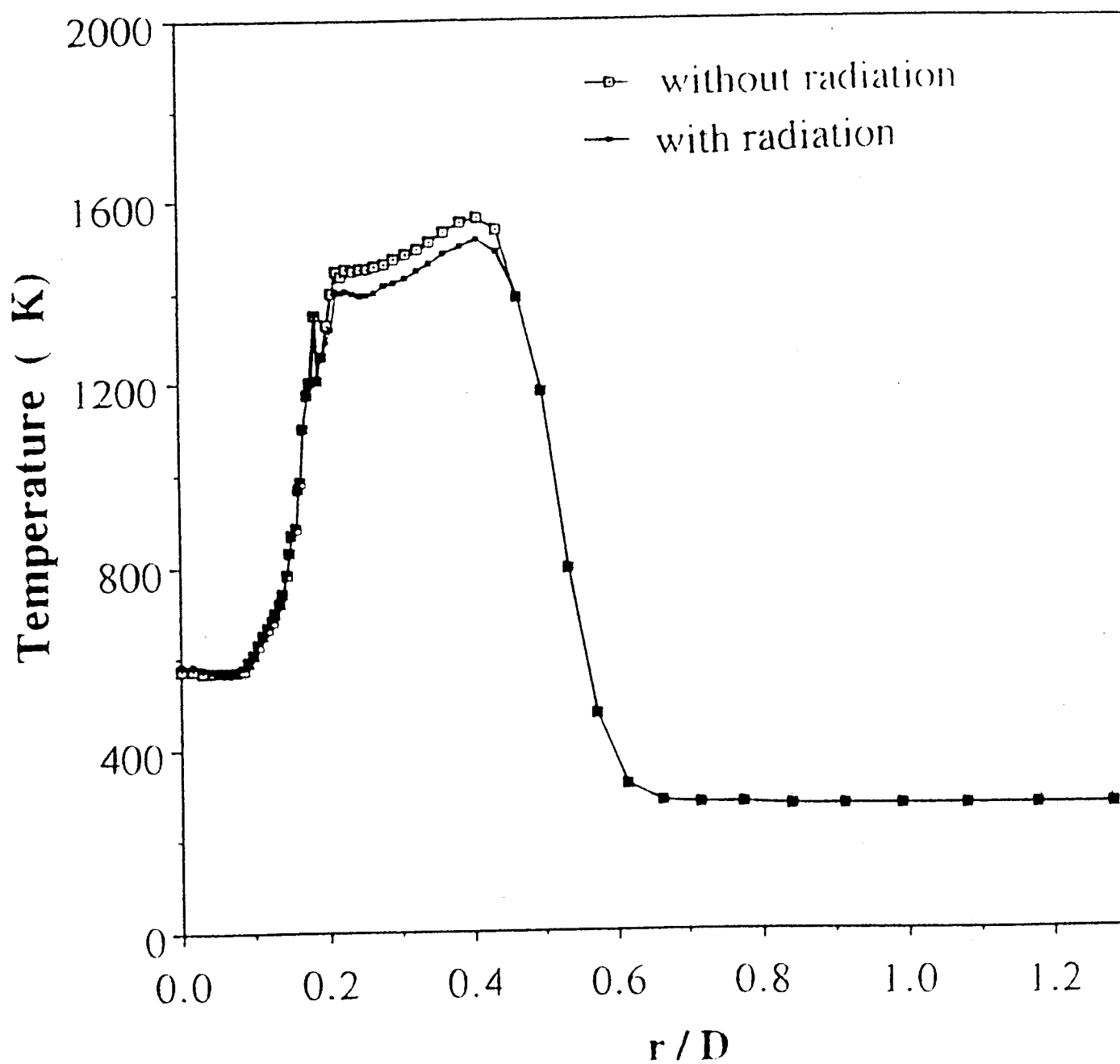


Fig. 5.37 Effect of “turbulent/radiation” coupling on temperature

Chapter 6

CONCLUSIONS

This study presents a systematic investigation of nonequilibrium processes in supersonic combustion. The two-dimensional, elliptic Navier-Stokes equations were used to investigate supersonic flows with nonequilibrium chemistry and thermodynamics, coupled with radiation, for hydrogen-air systems. The explicit, unsplit MacCormack finite-difference scheme was used to advance the governing equations in time, until convergence was achieved. The chemistry source term in the species equation was treated implicitly to alleviate the stiffness associated with fast reactions. Specific conclusions of studies conducted on premixed and non-premixed flows are presented here briefly.

Results obtained for the first part of this study indicate the radiative interactions varied substantially, depending on reactions involving HO_2 and NO species, and that this could have a noticeable influence on the flowfield. Also, it is observed that the difference in the ignition delays of two chemistry models involving HO_2 reactions is nullified as a result of radiative interaction. The results also showed that the streamwise radiative flux reduces the temperature and concentration of the species. This effect is a strong function of the amount of H_2O species concentration.

Results obtained for the second part of this investigation show that the presence of nonequilibrium in the expansion region of the nozzle. This reduces the temperature, pressure, species mass fractions as well as the radiative fluxes. The effect of radiative

interactions is to reduce the extent of thermal nonequilibrium due to additional mode of energy transfer.

Results obtained for the third part of this study indicate that the effect of heat release is to lower the turbulent shear stress and the mean density. Also, it is noted that the production of turbulence is a "nonequilibrium" process. Results obtained for the last part of this investigation show that the effect of turbulence/radiation interactions is to enhance the radiative heat transfer.

Based on the present study, several recommendations concerning the extensions of this work are suggested. Effects of ionization should be included in the thermal nonequilibrium investigations. Also, effects of anharmonic oscillators should be considered in the latter studies. Nongray radiation heat transfer should be investigated and models for multi-dimensional radiation should be developed. Extensions to other combustion problems should be carried out. Last but not in the least, effect of species PDF on radiative interactions should be studied.

REFERENCES

1. Kumar, A., "Numerical Simulation of Scramjet Inlet Flowfield," NASA TP-25117, May 1986.
2. Drummond, J. P., Hussaini, M. Y., and Zang, T. A., "Spectral Methods for Modelling Supersonic Chemically Reacting Flowfields," AIAA Journal, Vol. 24, No. 9, September 1986, pp. 1461-1467; also Drummond, J. P., "Numerical Simulation of Supersonic Chemically Reacting Mixing Layers," Ph.D. Dissertation, George Washington University, May 1987.
3. Drummond, J. P., Rogers, R. C., and Hussaini, M. Y., "A Detailed Numerical Model of a Supersonic Reacting Mixing Layer," AIAA Paper 86-1427, June 1986.
4. Chitsomboon, T., Kumar, A., Drummond, J. P., and Tiwari, S. N., "Numerical Study of Supersonic Combustion Using a Finite-Rate Chemistry Model," AIAA Paper 86-0309, January 1986.
5. Rogers, R. C. and Schexnayder, C. J., Jr., "Chemical Kinetic Analysis of Hydrogen-Air Ignition and Reaction Time," NASA TP-1856, 1981.
6. Shuen, S. J. and Yoon, S., "Numerical Study of Chemically Reacting Flows Using a Lower-Upper Symmetric Successive Overrelaxation Scheme," AIAA Journal, Vol. 27, No. 12, December 1989, pp. 1752-1760.
7. Carpenter, M. H., "A Generalized Chemistry Version of SPARK," NASA CR-4196, December 1988.
8. Sparrow, E. M. and Cess, R. D., Radiation Heat Transfer, Brooks/Cole, Belmont, CA, 1966 and 1970. New Augmented Edition, Hemisphere Publ. Corp., Washington D. C., 1978.
9. Tien, C. L., "Thermal Radiation Properties of Gases," Advances in Heat Transfer, Vol. 5, Academic Press, New York, 1968.
10. Cess, R. D. and Tiwari, S. N., "Infrared Radiative Energy Transfer in Gases," Advances in Heat Transfer, Vol. 8, Academic Press, New York, 1972.
11. Edwards, D. K., "Molecular Gas Band Radiation," Advances in Heat Transfer, Vol. 12 Academic Press, New York, 1976.

12. Tiwari, S. N., "Band Models and Correlations for Infrared Radiation," Radiative Transfer and Thermal Control (Progress in Aeronautics and Astronautics, Vol. 49), American Institute of Aeronautics and Astronautics, New York, 1979.
13. Tiwari, S. N., "Models for Infrared Atmospheric Radiation," Advances in Geophysics, Vol. 20, Academic Press, New York, 1978, pp. 1-85.
14. Tsai, S. S. and Chan, S. H., "Multi-Dimensional Radiative Transfer in Non-Gray Gases-General Formulation and the Bulk Radiative Exchange Approximation," Journal of Heat Transfer, Vol. 100, No. 3, August 1978, pp. 486-491.
15. Chung, T. J. and Kim J. Y., "Two-Dimensional Combined Mode Heat Transfer by Conduction, Convection and Radiation in Emitting, Absorbing and Scattering-Solution by Finite Elements," Journal of Heat Transfer, Vol. 106, No. 2, May 1984, pp. 448-452.
16. Im, K. H. and Ahluwalia, R. K., "Combined Convection and Radiation in Rectangular Duct," International Journal of Heat and Mass Transfer, Vol. 27, No. 2, February 1984, pp. 221-231.
17. Soufiani, A. and Taine, J., "Application of Statistical Narrow-Band Models to Coupled Radiation and Convection at High Temperature," International Journal of Heat and Mass Transfer, Vol. 30, No. 3, March 1987, pp. 437-447.
18. Tiwari, S. N., "Radiative Interaction in Transient Energy Transfer in Gaseous Systems," NASA CR-176644, December 1985.
19. Tiwari, S. N. and Singh, D. J., "Interaction of Transient Radiation in Fully Developed Laminar Flow," AIAA Paper 87-1521, June 1987.
20. Mani, M., Tiwari, S. N., and Drummond, J. P., "Numerical Solution of Chemically Reacting and Radiating Flows," AIAA Paper 87-0324, January 1987.
21. Mani, M., Tiwari, S. N., and Drummond, J. P., "Investigation of Two-Dimensional Chemically Reacting and Radiative Supersonic Channel Flows," AIAA Paper 88-0462, January 1988.
22. Mani, M. and Tiwari, S. N., "Investigation of Supersonic Chemically Reacting and Radiating Channel Flow," NASA CR-182726, January 1988 ; also Ph.D. Dissertation by M. Mani, Old Dominion University, May 1988.
23. Clarke, J. F. and McChesney, M., Dynamics of Relaxing Gases, Butterworth, 1976.
24. Vincenti, W. G. and Kruger, C. H., "Introduction to Physical Gas Dynamics," John Wiley & Sons, Inc., New York 1965.

25. Kuznetsov, V. M., "Theory of the Bulk Viscosity Coefficient," Fluid Mechanics (Mekhanika Zhidkosti i Gaza), Vol. 2, October 1966, pp. 62-64.
26. MacCormack, R. W., "The Effect of Viscosity in Hypervelocity Impact Cratering," AIAA Paper 69-354, May 1969.
27. Smoot, L. D., Hecker, W. C., and Williams, G. A., "Prediction of Propagating Methane-Air Flames," Combustion and Flame, Vol. 26, No. 3, June 1976, pp. 323-342.
28. Bussing, T. R. and Murman, E. M., "A Finite Volume Method for the Calculation of Compressible Chemically Reacting Flows," AIAA Paper 85-0331, January 1985.
29. Smith, R. E. and Weigel, B. L., "Analytical and Approximation Boundary Fitted Coordinates System for Fluid Flow Simulation," AIAA Paper 80-0192, January 1980.
30. Anderson, D. A., Tannehill, J. C., and Pletcher, R. H., Computational Fluid Mechanics and Heat Transfer, McGraw Hill, New York 1984.
31. Wilkins, J. H., The Algebraic Eigenvalue Problem, Oxford University Press, Oxford, England, 1965, pp. 233-236.
32. Householder, A. S., The Theory of Matrices in Numerical Solution Analysis, Dover Publication, New York, 1964, pp. 122-140.
33. Bray, K. N. C., "Atomic Recombination in a Hypersonic Wind Tunnel Nozzle," Journal of Fluid Mechanics, Vol. 6, July 1959, pp. 1-32.
34. Blythe, P. A., "Nonequilibrium Flow through a Nozzle," Journal of Fluid Mechanics, Vol. 17, September 1963, pp. 126-140.
35. Blythe, P. A., "Asymptotic Solutions in Nonequilibrium Nozzle Flow," Journal of Fluid Mechanics, Vol. 20, October 1964, pp. 243-272.
36. Stollery, J. L. and Park, C., "Computer Solutions to the Problem of Vibrational Relaxation in Hypersonic Nozzle Flows," Journal of Fluid Mechanics, Vol. 19, May 1964, pp. 113-123.
37. Cheng, H. K. and Lee, R. S., "Freezing of Dissociation in Supersonic Nozzle Flows," AIAA Paper 66-1, June 1966.
38. Hall, J. G. and Treanor, C. E., "Nonequilibrium Effects in Supersonic Nozzle Flows," AGARDograph No. 124, December 1967.

39. Anderson, J. D., Jr., "A Time-Dependent Analysis for Vibrational and Chemical Nonequilibrium Nozzle Flows," *AIAA Journal*, Vol. 8, No.3, March 1970, pp. 545-550.
40. Anderson, J. D., Jr., "Time-Dependent Solutions of Nonequilibrium Nozzle Flows — A Sequel," *AIAA Journal*, Vol. 8, No. 12, December 1970, pp. 2280-2282.
41. von Rosenberg, C. W., Jr., Bray, K. N. C., and Pratt, N. H., "The Effect of Water Vapor on the Vibrational Relaxation of CO," *Proceedings of the 13th Symposium (International) on Combustion*, The Combustion Institute, 1971, pp. 89-98.
42. von Rosenberg, C. W., Jr., Bray, K. N. C., and Pratt, N. H., "Shock Tube Vibrational Relaxation Measurements: N₂, Relaxation by H₂O and the CO-N₂ V-V Rate," *Journal of Chemical Physics*, Vol. 56, No. 7, April 1972, pp. 3230-3237.
43. Kung, R. T. V. and Center, R. E., "High Temperature Vibrational Relaxation of H₂O by H₂O, He, Ar, and N₂," *Journal of Chemical Physics*, Vol. 62, No. 6, March 1975, pp. 2187-2194.
44. Kothari, A. P., Anderson, J. D., Jr., and Jones, E., "Navier-Stokes Solutions for Chemical Laser Flows," *AIAA Journal*, Vol. 15, No. 1, January 1976, pp. 92-100.
45. Anderson, J. D., Jr., *Gasdynamic Lasers: An Introduction*, Academic Press, New York, 1976.
46. Reddy, N. M. and Shanmugasundaram, V., "Theoretical Gain-Optimization Studies in CO₂-N₂ Gasdynamic Lasers. I — Theory. II — Results of Parametric Study," *Journal of Applied Physics*, Vol. 50, April 1979, pp. 2565-2582.
47. Wada, Y., Yamaguchi, M., and Kubota, H., "Numerical Investigation of Nozzle Shape Effects on CO₂ Gas Dynamic Laser Performance," *AIAA Paper 87-1452*, June 1987.
48. Rakich, J. V., Bailey, H. E., and Park, C., "Computation of Nonequilibrium, Supersonic Three-Dimensional Inviscid Flow over Blunt-Nosed Bodies," *AIAA Journal*, Vol. 21, No. 6, June 1983, pp. 834-841.
49. Lee, J. H., "Basic Governing Equations for the Flight Regimes of Aeroassisted Orbital Transfer Vehicles," *AIAA Progress in Aeronautics and Astronautics*, Vol. 96, edited by H. F. Nelson, 1985, pp. 3-53.
50. Gnoffo, P. A., "Application of Program LAURA to Three-Dimensional AOTV Flowfields," *AIAA Paper 86-0565*, January 1986.

51. Candler, G. V. and MacCormack, R. W., "The Computation of Hypersonic Ionized Flows in Chemical and Thermal Nonequilibrium," AIAA Paper 88-0511, January 1988.
52. Gnoffo, P. A., Gupta, R. N., and Shinn, J. L., "Conservation Equations and Physical Models for Hypersonic Air Flows in Thermal and Chemical Nonequilibrium," NASA-TP-2867, February 1989.
53. Desideri, J. A., Glowinski, R., and Periaux, J. — Eds., Hypersonic Flows for Reentry Problems, Vol. 2, Springer Verlag, January 1990.
54. Finzi, J., Hovis, F. E., Panfilov, V. N., Hess, P., and Moore, C. B., "Vibrational Relaxation of Water Vapor," Journal of Chemical Physics, Vol. 67, No. 9, November 1977, pp. 4053-4061.
55. Center, R. E. and Newton, J. F., "Vibrational Relaxation of N_2 by H_2O ," Journal of Chemical Physics, Vol. 68, No. 8, April 1978, pp. 3327-3333.
56. Grossmann, B. and Cinella, P., "The Computation of Nonequilibrium, Chemically-Reacting Flows," Computers and Structures, Vol. 30, No. 1/2, October 1988, pp. 79-93.
57. Grossmann, B. and Cinella, P., "Flux-Split Algorithms for Flows with Nonequilibrium Chemistry and Vibrational Relaxation," Journal of Computational Physics, Vol. 88, No.1, May 1990, pp. 131-168.
58. Tiwari, S. N. and Cess, R. D., "The Influence of Vibrational Nonequilibrium upon Infrared Radiative Energy Transfer," Journal of Quantitative Spectroscopy and Radiative Transfer, Vol. 11, No.3, March 1971, pp. 237-248.
59. Goody, R. M., Atmospheric Radiation, Oxford University Press, London (1964).
60. Gilles, S. E. and Vincenti, W. G., "Coupled Radiative and Vibrational Nonequilibrium in a Diatomic Gas, with Application to Gas Dynamics," Journal of Quantitative Spectroscopy and Radiative Transfer, Vol. 10, No.2, February 1970, pp. 71-97.
61. Wang, L. S., "The Cooling of a Gas not in Local Thermodynamic Equilibrium by Conduction and Radiation," AIAA Paper 69-638, June 1969.
62. Park, C., Nonequilibrium Hypersonic Aerothermodynamics, John Wiley, 1990.
63. Millikan, R. C. and White, D. R., "Systematics of Vibrational Relaxation," Journal of Chemical Physics, Vol. 39, No. 12, December 1963, pp. 3209-3213.
64. Strehlow, R. A., Combustion Fundamentals, McGraw Hill, 1984, pp. 23.

65. Hill, T. L., *An Introduction to Statistical Thermodynamics*, Dover, New York, 1986, pp. 186.
66. Herzberg, G., *The Spectra and Structures of Simple Free Radicals*, Cornell University Press, Ithaca, N. Y., 1971, pp. 65.
67. Gokcen, T. and Park, C., "The Coupling of Radiative Transfer to Quasi 1-D Flows with Thermochemical Nonequilibrium," AIAA Paper 91-0570, January 1991.
68. Eklund, D. R., Drummond, J. P., and Hassan, H. A., "Numerical Modelling of Turbulent Supersonic Reacting Coaxial Jets," AIAA Paper 89-0660, January 1989.
69. Jones, W. P. and Whitelaw, J. H., "Calculation Methods for Reacting Turbulent Flows: A Review," *Combustion and Flame*, Vol. 48, No. 1, October 1982, pp. 1-26.
70. Givi, P., Madnia, C. K., Steinberger, C. J., Carpenter, M. H., and Drummond, J. P., "Effects of Compressibility and Heat Release in a High Speed Reacting Mixing Layer," *Combustion Science and Technology*, Vol. 78, Nos. 1-3, 1991, pp. 33-67.
71. Frankel, S. H., Drummond, J. P. and Hassan, H. A., "A Hybrid Reynolds Averaged/PDF Closure Model for Supersonic Turbulent Combustion," AIAA Paper 90-1573, July 1990.
72. Narayan, J. R., "A Two-Equation Turbulence Model for Compressible Reacting Flows," AIAA Paper 91-0755, January 1991.
73. Villasenor, R., Pitz, R., and Chen, J., "Modelling Ideally Expanded Supersonic Turbulent Jet Flows with Non-Premixed Combustion," AIAA Paper 90-0640, January 1990; also, *AIAA Journal*, Vol. 30, No. 2, February 1992, pp. 395-402.
74. Kolbe, W. and Kollmann, W., "Prediction of Turbulent Diffusion Flames with a Four-Equation Turbulence Model," *Acta Astronautica*, Vol. 7, No. 1, January 1980, pp. 91-104.
75. Hinze, J. O., *Turbulence*, McGraw Hill Book Co., pp. 1-790, 1975.
76. Moss, J. B., "Simultaneous Measurements of Concentration and Velocity in an Open Premixed Turbulent Flame," *Combustion Science and Technology*, Vol. 22, No. 4, 1980, pp. 115-120.
77. Libby, P. A. and Bray, K. N. C., "Countergradient Diffusion in Premixed Turbulent Flames," *AIAA Journal*, Vol. 19, No. 2, pp. 205-213, 1981.
78. Hogg, S. and Leschziner, M. A., "Computation of Highly Swirling Confined Flow with a Reynolds Stress Turbulence Model," *AIAA Journal*, Vol. 27, No. 1, January 1989, pp. 57-63.

79. Cox, G., "On Radiant Heat Transfer from Turbulent Flames," *Combustion Science and Technology*, Vol. 17, Nos. 1-2, January 1977, pp. 75-78.
80. Tamanini, F., "Reaction Rates, Air Entrainment and Radiation in Turbulent Fire Plumes," *Combustion and Flame*, Vol. 30, No. 1, January 1977, pp. 85-101.
81. Kabashnikov, V. P. and Kmit, G. I., "Influence of Turbulent Fluctuations on Thermal Radiation," *Journal of Applied Spectroscopy*, Vol. 31, No. 2, August 1979, pp. 963-967.
82. Gore, J. P., Jeng, S. M., and Faeth, G. M., "Spectral and Total Radiation Properties of Turbulent Hydrogen/Air Diffusion Flames," *ASME Journal of Heat Transfer*, Vol. 109, February 1987, pp. 165-171.
83. Jeng, S. M. and Faeth, G. M., "Radiative Heat Fluxes Near Turbulent Buoyant Methane Diffusion Flames," *ASME Journal of Heat Transfer*, Vol. 106, No. 4, November 1984, pp. 886-888.
84. Yuen, W. W., Ma, A. K., and Takara, E. E., "Turbulence/ Radiation Interaction in a Non-Gray, Absorbing, Emitting and Isotropically Scattering Medium," *Heat Transfer in Fire and Combustion Systems*, Kanury, A. M. and Brewster, M. Q., eds., HTD-Vol. 199, ASME, New York, pp. 53-62, 1992.
85. Fairweather, M., Jones, W. P., and Lindstedt, R. P., "Predictions of Radiative Transfer from a Turbulent Reacting Jet in a Cross-Wind," *Combustion and Flame*, Vol. 89, No. 1, July 1992, pp. 89-63.
86. Chen, J. Y., "Second-Order Conditional Modelling of Turbulent Non-Premixed Flames with a Composite PDF," *Combustion and Flame*, Vol. 69, No. 1, July 1987, pp. 1-36.
87. Farschi, M., "Prediction of Heat Release Effects on a Mixing Layer," *AIAA Paper* 86-0058, January 1986.
88. Sarkar, S. and Balakrishnan, L., "Application of a Reynolds Stress Turbulence Model to the Compressible Shear Layer," *NASA CR-182002* ; also *ICASE Report* No. 90-18, February 1990.
89. Evans, J. S., Schexnayder, C. J., and Beach, H. L., Jr., "Application of a Two-Dimensional Parabolic Computer Program to Prediction of Turbulent Reacting Flows," *NASA TP-1169*, March 1978.
90. Jarrett, O., Jr., Cutler, A. D., Antcliff, R. R., Chitsomboon, T., Dancey, C. L., and Wang, J. A., "Measurements of Temperature, Density and Velocity in Supersonic

Reacting Flow for CFD Code Validation," Presented at the 25th JANNAF Combustion meeting, Huntsville, AL, October 1988.

91. Jachimowski, C. J., "An Analytical Study of the Hydrogen-Air Reaction Mechanism with Application to Scramjet Combustion," NASA TP-2791, February 1988.
92. Hermanson, J. C. and Dimotakis, P. E., "Heat Release Effects on Shear Layer Growth and Entrainment," AIAA Paper 85-0142, January 1985.
93. Demuren, A. O. and Sarkar, S., "Systematic Study of Reynolds Stress Closure Models in the Computations of Plane Channel Flows," ICASE Report No. 92-19, April 1992.
94. Girimaji, S. S., "A Simple Recipe for Modeling Reaction Rates in Flows with Turbulent Combustion," AIAA Paper 91-1792, June 1991.

AUTOBIOGRAPHICAL STATEMENT

Rajnish Chandrasekhar was born in Bangalore, India on August 16, 1962. He received his undergraduate Honors degree in Aeronautical Engineering from the Indian Institute of Technology at Kharagpur, India in May 1985. Subsequently, he obtained his Master's in Mechanical Engineering from Concordia, University in Montreal, Canada in May 1988. His Master's research was funded by the National Sciences and Engineering Research Council (NSERC) of Canada as a Research Assistantship.

He is a student member of the American Institute of Aeronautics and Astronautics (AIAA), and the American Institute of Chemical Engineers (AIChE).